

# Optical Mapping of Organohalide Lead Perovskite Films

By

Joseph A. Sadler, B.S.

A thesis submitted to the Graduate Council of  
Texas State University in partial fulfillment  
of the requirements for the degree of  
Master of Science  
with a Major in Physics  
May 2018

Committee Members:

Alexander Zakhidov

Wilhelmus Geerts

David Donnelly

**COPYRIGHT**

by

Joseph Sadler

2018

## **FAIR USE AND AUTHOR'S PERMISSION STATEMENT**

### **Fair Use**

This work is protected by the Copyright Laws of the United States (Public Law 94-553, section 107). Consistent with fair use as defined in the Copyright Laws, brief quotations from this material are allowed with proper acknowledgement. Use of this material for financial gain without the author's express written permission is not allowed.

### **Duplication Permission**

As the copyright holder of this work I, Joseph A. Sadler, authorize duplication of this work, in whole or in part for educational or scholarly purposes only.

## DEDICATION

For my mother Rebecca Lyn Buchanan and step-father Donald Dean Wright.

Many thanks to my fiancé Breanna McCormack and her parents, as well as the Zaleski family for their continued love and support. I would like to show to my appreciation my oldest friend and best-man Brandon Forrest for his longstanding friendship and motivation.

Lastly, I would like to extend my thanks to Dr. Ron Paul for being one of the strongest influences in my early life, inspiring me to strive for peace, act with a spirit of love, and always seek liberty. It was after being introduced to his ideals that I began to immerse myself more in the study of history, economics, and philosophy, which prepared me to become an active leader in the student organization Young Americans for Liberty (YAL) where I met my fiancé and many of my closest friends.



## **ACKNOWLEDGEMENTS**

Firstly, I would Like to Thank the members of my committee Dr. Alexander Zakhidov (my thesis advisor), Dr. Wilhelmus Geerts, and Dr. David Donnelly for their years of guidance and support throughout my academic career. I would like to thank the National Science Foundation (NSF) for their funding and support.

Additionally, I would like to thank Dr. Dmitry Lyashenko for his insight and assistance as I began research in the Zakhidov Lab, Dr. Casey Smith and the Analysis Research Service Center (ARSC) staff for the training and use of their equipment and facility, as well as my classmate, colleague, and one of my best friends Ben C. Brooks.

# TABLE OF CONTENTS

	Page
ACKNOWLEDGEMENTS .....	v
LIST OF TABLES .....	viii
LIST OF FIGURES .....	ix
ABSTRACT .....	xii
CHAPTER	
I. INTRODUCTION .....	1
Financial and Environmental Motivation .....	1
The Changing Global Energy Market .....	2
Benefits of Solar Power .....	4
Introduction to Perovskites .....	5
II. PEROVSKITE PHOTOVOLTAICS .....	8
Perovskite properties and crystalline structure .....	8
Perovskite degradation and the challenges of stability .....	15
Thermal Degradation .....	16
Moister and Atmospheric Degradation .....	17
Interfacial degradation .....	20
III. CHARACTERIZATION METHODS .....	22
Ellipsometry .....	22
Polarization .....	22
Light-matter interaction .....	26
Regression analysis .....	28
Sample Preparation .....	32
Building the $\text{PbI}_2$ and $\text{MAPbI}_3$ models .....	34
Results .....	38
C-PL .....	41
Photoluminescence and Confocal Imaging .....	42
Film Sets .....	45
Signal Reflection .....	49
Results .....	51
Raman Spectroscopy .....	57
Confocal Raman Spectroscopy .....	60

Raman Signature of MAPbI <sub>3</sub> and PbI <sub>2</sub> .....	61
Observed MAPbI <sub>3</sub> degradation .....	63
Sample creation.....	65
Various MAPbI <sub>3</sub> spectra issues.....	67
Proper MAPbI <sub>3</sub> Spectra.....	68
MAPbI <sub>3</sub> Induced Step.....	70
Interfacial Thermal Degradation.....	74
Axial Scans .....	76
 CONCLUSIONS.....	 83
REFERENCES .....	86

## LIST OF TABLES

<b>Table</b>	<b>Page</b>
3.1.1 Literature Parameters after fit. ....	36
3.1.2 Parameters of the newly created models.....	36
3.1.3 Layered sample fit data.....	38

## LIST OF FIGURES

Figure	Page
1.2.1 Projection of US energy sources to 2040.....	3
1.2.2 Projection of the global share and growth of renewable energy production .....	4
1.3.1 NREL Solar Cell Efficiency Chart 10-30-2017.....	6
2.1.1 range of bandgap to ABX <sub>3</sub> formulation .....	10
2.1.2 Depiction of the Joint Density Of States.....	11
2.1.3 Shallow traps of MAPbI <sub>3</sub> in (a) the lower and (b) upper bands.....	13
2.1.4 Perovskite Mobility.....	14
2.1.5 Amount of lead contained in a perovskite PV module and in natural soil. ....	15
2.2.1 Degradation mechanism of MAPbI <sub>3</sub> exposed to moisture.....	18
2.2.2 Hydrated MAI- and PbI <sub>2</sub> -terminated and PbI <sub>2</sub> -defective perovskite slabs.....	19
3.1.1 Various polarization states of a monochromatic light wave.....	23
3.1.2 Elliptically polarized light and the projected polarization ellipse. ....	24
3.1.3 Reflection of polarized light. ....	25
3.1.4 The regression analysis process. ....	30
3.1.5 Single Parameter uniqueness fit.....	31
3.1.6 Multi parameter uniqueness.....	31
3.1.7 Modeled n and k values vs the values reported in the literature.....	37
3.1.8 Graph of the $\Psi$ and $\Delta$ model fit. ....	39
3.1.9 The Difference between the measured and modeled values of $\Psi$ and $\Delta$ . ....	40
3.1.10 System %Depolarization.....	40
3.2.1 Photoluminescence. ....	42

3.2.2 General Confocal-PL beam path.....	43
3.2.3 PL measurements of $\text{PbI}_2$ and $\text{MAPbI}_3$ .....	45
3.2.4. Ray tracing the Depth Resolution. ....	47
3.2.5. Depth Resolution vs Focus Depth.....	48
3.2.6 Side Peak due to reflection. ....	49
3.2.7 Surface Image of Perovskite Film.....	52
3.2.8 Comparing axial intensity of scans .....	53
3.2.9 Comparing bare $\text{MAPbI}_3$ samples to samples with $\text{PbI}_2$ deposited on perovskite. ....	54
3.2.10. The calculated dependence between real and apparent thickness .....	54
3.2.11 XRD analysis of film produced with varying MAI/IPA solution concentrations. ....	55
3.2.12. c-PL depth measurement of films formed with varying concentrations of MAI to IPA. ....	56
3.3.1 types of light scattering.....	58
3.3.2 Raman readout of scattered light. ....	59
3.3.3 Peak shape as it relates to material characterization.....	60
3.3.4 General beam path of a confocal Raman system. ....	61
3.3.5 Raman spectra of $\text{MAPbI}_3$ thin films .....	63
3.3.6 Breakdown of the $\text{MAPbI}_3$ Raman signature.....	64
3.3.7 Raman spectra of $\text{MAPbI}_3$ prior to baseline corrections. ....	69
3.3.8 Raman spectra and baseline correction.....	70
3.3.9 Signal change depending on grating used.....	71
3.3.10 Extended wavenumber range.....	72
3.3.11 Spectra change as $\text{MAPbI}_3$ film degrades. ....	73

3.3.12 Shifting MAPbI3 induced step.....	74
3.3.13 The effects of interface on MAPbI3 stability. ....	75
3.3.14 Change in average intensity with laser exposure. ....	76
3.3.15 comparison of PbI2 data. ....	77
3.3.16 Axial (z-axis/depth) scan of PbI2 .....	78
3.3.17 Raman Spectra of PbI2 film covered with 10nm of SnO2. ....	79
3.3.18 Axial (z-axis/depth) scan of MAPbI3 show the step-feature.....	80
3.3.19 Axial (z-axis/depth) scan showing the proper signature for a MAPbI3 film.....	81
3.3.20 Axial (z-axis/depth) scan of MAPbI3/SnO2/PbI2. ....	82

## ABSTRACT

Although thin film methylammonium lead iodide ( $\text{CH}_3\text{NH}_3\text{PbI}_3$  also written as  $\text{MAPbI}_3$ ) perovskite photovoltaics (PV) are cheap to produce and have seen a quick rise in power conversion efficiency (PCE), from 2.19 in 2006 to 22.7 as of 2017, they have not been able to find a place on the world energy market due to the persistent problem of film degradation. In this thesis I looked at three optical characterization techniques, i) Spectral Ellipsometry (SE), ii) Confocal- Photoluminescence (c-PL), and iii) Raman Spectroscopy (RS), to determine their competency in characterizing thin film perovskite through the Z-axis. While interrogating the film with RS with high power to induce degradation we confirmed  $\text{PbI}_2$  to be the byproduct of degraded  $\text{MAPbI}_3$  films, as well as found evidence that heat conductivity of the substrate employed can result in increasing or decreasing the perovskites sensitivity heat. By forming film stacks of  $\text{PbI}_2$  and  $\text{MAPbI}_3$  we found that both RS and c-PL were able to distinguish between the  $\text{PbI}_2$  and  $\text{MAPbI}_3$  layers despite low depth resolution. C-PL also provided insight into the film formation (when using the two-step deposition process) by showing us that the MAI, even at low concentrations, appears to evenly diffuse throughout the, initially formed,  $\text{PbI}_2$  film layer. Lastly, using SE I was able to create optical models that accurately determined film composition as well as film thickness in stacked samples

# I. INTRODUCTION

## Financial and Environmental Motivation

With global energy demand on the rise there is a growing need to expand energy production from a variety of sources. While working to keep pace with the growing demand, especially in nations that are struggling to become more developed and prosperous, there is also a growing mindfulness of environmental hazards associated with energy production. This environmental conscientiousness is guiding both the consumer markets and governmental policies to shift towards sustainable energy sources, chief among these being wind and solar. Both of which have had drawbacks that limit the rate at which they have been able to expand their total market share, yet with growing interest and demand they have seen a rise in funding to both help with the initial infrastructure cost as well as research and development of newer, more efficient, and cost effective sustainable sources.

One of the newer candidates for solar energy production is the emergent Perovskite photovoltaics (PV). Compared to standard silicon solar panels these devices would be relatively cheap and cleaner to produce. Since their discovery as a promising photovoltaic they have seen a dramatic increase in efficiency, yet the persistent problems with film degradation have proven to be a major setback that has kept them from being widely adopted. In this work I will look at existing methods of film characterization as well as newer methods that are capable of mapping of the film degradation.

## The Changing Global Energy Market

As of 2014 the world consumed  $1.10E^{14}$  kWh, or 9425 Million tons of Oil equivalent (Mtoe) of energy, slightly more than double its consumption of  $5.42 \times 10^{13}$  kWh (4661 Mtoe) in 1973.<sup>1</sup> During this time the largest source of energy has been oil (48.3 to 39.9 percent), followed closely by Natural gas, Coal, and then Biofuels.<sup>1</sup> Despite many advances in these various industries there are still many persistent hazards and negative externalities that result from extraction, transport, and processing of these fuels into energy. The past three years have had a relatively low growth in energy consumption, at or below 1 percent. Although this is almost half the 1.8 yearly average of previous 10 years there is still an ever-growing global demand.<sup>2</sup> Nearly half of the recent growth is due to the fast growing and developing economies of India and China. The yearly world energy consumption, *ceteris paribus*, is projected to increase to  $2.38 \times 10^{14}$  kWh a year as of 2040 (more than double that of 2014 levels) and more than half of this growth is expected to come from non-OECD (Organization for Economic Cooperation and Development) Asian countries.<sup>1,3</sup> Paired with the rise in consumption there is also a rise in demand for renewables which already show signs for a greater shift in the projected fuel mix for energy production. Although oil and coal will continue to be the primary source of world energy consumption, their percent of the market will continue their gradual decline while Renewables, primarily wind and solar, continue their sharp increase. They are projected to increase their share in global power from 7 percent in 2015 to 20 percent by 2035.<sup>4</sup> Even without implementation of the Clean Power Plan the US's use of renewables is projected to near that of coal by 2035 (as seen in Figure 1.2.1).

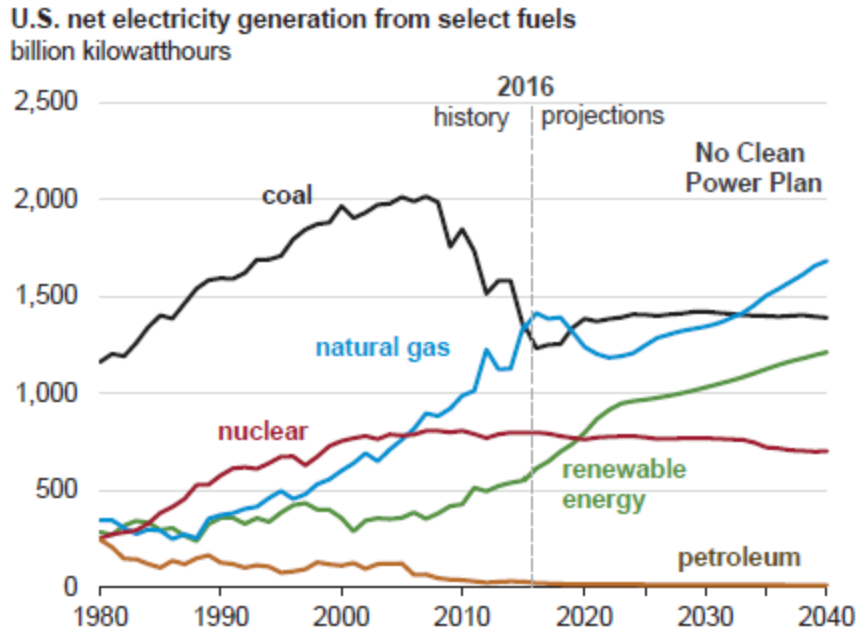
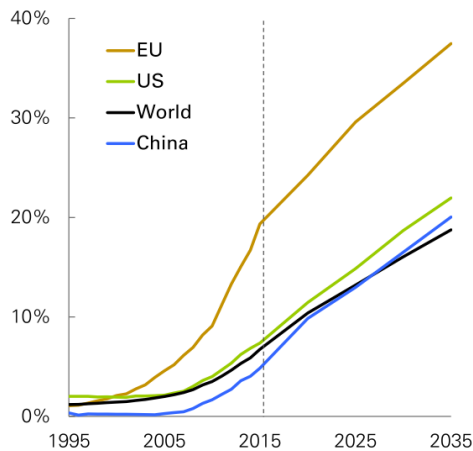


*Figure 1.2.1 Projection of US energy sources to 2040. This projection from the Energy Information Administration (EIA) shows that even without changed in energy policy, such as the CPP, renewables will begin to match coal as a dominant energy source for the US.<sup>5</sup>*

Additionally, the projections Figure 1.2.2 shows that within the 2015-2035 time frame the Chinese are expected to experience an expansion or renewable energy production greater than that of the E.U. and U.S combined, although the EU will still have a far greater total share.<sup>4,5</sup> It is clear that renewable energy is one of the fastest growing industries in the global market and it is an industry that will greatly benefit its investors as well as leading to a massive increase in the standard of living for billions of people living across the globe.

Renewables share of power generation



Shares of renewable power growth

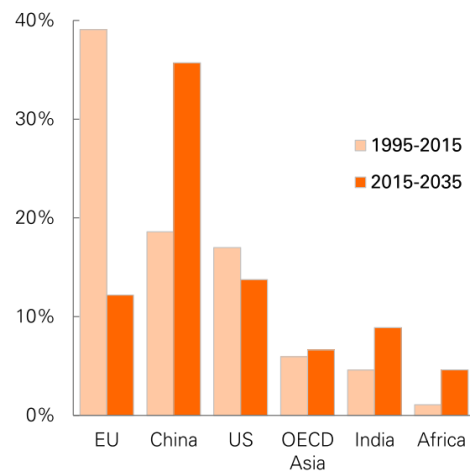


*Figure 1.2.2 Projection of the global share and growth of renewable energy production.<sup>4</sup>*

### Benefits of Solar Power

Solar energy is one of the fastest growing renewable energy sources right behind wind power. The earth is exposed to  $1.5 \times 10^{18}$  kW h of energy emitted by the sun every year, this is more than a hundred times the energy available by the entire worlds known fossil fuel reserves. Although there have been improvements in manufacturing of Si based solar panels a significant amount of energy is still required to create the product from start to finish, so much so that it takes over 2 years before that energy input is repaid.<sup>6</sup> The high cost of manufacturing and installation of these SI solar panels means that there Levelized Cost of Energy (LCOE) is still greater than that of coal and oil.<sup>7</sup> However, due to growing environmental consciousness there is still an ever-growing demand for PV energy. This high cost plus growing demand is a signal that this particular market is greatly in need of innovation.<sup>8,9</sup> As interest in solar energy has grown over the past decade so too has the privet and public investment capital, this

industry is now more than ever ripe for new materials and innovative techniques to keep solar power competitive in this growing market.

### Introduction to Perovskites

One of the most promising materials to emerge in recent years is that of thin film perovskite PVs. The name perovskite refers to a class of minerals discovered by Gustav Rose in 1839. During an expedition in the Ural mountains Rose discovered calcium titanate ( $\text{CaTiO}_3$ ) and named it Perovskite after Count Lev Aleksevich von Perovski, a mineralogist and Minister of Internal Affairs under Nicholas I of Russia. This class of mineral has a unique  $\text{ABX}_3$  structure (also called  $\text{ABO}_3$  with the O for oxygen). The first publication on  $\text{ABX}_3$ , lead halide, perovskites was in 1892.<sup>10</sup> Later, in 1926, Victor Goldschmidt further described the crystal structure and empirically deduced the tolerance factor ( $t$ ) for a stable perovskite, given in equation (1.4.1).

$$t = \frac{r_A + r_X}{\sqrt{2}(r_B + r_X)} \quad (1.4.1)$$

Where  $r_A$ ,  $r_B$ , and  $r_X$  are the atomic (ionic) radii of A, B, and X respectively. Here a stable perovskite is only formed when  $0.8 \leq t \leq 1$ . Additionally, the valences must match (e.g.  $\text{A}^{2+}\text{B}^{4+}\text{X}^{2-}$  or  $\text{A}^+\text{B}^{2+}\text{X}^-$ ). In 1978 Dieter Weber was the first person to study the structure and properties of Organohalide lead perovskites  $\text{MAPbX}_3$  (where x is Br, I, or Cl), yet the first time these materials were tested for photovoltaic properties was in 2006.<sup>11,12</sup>

Although the resultant efficiency was a meager 2.19 percent the potential was there, and the scientific community took interest. Since then perovskites have seen a

faster rate of efficiency increase than any other PV material. This progress is seen in the October 2017 NREL solar cell efficiency chart, Figure 1.3.1. Currently, at 22.7 percent, perovskites have the highest certified efficiency of all single-junction thin-film solar cells.<sup>13</sup> There are many benefits of this type of PV compared to that of silicon based solar cells such as its tunable bandgap, the compounds are already widely used and are cheap, there is no need for an energy intensive refinement process like that of Si-PV.

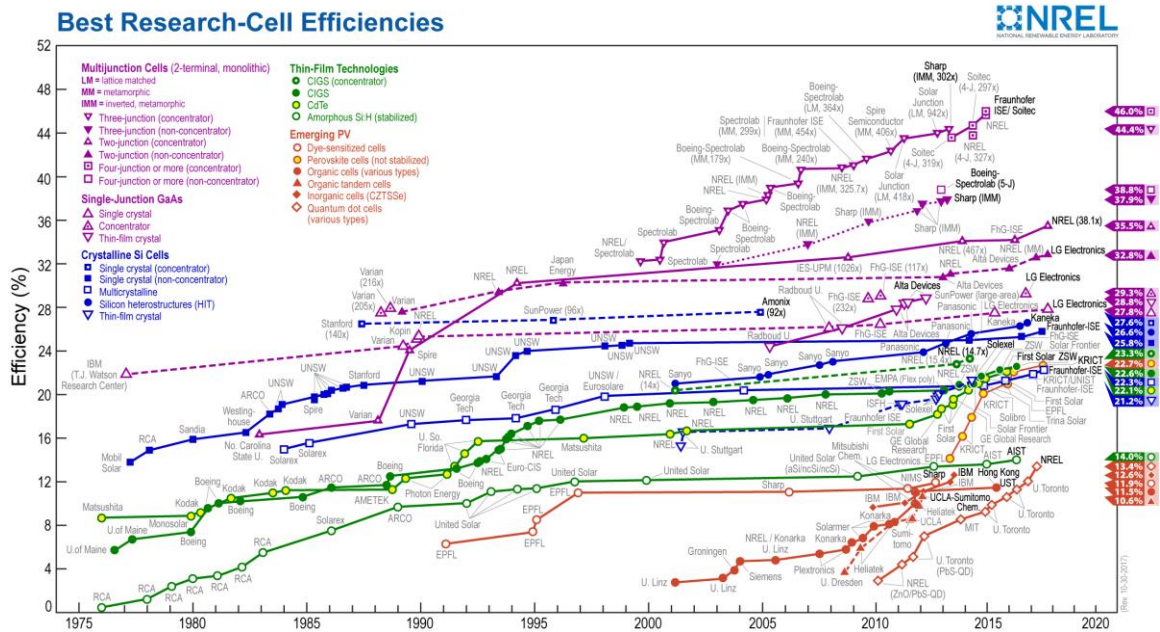


Figure 1.3.1 NREL Solar Cell Efficiency Chart 10-30-2017.<sup>13</sup>

With regards to cost, these materials have an estimated production cost of \$0.05/W as opposed to the current ~1.75/W for commercially available PV systems.<sup>14,15</sup> This drastic reduction in cost satisfies one of the 14 Grand Engineering Challenges for the 21<sup>st</sup> Century as set by The National Academies, which is to “make solar energy

affordable". In addition to drastically cheaper cells, the non-energy intensive production method also means that these devices have a much faster energy payback of ~3 months as opposed to nearly 2.5 and 2 years for c-Si and p-Si respectively.<sup>6</sup> There is a significant reduction in the CO<sub>2</sub> footprint and the amount of hazardous chemicals used. Cheap perovskite solar cells offer us a future of abundant clean energy, in addition to having a reduced manufacturing CO<sub>2</sub> footprint we may begin to even use this excess energy to further reduce CO<sub>2</sub> in the atmosphere through the George Olah's Nobel Prize winning process of CO<sub>2</sub> recycling, which converts atmospheric CO<sub>2</sub> into storable energy in the form of methanol.

However, there has been one major drawback that has kept these devices from entering the market place, the problem of degradation. Although efficiency is high, and cost would be low, the Perovskite structure and composition used in PV devices are prone to degradation from many sources, chief among these are moisture, thermal, and interface interaction. I will delve more deeply into these in the next chapter.

## II. PEROVSKITE PHOTOVOLTAICS

A photovoltaic (PV) devices' ability to thrive on the market depends greatly on three criteria (dubbed "The Golden Triangle") cost, efficiency, and stability. With regards to stability, an acceptable optimal performance lifetime for a PV is 25 years.<sup>16</sup>

Unfortunately, there is no method available in which we can test a device for a brief period and from that information extrapolate out an accurate projection of its total lifetime and performance. What we can do is test the effects that short-term degradation has on it, as well as investigate the mechanisms of the materials degradation. This thesis will focus on the latter and will determine the effectiveness of various analytical tools and characterization techniques in uncovering the origins of degradation. To fix a problem one must first understand the problem, and in that spirit, the motivation of this thesis is to better understand the degradation problem. In this section we will first look at the structure and advantages of perovskites. Moving on we will discuss the operational mechanisms of Perovskite Solar Cells (PSC), the problem of degradation, and the current understanding of the core chemistry involved in the film decomposition. Lastly, we will look at the various characterization methods available.

### Perovskite properties and crystalline structure

Perovskites have an  $ABX_3$  where A is an organic cation, B (also referred to as M) is a metal cation, and X is a halide anion. The organic cations are commonly  $CH_3NH_3^+$ ,  $C_2H_5NH_3^+$ ,  $HC(NH_2)_2^+$ , the metal cations are typically divalent metal ions such as  $Pb^{2+}$ ,  $Eu^{2+}$ ,  $Cu^{2+}$ , and  $Sn^{2+}$ , and X being either a single halide or a combination of  $Cl^-$ ,  $Br^-$ , and  $I^-$  that surrounds the metal cation in an octahedral  $[BX_6]^{4-}$  cluster<sup>17-19</sup>. One of the most

commonly studied  $ABX_3$  combinations be, and the one that I will be using, is  $CH_3NH_3PbI_3$  (also denoted as  $MAPbI_3$ ). During heating the crystal structure of these materials undergo phase transitions from lower symmetry orthorhombic ( $Pnma$ ) to higher symmetry tetragonal ( $I4/mcm$ ), and cubic ( $Pm3m$ ) phases.<sup>17,19</sup> With  $MAPbI_3$  the transition from orthorhombic to tetragonal is  $\sim 162K$  and the transition to cubic occurs near the devices operating temperature at  $\sim 327K$ .<sup>17-19</sup>

The allure of PSC stems from its impressive increase in the power conversion efficiency (PCE). In the span of only 11 years the PCE rose from 2.19% in 2006, to 22.7% in 2017. Furthermore, the fabrication methods employed such as solution based coating, screen printing, spraying, and roll on roll processing are of interest because they are cheaper than any other PV device, thus dramatically reducing the Levelized Cost of Energy (LCOE), and allow for use of unconventional substrates.<sup>19</sup> This coupled with the ability to tune the material to a desired color, fitting in with a desired aesthetic, means that it has high potential for use as a Building Integrated Photo Voltaic (BIPV).<sup>19,20</sup> The dramatically rapid increase in perovskite PV PEC results from their outstanding intrinsic properties, such as excellent visible-light absorption, long carrier diffusion length, low exciton binding energy, low effective masses, and high carrier mobility and lifetime, which relate to its near ideal band gap and ambipolar nature.<sup>21</sup>

One of the alluring features of perovskites is the ability to tune the band gap. The band gap of this class of materials is largely determined by the  $[BX_4]^{6-}$ .<sup>19</sup> The optical absorption and photoluminescence is related to the halide (X) within the octahedral cluster. For example, when using iodine the result is a perovskite with a smaller bandgap and light emission at longer wavelengths than materials that employ bromide.<sup>19</sup> This

allows for the continuous tuning of the bandgap by using combinations of more than one halide.<sup>18</sup> UV-vis spectral data of the more commonly used MAPbI<sub>3</sub> show it to have a band gap of ~1.5eV, with an onset of absorption near 826nm (wavelength) and a valance band maximum (VBM) of -5.43. Not only is this VBM suitable for effective hole separation, the band gap is near the optimum PV performance band gap of 1.4 (as determined by the Shockley-Queisser limit).<sup>18,22</sup> We see in Figure 2.1.1 examples of how the band gap can vary with the different formulations of perovskite compounds.

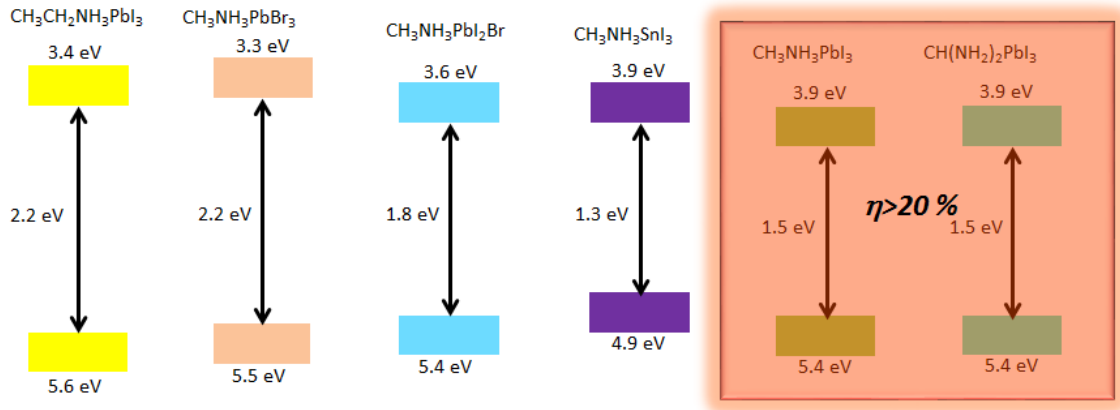


*Figure 2.1.1 range of bandgap to ABX<sub>3</sub> formulation. We see here the reported bandgaps for each formulation of perovskite, with MAPbI<sub>3</sub> highlighted for its ability to achieve PCE > 20%*

Two factors that contribute to perovskites high optical absorption one is its near optimal band gap and the other is its high joint density of states (JDOS), depicted in Figure 2.1.2. Although the bandgaps of GaAs and CH<sub>3</sub>NH<sub>3</sub>PbI<sub>3</sub> are both superior to Si PV, the perovskite still has superior absorption compared to GaAs. This is a result of its higher JDOS due to the lower part of its conduction band (CB) being primarily made up of Pb p band as opposed to CB of GaAs which is mainly delocalized s orbitals which exhibit a higher dispersion than p orbitals. Furthermore the perovskite benefits from its

edge transition coming from mixed-(Pb s, I p) to Pb p orbitals, where the Pb s to Pb p transition has a high probability, contributing to the VBM – CBM transition probability.<sup>23</sup>

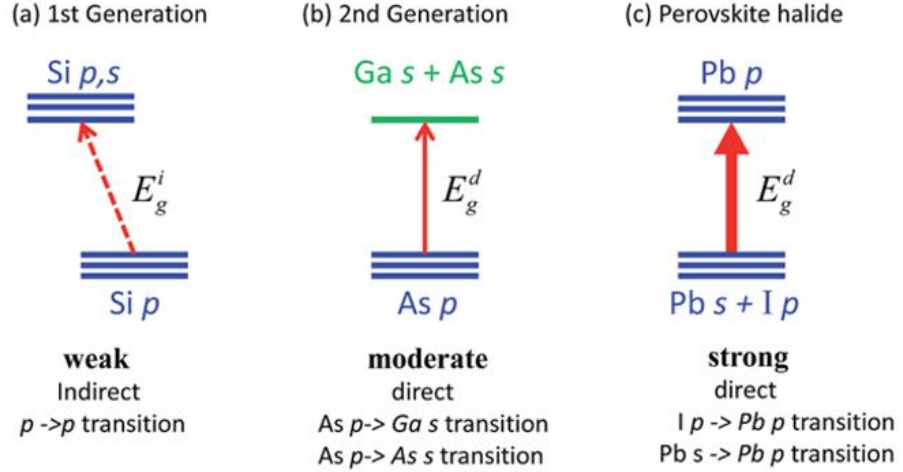


Figure 2.1.2 Depiction of the Joint Density Of States for 1<sup>st</sup>, 2<sup>nd</sup>, and 3<sup>rd</sup> generation solar cells.

The dispersion of the edges of the CBM and VBM determine the effective masses for electrons and holes which are inversely-proportional to their drift velocity. This means the lower the masses the more efficient the charge-carrier transport.<sup>21</sup> Spin-polarized DFT calculations by Giorgi *et al.* determined the effective masses of the hole and electrons to be small ( $m_e=0.23m_0$  and  $m_h=0.29$ ) showing long-ranged ambipolar charge transport property.<sup>19</sup>

Additionally, the effective masses for electrons and holes can be approximated by,

$$m^* = \hbar^2 \left[ \frac{\partial^2 \varepsilon(k)}{\partial^2 k} \right]^{-1} \quad (2.1.1)$$

where,  $\frac{\partial^2 \varepsilon(k)}{\partial^2 k}$  is the coefficient of the second-order term in a quadratic fit of  $\varepsilon(k)$  curve of the band edge.<sup>21</sup>

The aforementioned ambipolar nature means that perovskites not only act as photo absorbers, but also act as electron and hole transporters. This has been demonstrated in in experiments where the perovskite has been used in an electron transporter-free configuration.<sup>19</sup> This ambipolar nature is also apparent from the balanced diffusion lengths of the electrons and holes, for example MAPbI<sub>3</sub> exhibited electron and hole diffusion lengths are estimated as 130nm 100nm respectively. Further, Dong *et al.* found that the diffusion lengths for single crystal are an incredible 175 $\mu$ m.<sup>24</sup>

The diffusion length is given by,

$$L_D = (D \tau)^{\frac{1}{2}} \quad (2.1.2)$$

where the Diffusion coefficient (D) is related to the mobility ( $\mu$ ) by,

$$D = \mu \left( \frac{kT}{q} \right) \quad (2.1.3)$$

This indicates the average distance that a charge carrier can travel through a film before recombination takes place. If the film is thicker than the diffusion length, then the charge will not be extracted by its appropriate transport layer making this a crucial piece of information when determining the film thickness of a device. Most solution processed materials have diffusion lengths  $\sim$ 10nm which is much smaller than the 100nm  $L_D$  of MAPbI<sub>3</sub>. Yin *et al.* found that the long electron-hole diffusion length and high open-circuit voltage are partially explained by the strong Pb lone-pair *s* orbital and *I p* orbital antibonding coupling and the high ionicity of CH<sub>3</sub>NH<sub>3</sub>PbI<sub>3</sub>. This leads to the dominant

intrinsic defects creating only shallow level traps, depicted in Figure 2.1.3, that carriers can easily be liberated from.<sup>25</sup>

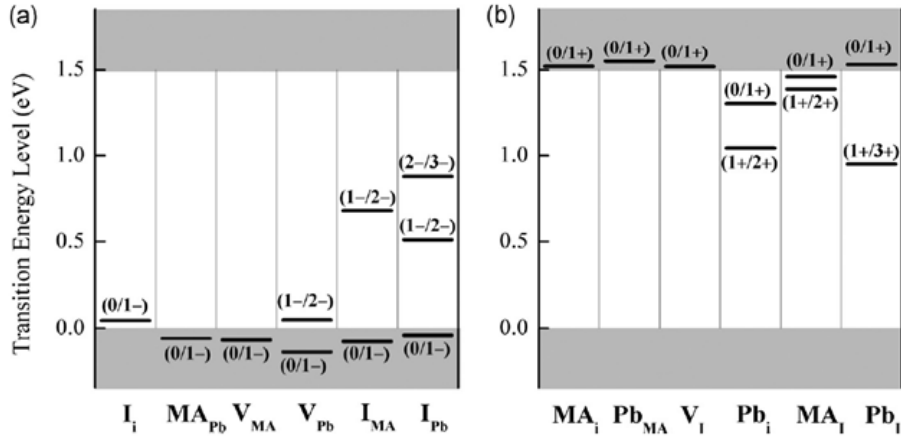
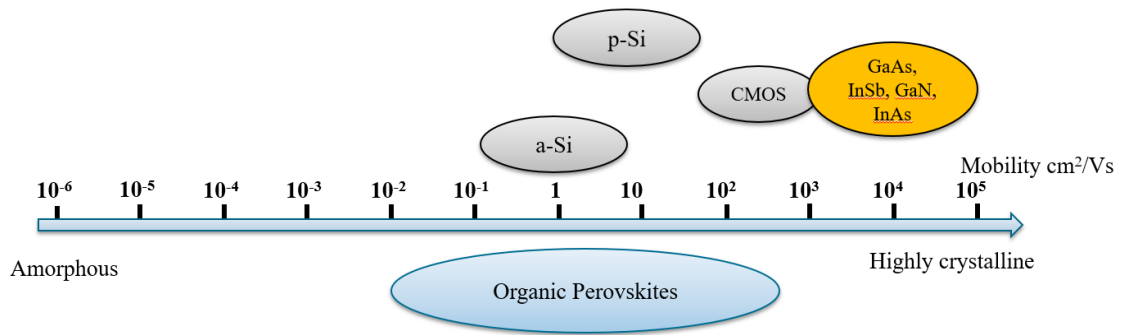


Figure 2.1.3 Shallow traps of MAPbI<sub>3</sub> in (a) the lower and (b) upper bands.<sup>25</sup>

Long diffusion lengths also stem from (and thus indicate) a combination of both low charge carrier recombination rates and high charge carrier mobilities. Perovskites have shown a remarkably high charge carrier mobility. Frost *et al.* estimated the MAPbI<sub>3</sub> electron mobility to be 66 cm<sup>2</sup>/Vs.<sup>22</sup> However the mobility seems to depend significantly on the film morphology as depicted in Figure 2.1.4, spanning from 0.01 cm<sup>2</sup>/Vs to 300 cm<sup>2</sup>/Vs for samples with higher crystallinity. The long L<sub>D</sub> coupled with perovskites low exciton binding energies, ranging from 19 to 50 meV for MAPbI<sub>3</sub>, also explains its good performance in a thin film configuration. Additionally, the low exciton binding energy indicates that there may be charge separation taking place within the absorber.



**Figure 2.1.4 Perovskite Mobility.** Here we see that Perovskite has a wide range of electron mobility. This can vary greatly depending on film morphology.<sup>20</sup>

Despite this plethora of beneficial properties that has made perovskite such an intriguing material for PV use there are some environmental concerns regarding the use of lead in these films. However, it is worth noting that despite the potential for harm lead is already successfully used in car batteries without producing negative environmental hazards. Additionally, the amount of lead used in a MAPbI<sub>3</sub> PV is so miniscule that it is already present in a slab of soil only 1 cm thick as seen in the Figure 2.1.5. Furthermore the 8.7kg of lead found in a single car battery is sufficient to create 5 acres of MAPbI<sub>3</sub> solar cells.<sup>26</sup> This means that instead of looking for replacements for lead we can focus on the nemesis of degradation which holds PSC back from being viable on the market.

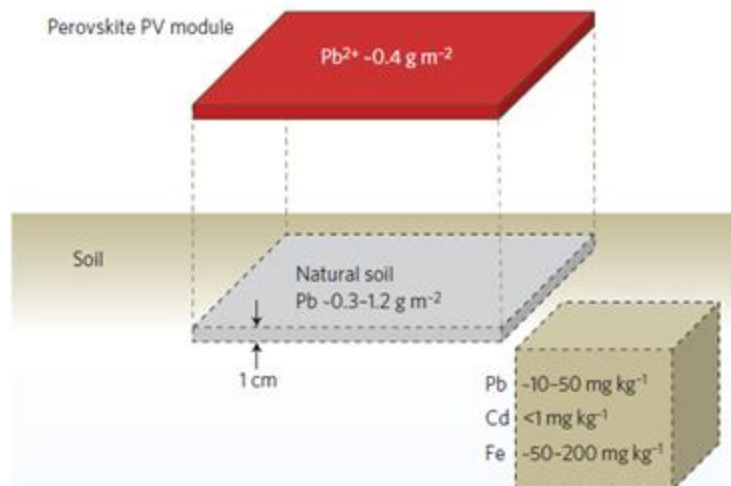


**Figure 2.1.5 Amount of lead contained in a perovskite PV module and in natural soil.** Areal content of lead in a perovskite solar module (red) and in natural soil (grey). A slab of soil (dashed lines) with a thickness of 1 cm contains as much lead as a perovskite solar module. Weight contents in soil of lead, cadmium and iron are also reported (lower right), which are naturally occurring.<sup>26</sup>

### Perovskite degradation and the challenges of stability

There are several factors that can affect the chemical balance and cause, or contribute to, the degradation of the perovskite film. Among these are heat, photo effects, contact with various solvents ( $H_2O$ , DMF, IPA, etc.), and interface properties. Some of these are less severe and/or more manageable than others (e.g. moisture easily degrades the film, yet encapsulation provides a sufficient barrier between the film and the outside air). The causes of degradation that we will be focusing on will be thermal, atmospheric, and interface effects.

## Thermal Degradation

Thermal degradation arises from intrinsic thermal instability of the material and can also be the result of the use of unstable interface layer. One of the primary intrinsic qualities of perovskite that results in thermal degradation is its extremely low thermal conductivity. Pisoni *et al.* showed that at room temperature the thermal conductivity ( $\kappa$ ) of MAPbI<sub>3</sub> is 0.5 W/(Km) and 0.3 W/(Km) for single crystals and polycrystals respectively.<sup>27</sup> With such low conductivity, even the light-deposited heat is prevented from rapidly spreading out. This trapping of heat results in mechanical stress that can begin to degrade the film.

This ultralow thermal conductivity of MAPbI<sub>3</sub> results from its unique crystal structure involving the slowly rotating MA<sup>+</sup> cations within the unit cell. The disorder of the MA<sup>+</sup> sublattice that is easily excited even at temperatures below 160K.<sup>27</sup>

Even with environmental temperature of 40°C The accumulation of heat easily reaches temperatures of 85°C, which has an average thermal energy of 0.093 eV. Since this is close to formation energy per unit cell in perovskite films (such as MAPbI<sub>3-x</sub>Cl<sub>x</sub> were the formation energy per unit cell was calculated to be 0.11~0.14eV) the instability of individual unit cells and degradation over time can be expected even at 85°C<sup>28</sup>.

Temperatures as low as 85°C acting as the only stressor are all that is needed to create instability in the film. Although the rate of degradation is influenced by the atmosphere in which it is taking place such as oxygen and water, they are not necessary for the initiation and continuation of film decomposition.<sup>28</sup>

Knudsen Effusion Mass Loss experiments (KEMML) as well as Thermogravimetric Analysis (TGA) were used to study the thermal behavior of MAPbX<sub>3</sub>(X=I or Cl). They

both demonstrated that the decomposition reactions occur with the organic component of the perovskite thermally decomposing resulting in the loss of gaseous methylamine (MA) and the corresponding hydrogen halide HI (not by phase separation of solid lead (II) halides and methylammonium halides).<sup>29,30</sup>



### Moister and Atmospheric Degradation

A water molecules small size allows it to enter the  $\text{MAPbI}_3$  structure where, due to its polarized configuration, it is trapped between the  $\text{MA}^+$  and  $[\text{PbI}_3]^-$  ions with oxygen pointing to the  $\text{MA}^+$  and hydrogen towards  $[\text{PbI}_3]^-$ . With the assistance of thermal energy, the water molecule will then disrupt the Pb-I bond by entering between two of the iodine atoms of  $[\text{PbI}_3]^-$  where, due to the coulombic repulsion between oxygen and iodine, it then pushes the iodine away resulting in liberation of the organic component<sup>21</sup>.



The isolated and negative charged iodine then catches a proton from the  $\text{NH}_3$  group in the  $\text{MA}^+$  to form HI,



The HI is then subject to degradation from both UV light as well as the presence of oxygen, with the redox reaction being,



And the photochemical reaction being,



Both reactions further drive degradation forward with the only biproduct remaining on the substrate being  $\text{PbI}_2$  and trace amounts of  $\text{I}_2$ .<sup>21</sup> This process can be seen in Figure 2.2.1 below.

**Note:** Replacing  $\text{I}^-$  with  $[\text{BH}_4]^-$  can make the negative charge be shared by many H atoms so that the attraction between anion and the water molecule decreases.<sup>31</sup>

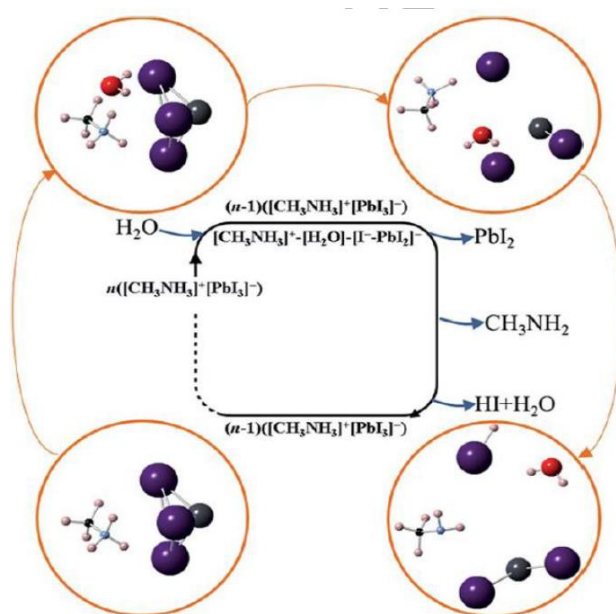


**Figure 2.2.1** Degradation mechanism of MAPbI<sub>3</sub> exposed to moisture. The lead back, purple, cyan, black, red and pink balls represent Pb, I, N, C, O and H, respectively.

Additionally, both Jarvest M. Frost *et al.* and Walsh and coworkers reported that moisture assisted degradation can result from acid-base reactions between water and the ammonium component of the organic compound.<sup>32,33</sup> In this case the water molecule, acting as a Lewis base, combines with MAPbI<sub>3</sub> to acquire a proton from the ammonium  $(\text{NH}_4)^+$  forming the intermediates  $[(\text{CH}_3\text{NH}_3^+)_{n-1}(\text{CH}_3\text{NH}_2)_n\text{PbI}_3][\text{H}_3\text{O}]$

which then decompose into HI, CH<sub>3</sub>NH<sub>2</sub>, resulting in PbI<sub>2</sub> being the only remaining biproduct remaining on the film.

Furthermore, Mosconi and coworkers looked at how moisture interacts with the interfacial surface of MAPbI<sub>3</sub> with different terminations, these being MAI-terminated, PbI<sub>2</sub>-terminated, and PbI<sub>2</sub>-defect- terminated, depicted in Figure 2.2.2

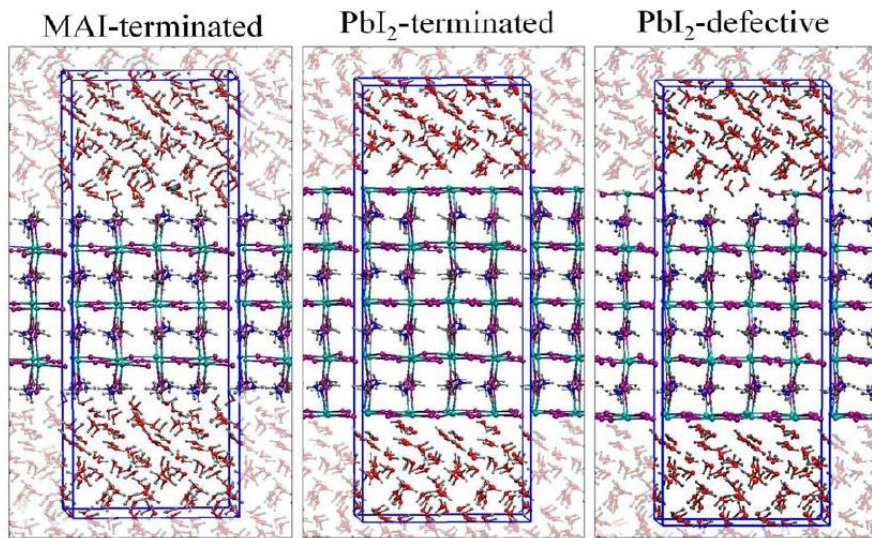


*Figure 2.2.2 Hydrated MAI- and PbI<sub>2</sub>-terminated and PbI<sub>2</sub>-defective perovskite slabs. The simulation cell is highlighted in blue.*

With regards to the MAI-terminated interface it was found that these surfaces allow for the ease infiltration of water due to the strong affected of the CH<sub>3</sub>NH<sub>3</sub><sup>+</sup> cations orientation near to the surface.<sup>21</sup> As discussed earlier, there is dissolution of the Pb-I bonds due to the interplay between H<sub>2</sub>O and Pb. Once water infiltrates the surface it begins to degrade the whole structure of the film.

The defected  $\text{PbI}_2$ -terminated film doesn't fare much better since there are still areas of the film with MAI in direct interfacial contact with the water which acts as a similar vector for decomposition.

The  $\text{PbI}_2$ -terminated surfaces are less sensitive to interfacial water due to this facet possessing significantly stronger Pb-I bonds. It is proposed that the incorporation of water at this surface may assist in creating an intermediate hydrated phase that could add to the films stability. However, due to weakening in the Pb-I bonds caused by electronic excitation when the film is exposed to sunlight, water can still absorb in these surfaces and initialize the degradation process.<sup>21</sup>

### **Interfacial degradation**

Degradation can also arise from the ETL and/or HTL used in the device structure. One such example is that of ZnO, which has been used as an effective ETL in producing high PEC (>15%) PSCs. It was chosen due to its high electron mobility (>1  $\text{cm}^2/(\text{V}\cdot\text{s})$ ), It possess an electron affinity that is nicely aligned with the valence band edge of  $\text{MAPbI}_3$ , and it is optically transparent due to its large band gap (3.3eV). However, even with these favorable characteristics, these devices have been shown to negatively affect the stability of the  $\text{MAPbI}_3$  absorber layer at temperatures >90°C.<sup>34</sup>

DFT calculation have shown that this issue arises from deprotonation of the perovskite film at the ZnO interface at which point The MA leaves the film as a gas.



This degradation can then continue throughout the bulk of the film as the reactive iodine ion could steal a proton from the NH<sub>3</sub> group in the MA<sup>+</sup> to form HI.<sup>34</sup>

After deprotonation has taken place any remaining solvent such as IPA can further exacerbate the problem as it may react with it to form propene and water



And as stated earlier the present of water dramatically promotes degradation of the film.

**Note:** In the case of Restrictive Volume Solvent Annealing (RVSA) the methylamine stays near the PbI<sub>2</sub> biproduct allowing for the possibility of recombination.<sup>35</sup>

### III. CHARACTERIZATION METHODS

#### Ellipsometry

Spectral Ellipsometry is an optical characterization technique that is used to measure the thickness, surface roughness, and optical constants of thin film materials. This process starts with unpolarized light which is then linearly polarized before being directed at the target sample. The linearly polarized light is then reflected off the target sample at which point its polarization state becomes elliptical. Ellipsometry takes advantage of the fact that this change in polarization is unique to the samples physical properties and optical constants and by measuring the change in polarization we can indirectly determine this information. To better understand this process, we must first look at the nature of polarized light, and the way in which thin film material interact with light waves to change their polarization. Moving on we will look at how SE uses this change in polarization to determine information about the film stack and its optical constants. Lastly, I will show how we are able to create an accurate model for  $\text{PbI}_2$ ,  $\text{MAPbI}_3$  and characterize the gradual degradation of the Perovskite film into  $\text{PbI}_2$

#### Polarization

Although light poses a transverse nature, with both an electric field and a magnetic field oscillating orthogonally with one another, frequencies in the visible part of the spectrum the interaction with material is mainly through the electric field. Therefore we here focus only on the electric components of the light. Polarized light can be described as the superposition of two linearly polarized plane waves, one oscillating

along the y-axis, or plane of incidence, and the other oscillating along the x-axis while both moving in the z-direction. If two waves are in phase, then the result is linearly polarized light. When the two waves have equal amplitude yet are  $90^\circ$  out of phase we have circularly polarized light. Further if these waves have either different amplitudes or arbitrary phases this creates elliptically polarized light. In Figure 3.1.1a we see the  $\mathbf{E}$  field of a linearly polarized electromagnetic wave as it propagates and is projected on the screen (Figure 3.1.1b). Figure 3.1.1c depicts circularly polarized light which the result of  $E_x$  and  $E_y$  having the same amplitude but being  $90^\circ$  out of phase causing the  $\mathbf{E}$  vector to rotate and its end point tracing a circle. Lastly, Figure 3.1.1d is elliptically polarized which is the general result of the x and y components being out of phase and/or having different amplitudes.

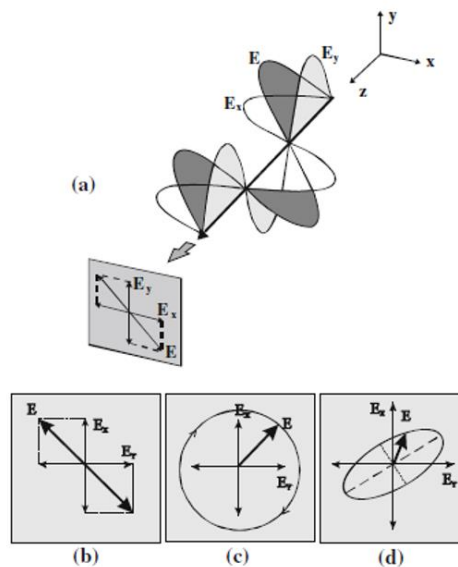


**Figure 3.1.1** Various polarization states of a monochromatic light wave. with  $E$  field projections in the  $x$  and  $y$  planes yielding  $E_x$  and  $E_y$  we see, (a) linearly or plane polarized light, (b) projected by linearly polarized light, and (c) circularly polarized light: d elliptically polarized light.<sup>36</sup>

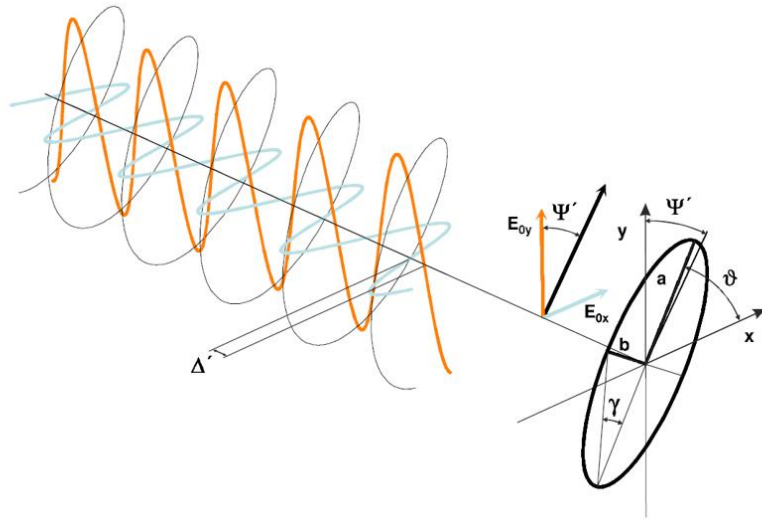


*Figure 3.1.2 Elliptically polarized light and the projected polarization ellipse. Mathematically the polarization state is defined by  $\Psi/\Delta$  the amplitude quotient and phase difference, and  $\psi/\gamma$  which is the azimuth angle and ellipticity.<sup>37</sup>*

The x and y components of elliptically polarized light, as depicted in Figure 3.1.1-2, are

$$E_x = E_{0x} e^{i(kz - \omega t)} e^{i\delta_x} \quad (3.1.1)$$

$$E_y = E_{0y} e^{i(kz - \omega t)} e^{i\delta_y} \quad (3.1.2)$$

Where  $k$  is the scalar of the wave vector and  $\omega$  is the angular frequency

$$k = \frac{2\pi}{\lambda} \quad (3.1.3)$$

$$\omega = 2\pi\nu \quad (3.1.4)$$

The polarization state is therefore already fully defined by only two parameters:

The relative amplitude is given by,

$$\tan \Psi = \frac{E_{0x}}{E_{0y}} \quad (3.1.5)$$

and phase is

$$\Delta = \delta_x - \delta_y \quad (3.1.6)$$

As you would expect from its name, Spectral Ellipsometry, it measures the change of the state of polarization of light beam upon reflection. This information is used to determine information about the sample under study. Although the light is linearly polarized before it makes contact with the target, the physical properties of the sample alter and deform it such that the resultant reflected light is now in an elliptical state. In Figure 3.1.3 we see a linearly polarized incident beam where  $\mathbf{E}$  is depicted in its x and y components  $\mathbf{E}_{is}$  and  $\mathbf{E}_{ip}$  respectively. The plane of incidence (POI) normal to the surface that  $\mathbf{E}$  will be reflecting off of.  $\mathbf{E}_{ip}$  and  $\mathbf{E}_{is}$  are parallel and orthogonal to the POI, respectively. With the subscript p for parallel and s for “senkrecht” the German word for perpendicular.

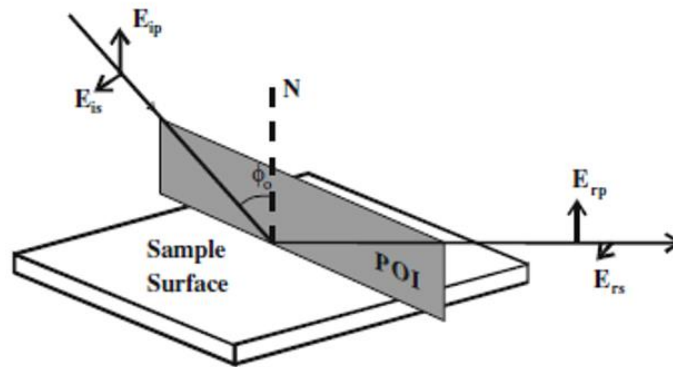


**Figure 3.1.3 Reflection of polarized light.** Incident linearly polarized light with orthogonal electric field components  $E_{ip}$  and  $E_{is}$  reflected at incident angle  $\phi_0$  yielding reflected components  $E_{rp}$  and  $E_{rs}$ . The plane of incidence (POI) contains the surface normal  $N$  and the incident ray. <sup>36</sup>

The elliptical shape of the reflected light can be expressed with respect to the ratio of p and s-polarized light as introduced above. The reflected light that oscillates parallel to the plane of incidence, is known as p-polarized light ( $r_p E_p$ , where  $r_p$  is the Fresnel reflection coefficient of p-polarized light, and  $E_p$  is the electric field amplitude of the p-polarized light incident on the sample), whereas the reflected light that has an electric field that oscillates perpendicular to the plane of incidence, is known as s-polarized light ( $r_s E_s$ , where  $r_s$  is Fresnel reflection coefficient of s-polarized light, and  $E_s$  the electric field amplitude of the s-polarized light incident on the sample). The effect of the sample is summarized by the ratio of the complex field amplitudes of the reflected light  $\rho$

$$\rho = \frac{R_p}{R_s} = \tan(\Psi) e^{i\Delta} \quad (3.1.7)$$

With  $\tan(\Psi)$  describing the difference in reflection of the p- and s-component of the light, and  $\Delta$  describing the relative phase shift for p and s-polarized light upon reflection. For incident linearly polarized light  $\tan(\Psi)$  is the magnitude of the ratio and  $\Delta$  gives the oblique shape of the ellipse, which is determined by the phase difference between the p and s-plane light. These two parameters are measured with respect to the discrete wavelengths of the reflected light and allow us to build a model that represents our sample structure and then we fit the parameters of the model to the collected data.

### **Light-matter interaction**

There are two primary ways in which light and matter interact with one another, refraction and absorption. Refraction can be used to describe the way in which light is redirected through a materials interphase as well as the way in which it is reflected from a

sample. Absorption is related to a materials bandgap, which governs what wavelengths of light are absorbed by a material. Both of these are properties of the Fresnel reflection coefficients for the perpendicularly polarized and parallel polarized reflected light,  $r_s$  and  $r_p$  respectively. Maxwell's equations and the boundary conditions for a planar interface provide expressions for the Fresnel reflection coefficients

$$r_p = \frac{\vec{E}_{rp}}{\vec{E}_{ip}} = \frac{\tilde{N}_1 \cos \phi_0 - \tilde{N}_0 \cos \phi_1}{\tilde{N}_1 \cos \phi_0 + \tilde{N}_0 \cos \phi_1} \quad (3.1.8)$$

and

$$r_s = \frac{\vec{E}_{rs}}{\vec{E}_{is}} = \frac{\tilde{N}_0 \cos \phi_0 - \tilde{N}_1 \cos \phi_1}{\tilde{N}_0 \cos \phi_0 + \tilde{N}_1 \cos \phi_1} \quad (3.1.9)$$

Here  $\tilde{N}$  is known as the complex refractive index

$$\tilde{N} = n + ik \quad (3.1.10)$$

Where  $n$ , the real part of  $\tilde{N}$ , is the refractive index and  $k$  is the absorption index, also known as the extinction coefficient.

Additionally, the angles  $\phi_0$  and  $\phi_1$  are related to each other through Snell's Law

$$n_1 \sin \phi_1 = n_2 \sin \phi_2 \quad (3.1.11)$$

Further, these Fresnel reflection coefficients,  $r_p$  and  $r_s$  are related to the complex reflectivity ratio  $\rho$  through the Pseudo-Fresnel reflection coefficients,  $R_p$  and  $R_s$ .

Where, for a single film on a bulk substrate

$$R_p = \frac{r_{01} + r_{12} e^{i2\beta}}{1 + r_{01} r_{12} e^{i2\beta}} \quad (3.1.12)$$

Here  $\beta$  is the phase, or optical, thickness of the film and is expressed as,

$$\beta = 2\pi\tilde{N}_1 \frac{d}{\lambda} \cos \phi_1 \quad (3.1.13)$$

Where  $d$  is the film thickness and  $\lambda$  is the incident wavelength.

We now see how, through the complex reflectivity ratio ( $\rho$ ),  $\Delta$  and  $\Psi$  are related to the refractive index ( $n$ ), absorption coefficient ( $k$ ), and thickness ( $d$ ) of a film.  $\tilde{N}$  is related to the complex dielectric response function

$$\tilde{\epsilon} = \epsilon_1 + i\epsilon_2 \quad (3.1.14)$$

Where,

$$\tilde{N} = \sqrt{\tilde{\epsilon}} \quad (3.1.15)$$

And,

$$\epsilon_1 = n^2 - k^2 \quad , \quad \epsilon_2 = 2nk \quad (3.1.15)$$

The optical constants  $n$  and  $k$  give us the optical properties of a material in regard to how an electromagnetic wave will propagate through it. The real part,  $n$ , tells us about the speed of the EM-wave relative to vacuum, and  $k$  tells us more about the absorption of the EM-wave. The parameter  $\tilde{\epsilon}$  contains the same information but relates to how the material's polarization will respond to an applied electric field.

### **Regression analysis**

Although  $\Delta$  and  $\Psi$  are equal to an expression that contains the various optical properties that we may be interested in, we cannot simply calculate those constants

directly from the measured values of  $\Delta$  and  $\Psi$ . We can however calculate values of  $\Delta$  and  $\Psi$  with given values of the materials properties and other information on the thin film stack such as film thickness and roughness. This allows us to create optical models with which we can generate calculated values of  $\Delta$  and  $\Psi$  to compare to the experimental values. The basic process is depicted in Figure 3.1.4 and goes as such. First, we measure the target sample and system records the experimental values  $\Delta_{ex}$  and  $\Psi_{ex}$ . Second, we use the CompleteEase software to create a layered optical model by inputting known or accepted values of the samples optical parameters. Other parameters that we are not sure of and want to test for the values that may be more accurate we call “fit parameters”, for these we simply specify the likely range that we believe to contain a correct. Next the software calculates the values  $\Delta_c$  and  $\Psi_c$  for the optical model, at which point it compares  $\Delta_c$ ,  $\Psi_c$  to  $\Delta_{ex}$ ,  $\Psi_{ex}$  and determines which values give the lowest Mean Square Error (MSE). Lastly, if the MSE is unsatisfactory (typically being a value greater than 10) the user then manually adjusts the parameters of the optical model until the  $\Delta_c$ ,  $\Psi_c$  and  $\Delta_{ex}$ ,  $\Psi_{ex}$  values are in more agreement with one another.

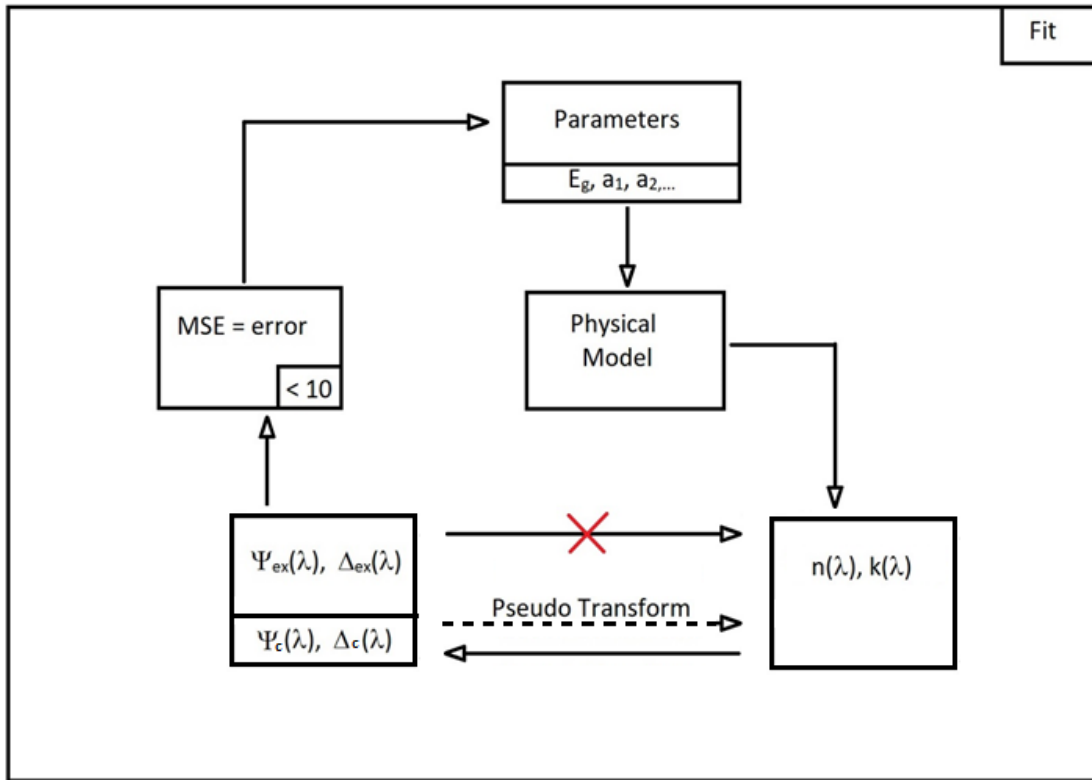


**Figure 3.1.4 The regression analysis process.** Here the user must build the optical model which is then compared to the  $\Psi$  and  $\Delta$  measured from the elliptical light reflected off of the sample.

A low MSE value isn't the only aspect of a model that determines its adequacy, the parameters used must undergo further scrutiny to ensure that they are providing a unique fit. In total we must have a low MSE  $< 10$ , all variations in the parameters must be less than 10 percent of the fit values, and all parameter correlations must be  $< |0.9|$ , and the  $n$  and  $k$  values must make physical sense. Additionally, we must make sure to minimize the number of parameters to help ensure a more unique and accurate fit. In Figure 3.1.5 we see that there are many local minima for a single parameter, in this case the parameter being thickness.

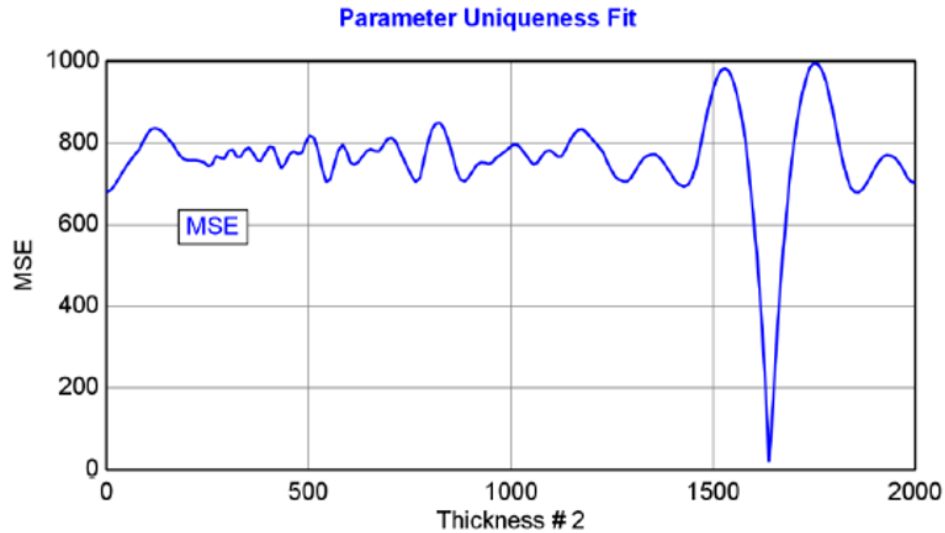


*Figure 3.1.5 Single Parameter uniqueness fit. In this example, from the CompleteEase software manual, we see the MSE changes as the software varies the parameter from 0 to 2000, looking for the lowest fit. Here there is one true fit is ~1700nm, however if the fit range was reduced 0-1500nm the software would settle at the lowest local minima.*

However, when we have a large number of oscillators and subsequent parameters then the MSE vs the aggregated parameters look more like the following graph in Figure 3.1.6 where it is more difficult to determine if you're within the bounds of the true minimum.

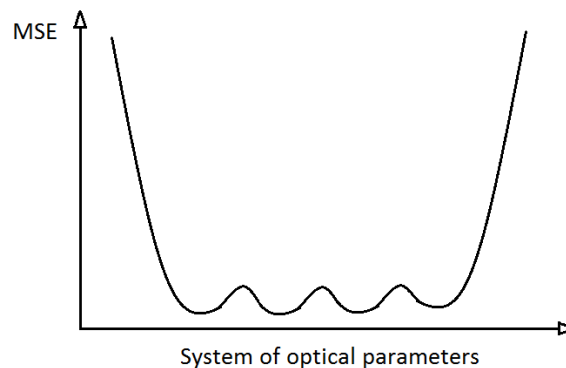


*Figure 3.1.6 Multi parameter uniqueness. When a large number of parameters it is possible for a large range of parameter values to return a low MSE even if they are incorrect and non-unique. This is why it is very important to observe the error range of each parameter to ensure that all, or at least most, have errors of <10%.*

The main advantage of ellipsometry measurements is that it is a non-destructive, non-invasive, and a non-contact characterization method, this is especially useful for the purposes of this thesis since the perovskite films that are being investigated are extremely prone to degradation. Additionally, it is precise, reproducible, and very sensitive for ultra-thin films (<10 nm) as long as one knows the material's optical properties. This technique is applicable to almost any thin film (polymers, semiconductors, dielectrics, metals, alloys, etc.) and is ideal for in-situ applications.

### **Sample Preparation**

Since the goal is to see how effectively SE can measure the  $\text{PbI}_2$ , which is the byproduct of the degraded perovskite, within the  $\text{MAPbI}_3$  film I first had to ensure that am using correct models for  $\text{MAPbI}_3$  and  $\text{PbI}_2$ . To do this I had to create two samples a  $\text{PbI}_2$  film on silicon (Si) and an  $\text{MAPbI}_3$  film on Si. After the parameters of the two independent models were determined I could then make, and test, a  $\text{PbI}_2/\text{MAPbI}_3/\text{Si}$  film stack.

The procedure for forming the perovskite films went as such. First, we prepared the inks and the substrates. The substrates that we used were 1x1 inch silicon (Si) slide that were cleaned in a sonicator for 20 minutes while immersed in a Deconex OP 121 (5 wt.% in DI water) solution and then exposed to an  $\text{O}_2$  plasma (Harrick Plasma, Pdc-32G,

RF power 18W) for 10 minutes. Afterwards, they were transferred into a Nitrogen Glovebox for deposition.

The deposition ink/solution is made in three steps, the first two steps involve making a one molar  $\text{PbI}_2/\text{MAI}/\text{DMF}$  solution. Here I would put 461mg of  $\text{PbI}_2$  and 1 mL of DMF in a small, clear, glass vile with a magnetic stirring bar and the place it on a hotplate set to  $70^\circ\text{C}$ . After about 10 minutes the  $\text{PbI}_2$  would completely dissolve. At this point I would then take the vile and insert 159mg of MAI and return the vile to the hotplate for an additional 10 minutes. Even after the MAI is fully dissolved the solution still has a somewhat cloudy appearance. In a second vile I would then place 91mg of MAAC, the purpose of which it to slow the rate of film formation and crystal growth, allowing for larger crystals to form during annealing. The  $\text{PbI}_2/\text{MAI}/\text{DMF}$  solution is placed in a syringe affixed with a  $1\mu\text{m}$  particle filter through which it is transferred into the vile containing the MAAC. After  $\sim 15$  minutes of occasional stirring the MAAC is completely dissolved and the ink is ready for deposition. Next, in the  $\text{N}_2$  glovebox, I would deposit 85mL of the ink on the Si substrates and spincoat them at 4000rpm for 60 seconds. They were then removed from the glove box and placed in a humidity chamber, set to 35% humidity, where they were annealed on a  $100^\circ\text{C}$  hotplate for 5 minutes.

The  $\text{PbI}_2$  film for the sample of  $\text{PbI}_2$  on Si and the layered  $\text{PbI}_2/\text{MAPbI}_3/\text{Si}$  sample was formed by means of thermal vapor deposition using a Trovato 300C vacuum thermal evaporator with a deposition rate of 0.1 nm/sec and base pressure  $5 \times 10^{-7}$  Torr. Using a Burker Profilometer the film thicknesses of the perovskite and the  $\text{PbI}_2$  were measured to be 270nm and 30nm respectively.

## Building the PbI<sub>2</sub> and MAPbI<sub>3</sub> models

Although the CompleteEase software comes preloaded with models for many common materials, and some materials that are less common, neither PbI<sub>2</sub> nor MAPbI<sub>3</sub> are included. I then had to proceed to build them using existing information from the literature.

When first building the model for the MAPbI<sub>3</sub> and PbI<sub>2</sub> looked to the literature to see what models have already been created. I found models for both materials from work published by Shirayama and coworkers.<sup>38</sup> The models were created using Tauc-Lorentz oscillators described by the following equations.

$$\varepsilon_{T-L}(E) = \varepsilon_{n1} + i\varepsilon_{n2} \quad (3.1.16)$$

$$\varepsilon_{n2} = \left[ \frac{Amp_n E o_n B r_n (E - E g_n)^2}{(E^2 - E o_n^2)^2 + B r_n^2 E^2} \cdot \frac{1}{E} \right] \quad E > E g_n \quad (3.1.17)$$

$$\varepsilon_{n2} = 0 \quad E \leq E g_n \quad (3.1.18)$$

$$\begin{aligned} \varepsilon_{n1} = & \varepsilon_1(\infty) + \frac{Amp_n B r_n}{\pi \xi^4} \frac{a_{ln}}{2\beta E o_n} \ln \left( \frac{E o_n^2 + E g_n^2 + \beta E o_n}{E o_n^2 + E g_n^2 - \beta E o_n} \right) - \frac{Amp_n}{\pi \xi^4} \frac{a_{tan}}{E o_n} \left[ \pi - \tan^{-1} \left( \frac{2E g_n + \beta}{B r_n} \right) + \right. \\ & \left. \tan^{-1} \left( \frac{-2E g_n + \beta}{B r_n} \right) \right] + 2 \frac{Amp_n E o_n}{\pi \xi^4 \beta} E g_n (E^2 - \gamma^2) \left[ \pi + 2 \tan^{-1} \left( 2 \frac{\gamma^2 - E g_n^2}{\beta B r_n} \right) \right] - \\ & \frac{Amp_n E o_n B r_n}{\pi \xi^4} \frac{E^2 + E g_n^2}{E} \ln \left( \frac{|E - E g_n|}{E + E g_n} \right) + \frac{2Amp_n E o_n B r_n}{\pi \xi^4} E g_n \ln \left[ \frac{|E - E g_n|(E + E g_n)}{\sqrt{(E o_n^2 - E g_n^2)^2 + E g_n^2 B r_n^2}} \right] \end{aligned} \quad (3.1.19)$$

where,

$$a_{ln} = (Eg_n^2 - E_p^2)E^2 + Eg_n^2Br_n^2 - Eo_n^2(Eo_n^2 + 3Eg_n^2) \quad (3.1.20)$$

$$a_{tan} = (E^2 - Eo_n^2)(Eo_n^2 + Eg_n^2) + Eg_n^2Br_n^2 \quad (3.1.21)$$

$$\xi^4 = (E^2 - \gamma^2)^2 + \frac{\beta^2 Br_n^2}{4} \quad (3.1.22)$$

$$\beta = \sqrt{4Eo_n^2 - Br_n^2} \quad (3.1.23)$$

$$\gamma = \sqrt{Eo_n^2 - \frac{Br_n^2}{2}} \quad (3.1.24)$$

Here there are 4 parameters per individual oscillator, Amp, Br, Eg, and Eo represent the amplitude, the peak broadening, the bandgap energy, and the peak transition parameter respectively. Additionally,  $\epsilon_1(\infty)$  is a constant contribution to the  $\epsilon_1(E)$  of all the oscillators.

When first applying this model to a MAPbI<sub>3</sub> sample and a PbI<sub>2</sub> sample the first resulted in MSEs of 31.183 and 10.798 respectively. I then allowed the software to fit each of the parameters listed in Table 3.1.1 which resulted in significantly better MSE results, 6.221 for MAPbI<sub>3</sub> and 1.139 for PbI<sub>2</sub>, however several of the parameters had very high errors (optimal parameter error is <10%) as seen in Table 3.1.1.

Material	Error(%)		Oscillator	Amp	Error(%)	Br	Error(%)	Eo	Error(%)	Eg	Error(%)
MAPbI <sub>3</sub>	MSE	6.221	1	0.6478	114.79623	3.112	83.717866	2.499	53.957583	0	0
	Thickness (nm)	317.95	2	42.5707	34.545004	0.139	4.3755396	1.596	0.5215539	1.549	0.2437702
	Roughness (nm)	7.05	3	2.3074	52.269221	0.592	14.831081	2.527	0.4907004	1.082	19.121996
	$\varepsilon(\infty)$	1.774	4	37.0445	90.292081	3.016	78.829576	2.632	17.207447	1.571	12.590707
	Angle Offset	0.0712	5	5.2423	278.60824	0.545	15.192661	3.221	1.393977	1.708	124.47307
			6	2.1211	448.59884	0.459	21.938998	3.5	1.2714286	1.782	216.4422
			7	1.9486	378.35318	0.652	24.52454	4.693	1.6322182	2.819	123.39837
			8	4.4158	474424.67	0.0001	87281500	6.253	866.4545	3.759	155458.44
			9	10.3024	7509.9913	0.883	6206.5459	6.625	186.42868	2.561	1283.6431
PbI <sub>2</sub>	MSE	1.139	1	1.0945	5.0781179	0.991	0.0001636	0.435	1.8395402	2.131	1.15E-05
	Thickness (nm)	46.24	2	145.9307	3.7766419	0.108	1.3185185	2.465	0.0253241	2.371	0.0661746
	Roughness (nm)	0.74	3	41.3767	25.205321	0.438	9.9315068	2.62	0.4122137	2.303	1.0594876
	$\varepsilon(\infty)$	1.686	4	43.7334	17.642077	0.473	3.5729387	2.889	0.225649	2.284	1.8870403
	Angle Offset	0	5	44.2522	18.303587	0.271	3.1738007	3.22	0.1635714	2.959	0.8313619
			6	57.5443	3.9223694	1.298	1.9799692	3.776	0.1639036	2.105	0.5415677
			7	30.2737	20.168562	0.535	1.6446729	4.372	0.1263266	3.318	3.4870404
			8	7.4531	14.935933	1.415	5.5194346	5.301	0.2641011	1.738	10.23015

**Table 3.1.1 Literature Parameters after fit.** The optimal parameter error is <10%. With so many parameters with such high error it is clear that these models lack uniqueness and the model must be reconstructed despite having a low MSE.

Using the current low MSE FIT I used the Parameterize Layer function with in the CompleteEase software and proceeded to build the model from scratch with very few oscillators so as to insure a more unique fit. I then fitted the new parameters to the sample data which returned a MSE of 1.471 and 7.034 for PbI<sub>2</sub> and MAPbI<sub>3</sub> respectively, with only 1 oscillator parameter for both the PbI<sub>2</sub> and MAPbI<sub>3</sub> having error values over 10%, as seen in Table 3.1.2. In Figure 3.1.7 we see the resultant n and k values of the models compared to values reported in the literature.

Material	Error(%)		Oscillator	Amp	Error(%)	Br	Error(%)	Eo	Error(%)	Eg	Error(%)
MAPbI <sub>3</sub>	MSE	7.034	1	10.5039	9.91374632	0.87	1.2183908	3.293	0.172335257	1.386	6.652236652
	Thickness (nm)	316.44	2	1.7314	3.35220053	0.716	0.88337989	2.561	0.107848497	0.00000001	241000000
	Roughness(nm)	2.3	3	67.7713	7.38901275	0.104	4.86153846	1.586	0.135372005	1.568	0.098086735
	$\varepsilon(\infty)$	1.451	4	25.5557	9.57535892	8.122	9.73282443	6.638	2.416390479	1.405	4.306049822
	Angle Offset	0.203									
PbI <sub>2</sub>	MSE	1.471	1	363.5349	3.07053326	0.111	1.18108108	2.441	0.037636624	2.395	0.034559916
	Roughness (nm)	0.06	2	73.5122	4.5988693	0.636	2.48427673	2.869	0.106936215	2.222	0.319306931
	Thickness (nm)	45.78	3	45.4934	20.7057287	0.3	4	3.232	0.205012376	2.934	1.049761418
	$\varepsilon(\infty)$	1.453	4	206.7515	7.39911923	1.313	2.23914699	3.595	0.322670376	2.884	1.25520111
	Angle Offset	0	5	19.7165	16.6228793	0.402	2.22462687	4.374	0.099794239	3.452	2.26825029
			6	6.5614	6.2945408	4.143	81.7016655	10.855	9.313680332	0	#DIV/0!

**Table 3.1.2 Parameters of the newly created models.** Here we see that the errors are significantly lower indicating a more unique model.

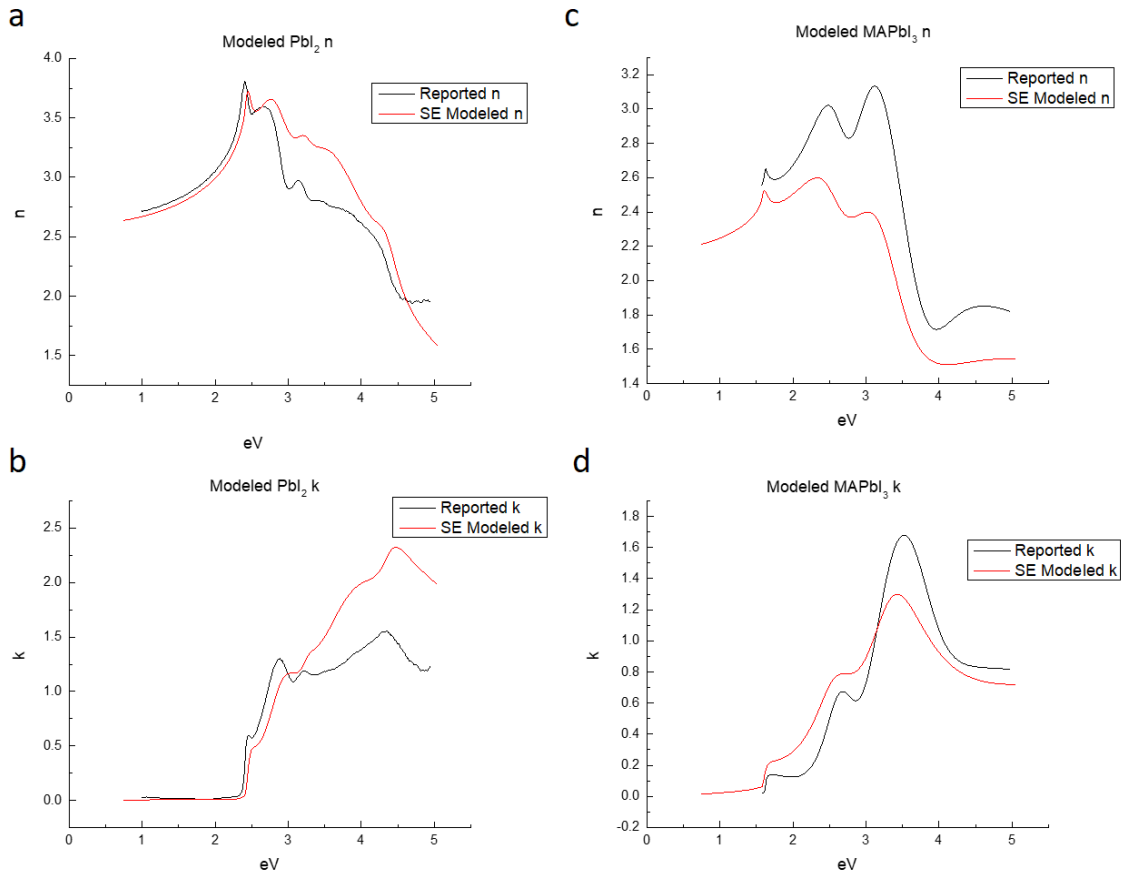


**Figure 3.1.7** Modeled  $n$  and  $k$  values vs the values reported in the literature. Notice that although the intensities may be different, the peaks and inflection points of the models of (a-b)  $\text{PbI}_2$  and (c-d)  $\text{MAPbI}_3$ , match nicely with the reported values.<sup>39,40</sup>

## Results

Finally, I applied and refit these models to the  $\text{PbI}_2/\text{MAPbI}_3$  layered sample resulting in an MSE of 4.631 with the measured vs modeled Psi and Delta appearing nearly identical, as seen in Figure 3.1.8. These too had few high-error parameters, as seen in table 3.1.3. Most importantly, besides having a low MSE and parameter errors, the models generated film thicknesses of the layers that were comparable to their actual, profilometer measured, values. For the  $\text{PbI}_2$  with a measured value of 30nm the model returned a value of ~32 nm and the 270 nm layer of  $\text{MAPbI}_3$  was modeled to have a thickness of ~291nm.

	Material	Error(%)	Oscillator	Amp	Error(%)	Br	Error(%)	Eo	Error(%)	Eg	Error(%)	
MSE	$\text{PbI}_2$											
4.631	Thickness (nm)	32.16	2.64	1	518.31	2.76	0.117	4.97	2.413	0.04	2.483	1.44E-06
Angle Offset	$\varphi(\infty)$	1.102	6.93	2	79.048	30.24	0.643	7.43	2.847	0.98	2.439	2.28
0.137				3	53.1799	27.29	0.4	9.25	3.717	0.46	3.378	1.58
Roughness(nm)				4	199.468	16.48	1.518	9.28	3.361	2.22	2.931	1.7
0.1				5	18.2844	41.28	0.397	6.24	4.392	0.27	3.629	4.43
				6	9.352	19.51	9	67.48	6	16.52	1.192	6.88
	$\text{MAPbI}_3$											
	Thickness (nm)	291.09	0.02	1	18.0727	7.68	1.23	2.82	3.317	0.27	1.45	4.58
	$\varphi(\infty)$	1.455	0.13	2	1.4118	4.08	0.64	1.02	2.552	0.16	0.0997	28.69
				3	76.4969	4.55	0.0988	2.48	1.601	0.08	1.574	0.07
				4	34.3146	4.64	8.148	122717.2312	4	2.975	1.485	1.88

**Table 3.1.3 Layered sample fit data.** Here we see that the fit values of the oscillator parameters of the  $\text{MAPbI}_3$  and  $\text{PbI}_2$  models provide a low MSE and low error, as well as accurate thickness measurements.

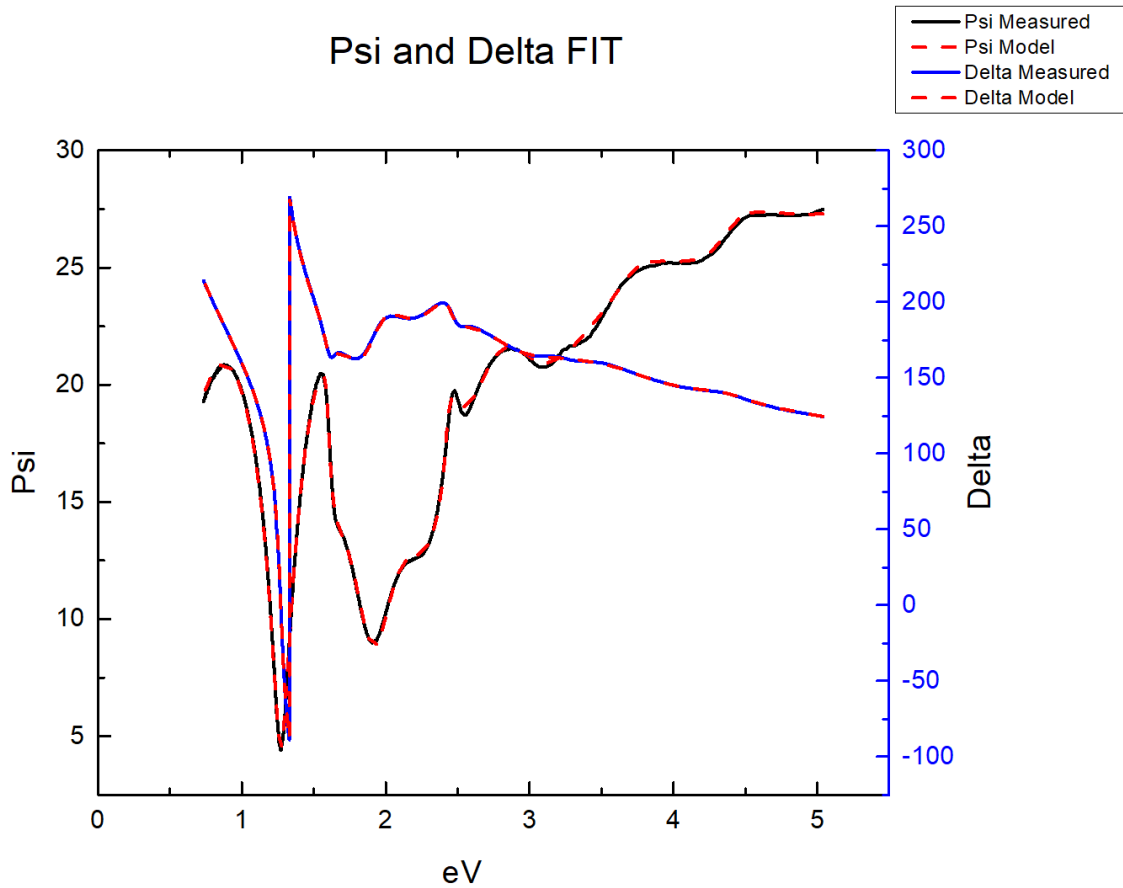


*Figure 3.1.8 Graph of the  $\Psi$  and  $\Delta$  model fit. The red dashed lines are the model generated  $\Psi$  and  $\Delta$ . As you can see by the way the dashed lines barely deviate from the actual  $\Psi$  and  $\Delta$  this is an outstandingly close fit.*

In Figure 3.1.9 we see further testament to the accuracy of the model fit is the Exp-Model Difference Graph, which subtracts the measured values from the model. Here we see very little deviation between the two sets. The difference between the  $\Psi$  values staying near zero, with variation between -0.4 and 0.2. The  $\Delta$  variation values between -4 and 2 are miniscule given this function itself ranges from -100 to 275.

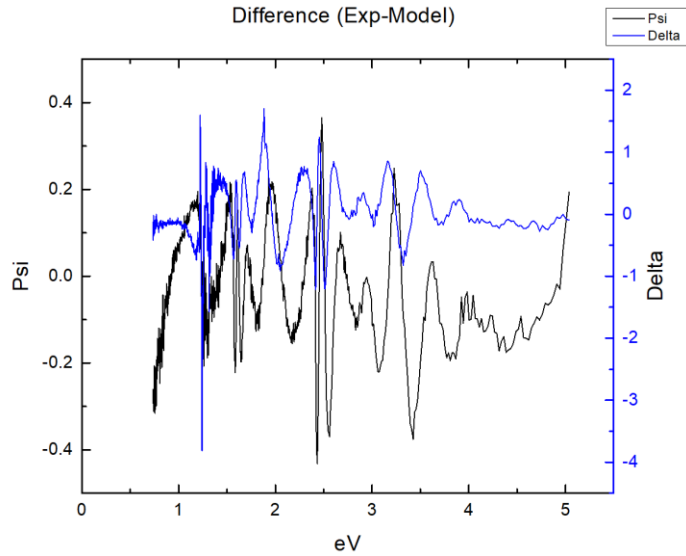


*Figure 3.1.9 The Difference between the measured and modeled values of  $\Psi$  and  $\Delta$ . Along with the calculated MSE, the difference graph provides the user with information about the deviation between the measured and modeled values of  $\Psi$  and  $\Delta$  with respect to eV.*

Furthermore, Figure 3.1.10 show the depolarization data which is used to check that the system has been properly calibrated, determined by having a depolarization less than ~5% throughout the whole spectral region.

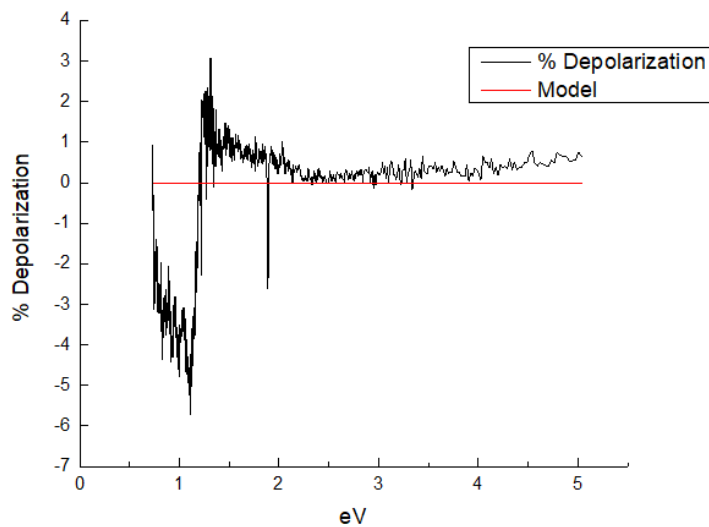


*Figure 3.1.10 System %Depolarization. Here we see that throughout spectral range (except for a downward spike around 1ev that extends to 5.7) the depolarization is <5%.*

## C-PL

In this section I will discuss the use of Confocal Photo Luminescent (c-PL) microscopy for characterization and imaging of thin film planar perovskite surfaces, as well as axial characterization. This method employs various lasers to provoke a photoluminescent response in a material and confocal imaging techniques to achieve high sample resolution. Since photoluminescence is dependent on a material's absorption and band gap we can take advantage of the differing bandgaps in samples that contain multiple materials to produce images that allow us to see the way in which inhomogeneous samples are intermixed.

Although this method is primarily used in biological samples it has found its place as an indispensable technique of choice for defect-band imaging and defect mapping for thin film photovoltaic technologies, such as Si, cadmium telluride and copper indium gallium selenide.<sup>41,42</sup> This is due in part to its high spatial resolution ( $<1 \mu\text{m}$ ) and its non-invasive nature.

Here I will apply this technique to study the structural and morphological defects of the perovskite film as well as the origin and spread of degradation within the axial plane. First, I will briefly discuss the concepts of photoluminescence and confocal imaging then I will delve into the anomalous intensities that we encountered while performing depth measurements on our thin-film samples before moving onto film preparation, experimental procedures, and results.

## Photoluminescence and Confocal Imaging

Photoluminescence is a response that a material has when it is in contact with light possessing an energy equal to or greater than the energy of the materials bandgap. The energy of the light is related to its wavelength through the following expression

$$E = \frac{hc}{\lambda} \quad (3.2.1)$$

When this happens, the photon excites an electron from the valance band to the conduction band, as the electron relaxes back to the valance band the material then emits a photon with a wavelength equal to the energy of the bandgap as depicted in Figure 3.2.1.

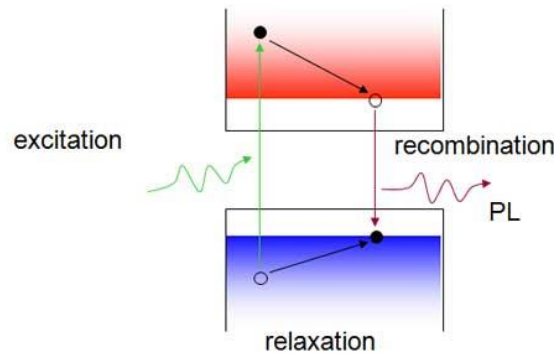


*Figure 3.2.1 Photoluminescence.* Here we see the absorption of a photon causing an electron to move from the valance band to the conduction band only to relax, causing the emission of a photon whose wavelength corresponds to the energy of the bandgap.

$$E_{ex} > E_{PL} \rightarrow \lambda_{ex} < \lambda_{PL} \quad (3.2.2)$$

Using the technique of confocal microscopy, we are then able collect the and record the intensity of these specific photons with a high degree of spatial resolution. This is achieved through the use of filters which insure that only photons with wavelengths specific to the materials PL emission are collected. In addition a pinhole in

the optical path is used to eliminate out of focus contributions. Below in Figure 3.2.2 we see the general schematic of the optical path. We can then apply this to mapping the degradation of MAPbI<sub>3</sub> films by taking advantage of the difference between the bandgaps of MAPbI<sub>3</sub> and the biproduct of its degradation, PbI<sub>2</sub>.

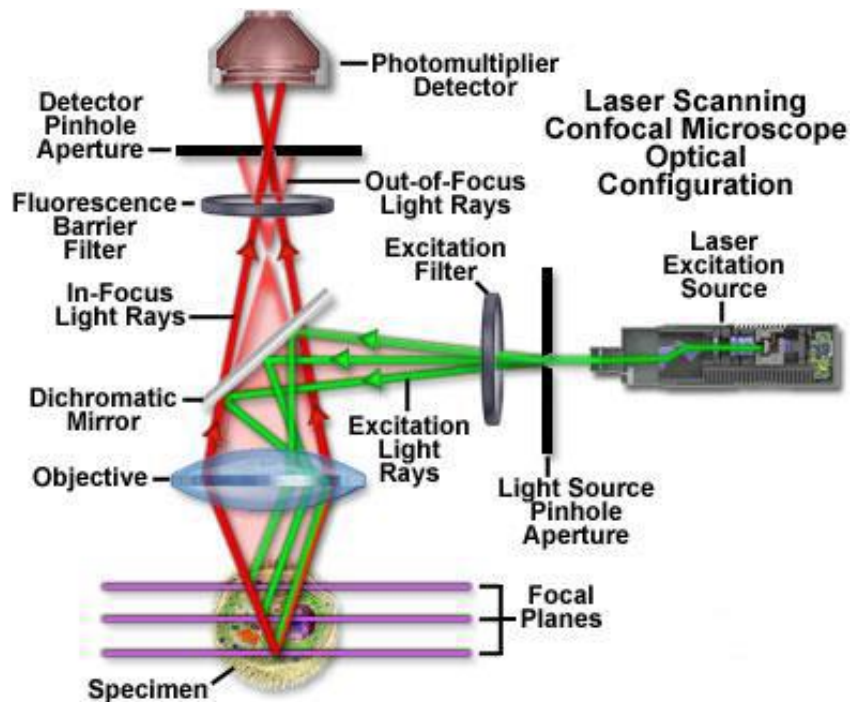


Figure 3.2.2 General Confocal-PL beam path.

Using equations (3.2.1-2) and known bandgaps we can determine what are the appropriate excitation lasers for MAPbI<sub>3</sub> and PbI<sub>2</sub>. The bandgap of MAPbI<sub>3</sub> is ~1.55eV which tells us that the photoluminescent wavelength will be ~800nm and will require an excitation laser with a shorter wavelength. Here we selected the 633nm excitation laser and a filter that allows for the collection of all light with a wavelength greater than

710nm. With a bandgap of ~2.3eV for PbI<sub>2</sub> we know that the wavelength of the emitted light will be ~540nm and it will require a light of a lower wavelength to stimulate a response.<sup>43</sup> The PL response of both materials are shown in Figure 3.2.3. Here we use the 488nm excitation laser with the collection filter set to 505-605nm which insures that we are only collecting the photons from the PbI<sub>2</sub> and not from the perovskite which will also be experiencing a photoluminescent response from this laser. This will allow us to accurately differentiate between the two materials as far as the confocal microscope's resolution will allow. The resolution is the smallest discernable distance between two points and is measured both laterally and axially. The lateral resolution (R<sub>L</sub>) is the radius of the first Airy disc and is given by,

$$R_L = \frac{0.61\lambda_{ex}}{NA} \quad (3.2.3)$$

Where  $\lambda_{ex}$  is the wavelength of the excitation laser in air and NA is ne numerical aperture of the lens used. The axial resolution is given by

$$R_{ax} = \frac{1.4n\lambda_{ex}}{NA^2} \quad (3.2.4)$$

Where n is the index of refraction of the medium.

With NA being 1.4 the resultant R<sub>L</sub> for the 488nm and the 635nm excitation is 213nm and 277nm respectively.

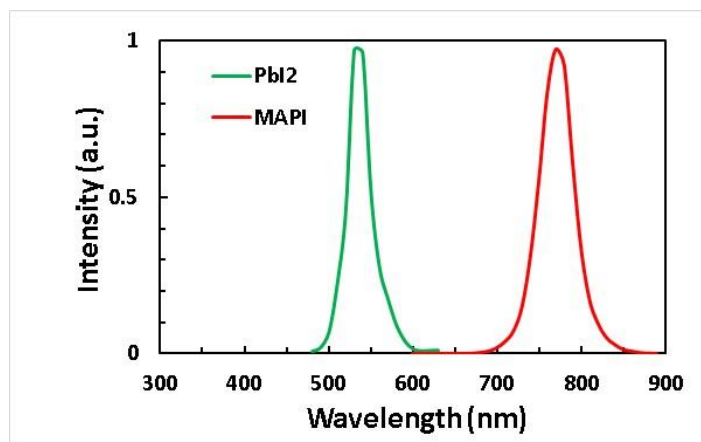


Figure 3.2.3 PL measurements of  $PbI_2$  and  $MAPbI_3$

It has been reported for Raman spectroscopy (633 nm) that using a laser power density of  $1300W/cm^2$  leads to film degradation within several seconds but using a power density of  $260W/cm^2$  the material is completely stable with zero signs of degradation for an hour.<sup>44</sup> With a laser power density of  $6.4W/cm^2$  this method is well within the bounds for non-destructive characterization.<sup>45</sup>

## Film Sets

This experiment was carried out with three different sample sets. The first was used primarily for equipment familiarization and for observing image quality of the grain boundaries. The second set consisted of bare perovskite and where used to gather axial intensity measurements. Lastly, were samples that consisted of 50nm  $PbI_2$  deposited via thermal evaporator on top of a perovskite layer. The purpose of this set was to determine

if the FlouView FV1000 would be able to indicate, and detect, where the  $\text{PbI}_2$  is in relation to the perovskite and the substrate.

The procedure for forming the perovskite films went as such. First, we prepared the inks and the substrates. The substrates that we used were 1x1 inch glass slide with a 125nm ITO coating, a common ETL. They were cleaned in a sonicator for 20 minutes while immersed in a Deconex OP 121 (5 wt.% in DI water) solution and then exposed to an  $\text{O}_2$  plasma (Harrick Plasma, Pdc-32G, RF power 18W) for 10 minutes before being transferred into a Nitrogen Glovebox for deposition. There were two inks prepared, a one molar solution of  $\text{PbI}_2$  in DMF (that is 461mg of  $\text{PbI}_2$  per 1 mL of DMF), and a solution of MAI in IPA that consisted of 70mg of MIA per mL of IPA. The  $\text{PbI}_2$  solution was placed on a hot plate set to  $75^\circ\text{C}$  until the  $\text{PbI}_2$  was fully dissolved. After the  $\text{PbI}_2$  is fully dissolved I used a pipet to deposit 100uL of the solution onto the clean substrate and, using a spin-coater, evenly distributed the solution over the substrate by spinning it as 4000rpm for 60 seconds. The substrates were then placed on a hot plate set to  $100^\circ\text{C}$  for 10 minutes to allow the  $\text{PbI}_2$  film to anneal. This results in a yellow film covering the clear ITO/glass substrate. After the substrate was allowed time to cool down I placed it back in the spin-coater and deposited 100uL of the MAI/IPA solution and spincoated the sample at 3000rpm for 60 seconds. At this point the once yellow film now appears to have a dark-brown or black color with a matte finish. Lastly, I annealed the sample again for 10 minutes at  $100^\circ\text{C}$  were it forms a fully converted black perovskite film with a somewhat reflective gloss.  $\text{PbI}_2$  was deposited on the surface of several perovskite samples and a glass witness slide by means of thermal vapor deposition using a Trovato 300C vacuum thermal evaporator with a deposition rate of 0.1 nm/sec and base

pressure  $5 \cdot 10^{-7}$  Torr. Using a Burkert Profilometer the film thicknesses of the perovskite and the  $\text{PbI}_2$  were measured to be 440nm and 50nm respectively.

The procedure for using the FluoView FV1000 Confocal microscope goes as follows. After turning on the system and software we first use a 10x objective to find our initial focus. Next, we add a drop of the silicon oil on the sample and switch to the 60x, 1.4 NA, objective. The purpose of the oil is to lessen the effect spherical aberration caused by mismatched refractive indices of the immersion medium and the sample, as seen in Figure 3.2.4. Here the oil has a refractive index of 1.5 and the perovskite has a refractive index of 2.4.<sup>46,47</sup> Although this is better than using a non-emersion objective there will still be some spreading of the depth of focus due to the light from the objective transitioning from a medium with a lower index of refraction than sample, reducing the depth resolution, which is described by the following,

$$DR = \Delta \left[ \left( \frac{NA^2(n^2-1)}{1-NA^2} + n^2 \right)^{\frac{1}{2}} - n \right] \quad (3.2.5)$$

Where NA is the numerical aperture, n is given by  $n=n_1/n_2$ , which is the ratio between the refractive indices of the medium between the film and the aperture and the film its self, and  $\Delta$  is the focus depth into the film.<sup>48</sup>

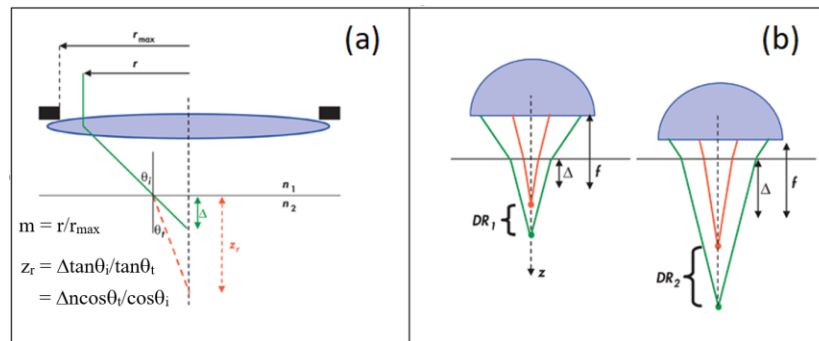


**Figure 3.2.4. Ray tracing the Depth Resolution.** We see the way in which the resolution is distorted due to mismatched index of refraction at the films interface.<sup>49</sup>

This lowering of the resolution caused by the mismatching of refractive indices the resolution will linearly worsen the further we focus into the film (see Figure 3.2.5).

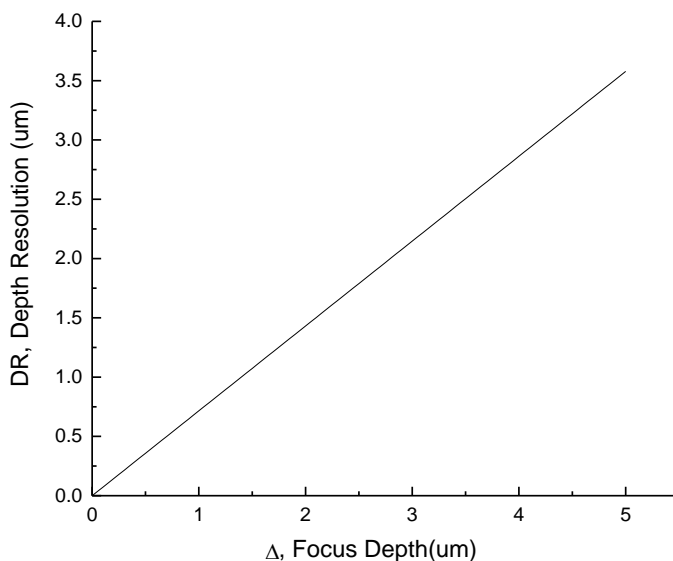


*Figure 3.2.5. Depth Resolution vs Focus Depth. Here we see the change in resolution as with respect to the focus depth as described by equation (3.2.5).*

After refocusing with the 60x objective I then select the setting to the two channels in the software. Channel 1 was set to detect  $\text{PbI}_2$  by using a 488nm laser and a 505-605nm collection filter. Channel 2 used a 633nm excitation laser and the 710LP filter to collect PL from the  $\text{MAPbI}_3$ . We then tuned the laser intensities to reduce the signal noise.

## Signal Reflection

For both sample sets 1 and 2 we set the axial scan to move in 100nm increments with the bounds of the scan set to where signal intensity is negligibly low. While reviewing the axial intensity data it was noticed that there was a peculiar double peak and shoulder hump. It was later determined that this was a result of signal reflection as seen. In Figure 3.2.6 we compare an axial intensity graph to that of a graph with the same effect studied by Sheppard *et al.* Using the following equations, I was able to create a Matlab GUI to model the effect.

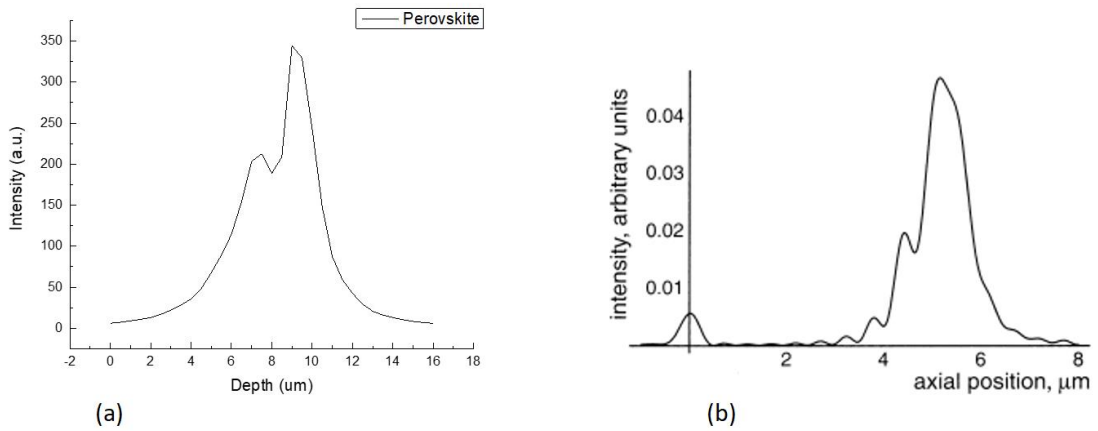


**Figure 3.2.6 Side Peak due to reflection.** (a) Intensity vs depth for perovskite film. (b) Graph from the Sheppard *et al.* in their paper on axial reflectivity.<sup>50</sup>

The reflections influence in the intensity measurements for depth profiling can be calculated by the following

$$I(z) = \left| \int_0^\alpha r(\theta) \exp(2ikn_0z \cos(\theta)) \sin(\theta) \cos(\theta) d\theta \right|^2 \quad (3.2.6)$$

Where

$$r(\theta) = \frac{r_\sigma - r_\pi}{2} \quad (3.2.7)$$

And for single films on a substrate  $r_\sigma$  and  $r_\pi$  are,

$$r_\sigma^{(3)} = \frac{r_{01,\sigma} + r_{1s,\sigma} \exp(2i\beta)}{1 + r_{01,\sigma} r_{1s,\sigma} \exp(2i\beta)} \quad (3.2.8)$$

$$r_\pi^{(3)} = \frac{r_{01,\pi} + r_{1s,\pi} \exp(2i\beta)}{1 + r_{01,\pi} r_{1s,\pi} \exp(2i\beta)}$$

For two films stacked on top of a substrate they are

$$r_\sigma^{(4)} = \frac{r_{01,\sigma} + r_{12,\sigma} \exp(2i\beta_1) + (r_{01,\sigma} r_{12,\sigma} + \exp(2i\beta_1)) r_{2s,\sigma} \exp(2i\beta_2)}{1 + r_{01,\sigma} r_{1s,\sigma} \exp(2i\beta_1) + (r_{12,\sigma} + r_{01,\sigma} \exp(2i\beta_1)) r_{2s,\sigma} \exp(2i\beta_2)} \quad (3.2.9)$$

$$r_\pi^{(4)} = \frac{r_{01,\pi} + r_{12,\pi} \exp(2i\beta_1) + (r_{01,\pi} r_{12,\pi} + \exp(2i\beta_1)) r_{2s,\pi} \exp(2i\beta_2)}{1 + r_{01,\pi} r_{1s,\pi} \exp(2i\beta_1) + (r_{12,\pi} + r_{01,\pi} \exp(2i\beta_1)) r_{2s,\pi} \exp(2i\beta_2)}$$

Where

$$r_{01,\sigma} = \frac{n_0 \cos(\theta_0) - n_1 \cos(\theta_1)}{n_0 \cos(\theta_0) + n_1 \cos(\theta_1)} \quad (3.2.10)$$

$$r_{01,\pi} = \frac{n_1 \cos(\theta_0) - n_0 \cos(\theta_1)}{n_1 \cos(\theta_0) + n_0 \cos(\theta_1)}$$

And the phase factor  $\beta$  is given by

$$\beta_i = \frac{2\pi d_i n_i}{\lambda} \quad (3.2.11)$$

Where  $d_i$  and  $n_i$  is the thickness and refractive index of the layer.

## Results

The set used for equipment familiarization and imaging provided me with highly detailed images. In Figure 3.2.7 we can see the perovskite film with the red color corresponding to the perovskite PL and the green corresponds with to the  $\text{PbI}_2$  PL. The sample used here was created through the “Hot-Casting” method in which after the  $\text{PbI}_2$  film is annealed the sample is immediately transferred to the spin-coater where the MAI solution is immediately deposited. This is done as quickly as possible and results in films with large crystal formation. Additionally, this film was formed on a ZnO coated substrate that is known to promote  $\text{MAPbI}_3$  film degradation. The top image is focused on the ZnO interface and we see significantly more green indicating that the presence of  $\text{PbI}_2$  which leads us to determine that degradation has occurred at that interface due to the thermal shock undergone during Hot-Casting”. Additionally, this degradation continued up the film along the grain boundaries as we can see in the bottom image by the green boarders of the formed crystals, indicating the presence of excess  $\text{PbI}_2$ .

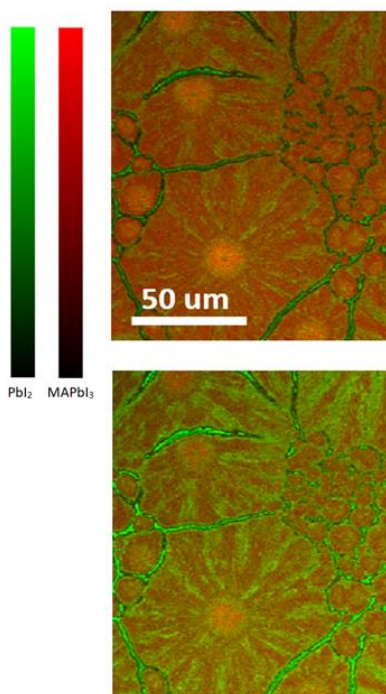


**Figure 3.2.7 Surface Image of Perovskite Film.** The green represents PL with 505-605nm wavelength and the red represents a PL with 710-1000nm wavelength, relating to  $\text{PbI}_2$  and  $\text{MAPbI}_3$  respectively. The image above is focused on the surface of the perovskite and the image below is focused on the ZnO interface layer.

It was necessary to determine what is an adequate step size of the microscope stage while executing the depth scans. The FlouView FV1000 is capable of moving the stage in 10nm increments. In Figure 3.2.8 we see the result of two tests, where one is uses a 50nm step size and the other uses a 500nm step size. When comparing the two we see that there are no major features that are missing from the graph of with the larger step size. This lead me to determine that, because of the low resolution calculated earlier due to spherical aberration, further characterization with the 500nm step size is adequate for my purposes.

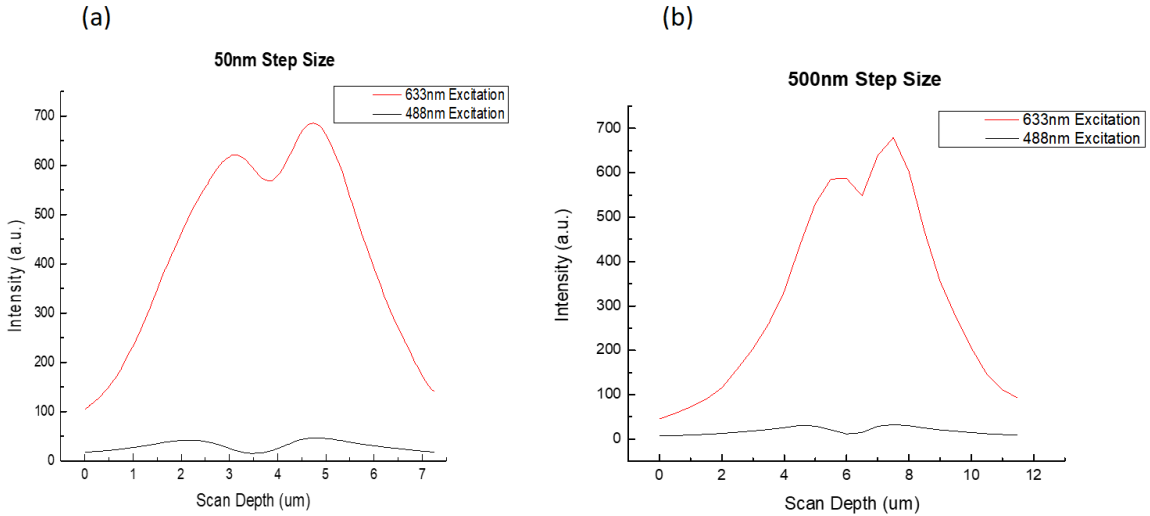
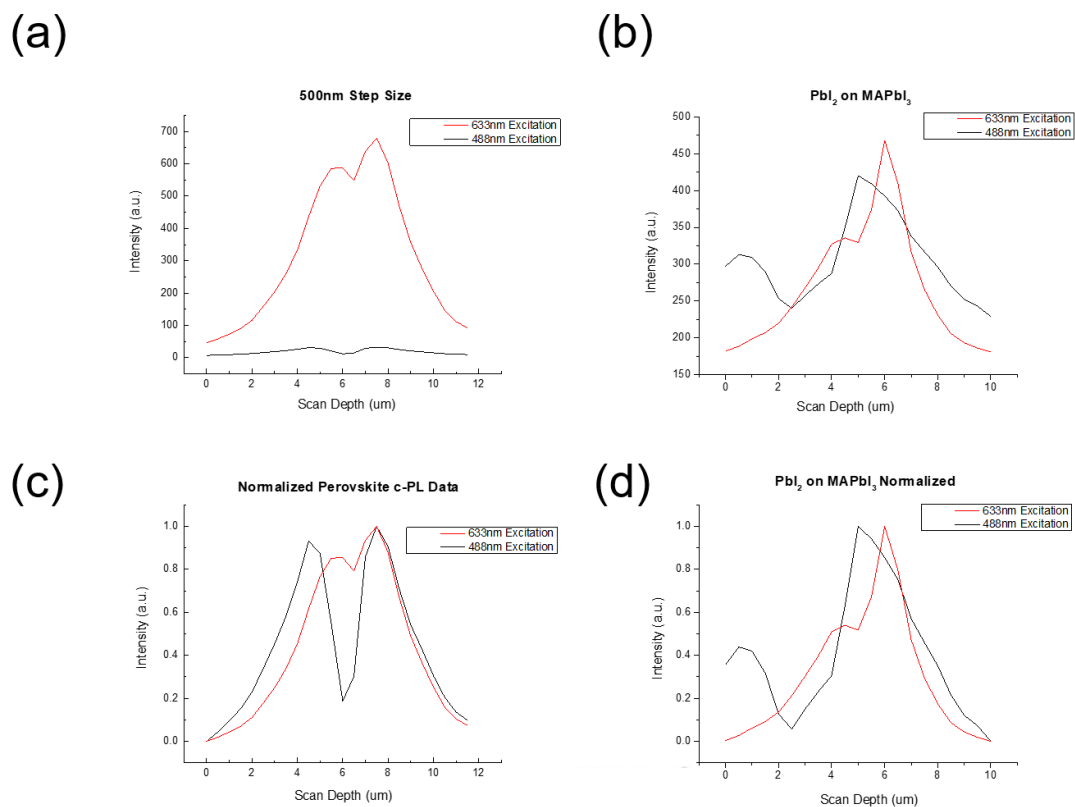
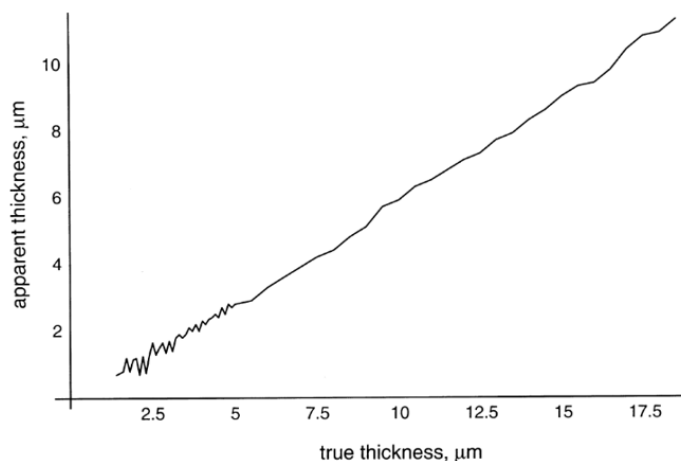


Figure 3.2.8 Comparing axial intensity of scans with (a) 50nm and (b) 500nm step sizes.

Next, I tested the methods ability to detect  $\text{PbI}_2$  located on the surface of the film despite the low optical resolution. In Figure 3.2.9 we see can clearly see that there is an increase in the intensity from the 488nm excitation as well as a shift in what we can see to be a primary peak. These differences are even more apparent when the data from both the  $\text{PbI}_2$  covered and the bare  $\text{MAPbI}_3$  film. Unfortunately, neither the full width half max (FWHM) nor the half width half max (HWHM) of either the higher peak or the apparent shoulder peak corresponds to the actual film thickness. The inability for the Confocal microscopy to adequately resolve the thickness of very thin films was demonstrated by Cox *et al.* and is shown in Figure 3.2.10.



**Figure 3.2.9** Comparing bare MAPbI<sub>3</sub> samples to samples with PbI<sub>2</sub> deposited on perovskite. (a) is the axial scan of bare MAPbI<sub>3</sub> and (b) is the axial scan of PbI<sub>2</sub> on MAPbI<sub>3</sub>. (c) and (d) are the same scans normalized. This allows us to see the way in which the PbI<sub>2</sub> peak shifts in relation to the MAPbI<sub>3</sub> peak.



**Figure 3.2.10.** The calculated dependence between real and apparent thickness from Cox et al. Unfortunately it is not possible to accurately determine film thickness for samples  $< 5 \mu\text{m}$ .<sup>51</sup>

A round of test was conducted with a set of films that I produced while looking to determine an adequate concentration of MAI to IPA for the two-step method. For this film test I produced inks that were 10, 20, 30, 40, 50, 60, and 70mg/mL MAI/IPA and preformed XRD measurements, as seen in Figure 3.2.11, to confirm if the film had partially or fully converted to MAPbI<sub>3</sub>. The XRD measurements were performed with Bragg-Brentano focusing, Theta/2Theta scan mode, and a K-Beta filter method. I then preformed c-PL depth measurements to determine where the film conversion takes place. In Figure 3.2.12 we see that instead of the perovskite forming at any one of the interfaces it appears to form evenly throughout the film. This is indicated by the 488nm excitation peak not changing position relative to the 635nm excitation peak as it did with the PbI<sub>2</sub> coated samples seen in Figure 3.2.9.<sup>52,53</sup>

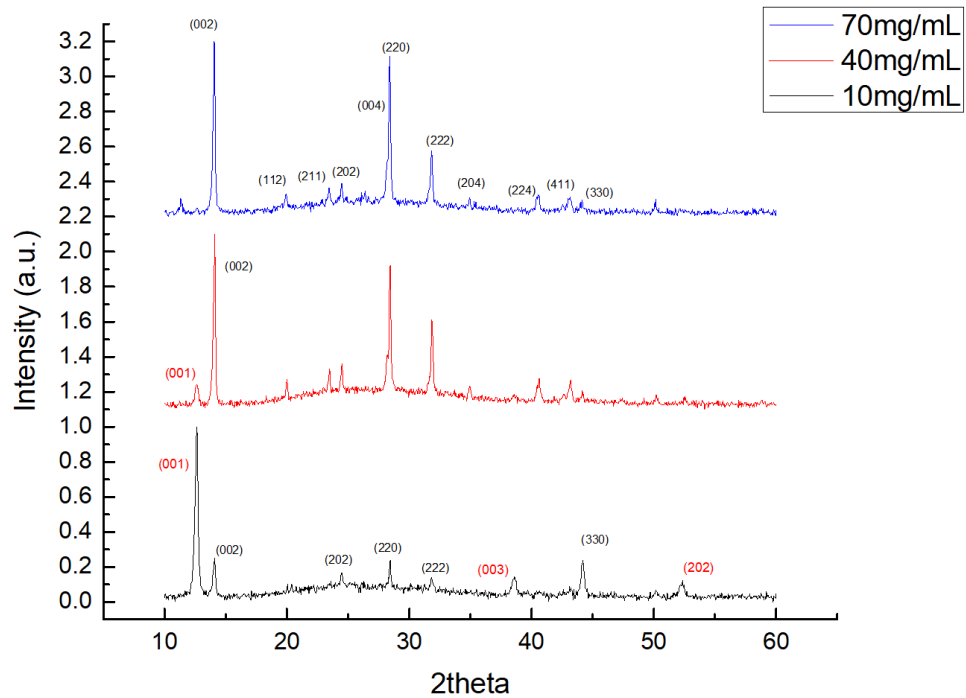


**Figure 3.2.11 XRD analysis of film produced with varying MAI/IPA solution concentrations.** The red indices indicate PbI<sub>2</sub> and the black indices indicate MAPbI<sub>3</sub>. We see that at the top the 70 mg/mL MAI/IPA is fully converted whereas the bottom two are only partially converted.<sup>52,53</sup> Note: the dominant (220) and (002) indices indicate tetragonal crystal growth along the direction of the substrate.<sup>54</sup>

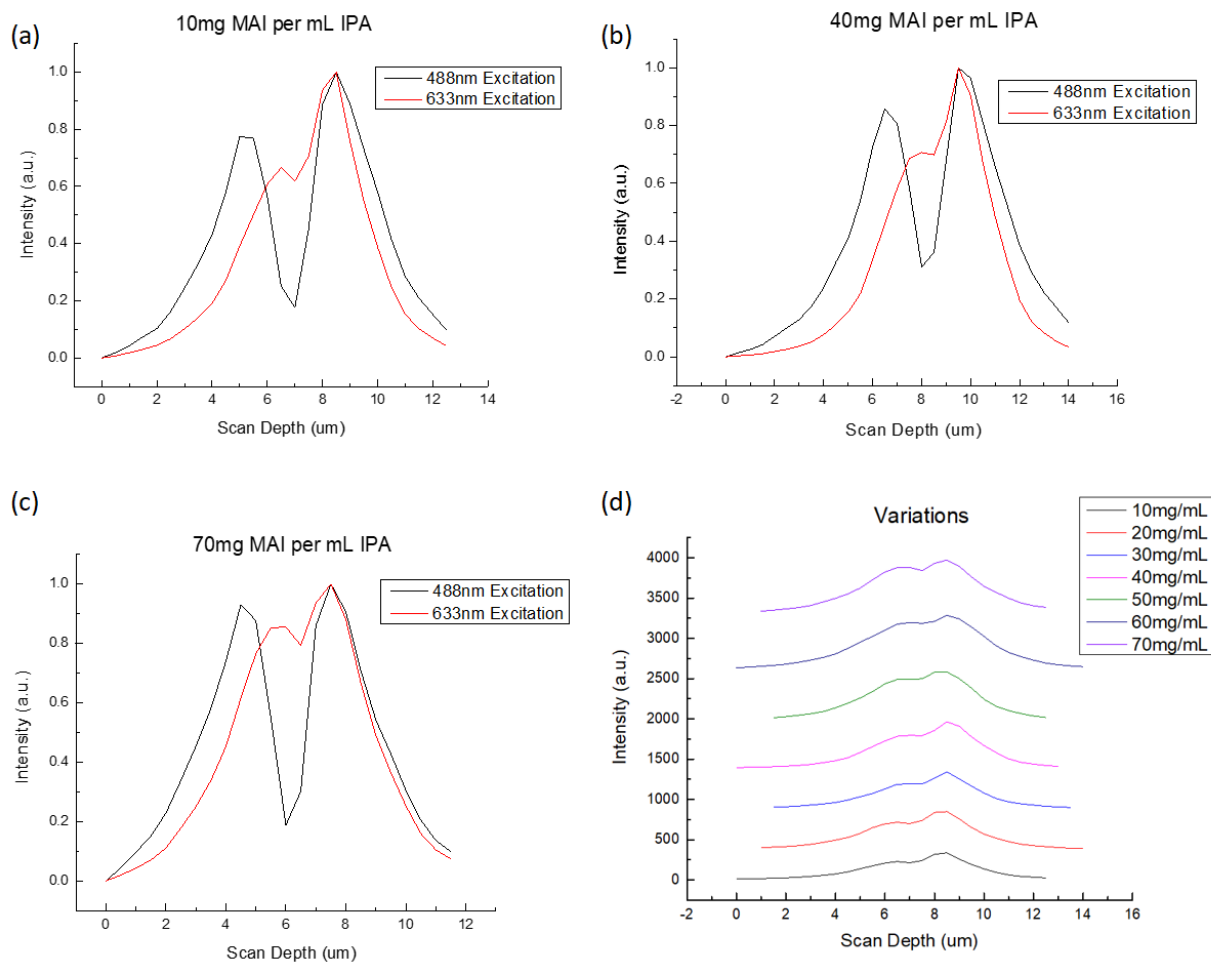


**Figure 3.2.12. c-PL depth measurement of films formed with varying concentrations of MAI to IPA. In a-c we see no lateral shift in the 488nm excitation peak. In (d) we see 488nm excitation data for all the 7 different ink concentrations.**

## **Raman Spectroscopy**

Raman Spectroscopy is a characterization technique that takes advantage of the unique signature of the inelastically scattered light that is emitted from a material when it is irradiated with light. This inelastic scattering of light was first predicted in 1923 by Adolf Smekal and later experimentally verified in 1928 by C.V. Raman for whom Raman Scattering and the Raman effect is named.

When light is scattered it can be classified as elastic or inelastic. Elastic scattering, also known as Rayleigh scattering, is where there is no net transfer of energy between the molecule and the photon. This means that the light that is scattered has the same wavelength and energy as the incident light.

The inelastic scattering occurs when the reflected light has more or less energy than the incident light due to energy transfer to or from a vibrational state of the molecular structure of the molecule being interrogated. Raman Scattering comes in two forms, Stokes scattering where the light has less energy than the incident light, and anti-Stokes scattering, where the scattered light has more energy than the incident light. Raman Scattering is the product of molecular vibrations that causes a change in polarizability, altering the size, shape, or orientation of the electron cloud that surrounds the molecules. This change occurs in symmetric stretching but not in asymmetric stretching. This means that intense Raman scattering occurs from symmetric vibrations that induce large distortions of the electron cloud around the molecule.

The types of light scattering are depicted in Figure 3.3.1. Stokes scattering occurs when an electron is excited from the ground level but fall to a vibrational level resulting in scattered light that has less energy (longer wavelength) than the incident light. Anti-Stokes scattering occurs when the electron is excited from the vibrational state and relaxes down to the ground state resulting in light with higher energy (shorter wavelength) than the incident light.

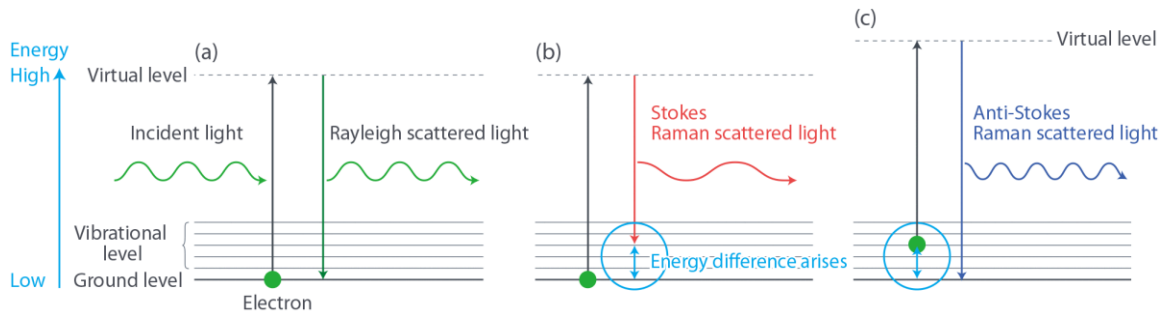


**Figure 3.3.1 types of light scattering.** The vast majority of scattered light is (a) Rayleigh scattered. Raman Spectroscopy measures (b) Stokes and (c) anti-Stokes scattering to evaluate and characterize materials.

The Raman scattered light only accounts for a miniscule  $10^{-6}$  percent of all scattered light, the rest belonging to Rayleigh scattering. This light is filtered out so that only the Stokes and anti-Stokes scattered light is measured. The x-axis is measured in wavenumbers as opposed to absolute wavelength in order to normalize the spectra so that it is independent from the excitation wavelength.

$$\Delta\omega(\text{cm}^{-1}) = \left( \frac{1}{\lambda_0(\text{nm})} - \frac{1}{\lambda_1(\text{nm})} \right) \times \frac{(10^7 \text{ nm})}{(\text{cm})} \quad (3.3.1)$$

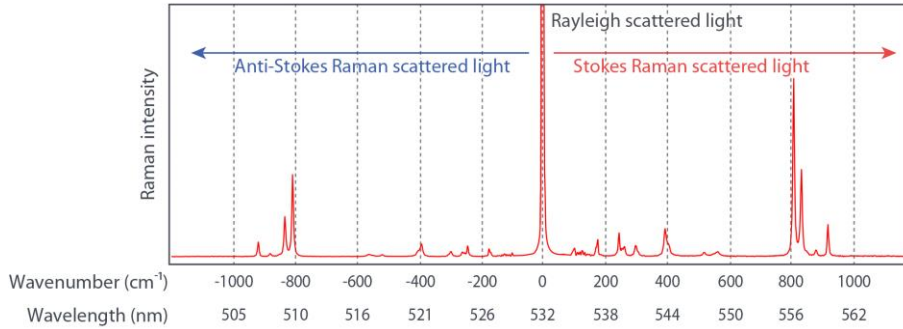


**Figure 3.3.2 Raman readout of scattered light.** Using equation (3.3.1) Raman Spec. outputs the signal as an inverse centimeter “Wavenumber”.

Each of the Raman Spectrum peaks are the result of specific Molecular or lattice vibrations. The position of the peaks indicates specific vibrational modes of each molecular functional group in the material and provides us with a “molecular fingerprint”. The shape and width of the peak contains information about the materials crystallinity as well (as seen in Figure 3.3.3). A crystalline material yields a spectrum with very sharp Raman peaks and an amorphous material tends to have broader and less intense Raman peaks. Any residual stress can be evaluated from the direction and amount of any shift on the Raman Peak. This is much more of a precise method when it comes to determining what the material in question is, as opposed to confocal photoluminesces (c-PL) that is solely dependent on a materials band gap, which is far from unique. With this technique, when we collect the signature for  $\text{PbI}_2$  one can be certain that the material is in fact  $\text{PbI}_2$ , and likewise with  $\text{MAPbI}_3$ .

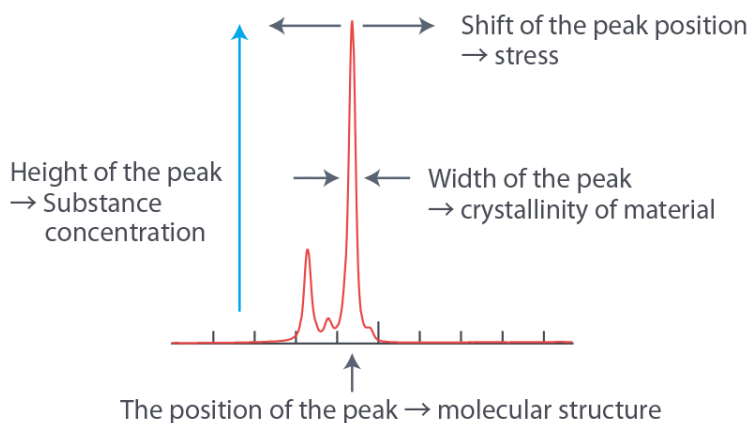


*Figure 3.3.3 Peak shape as it relates to material characterization.*

### **Confocal Raman Spectroscopy**

Using the technique of confocal microscopy we can then achieve more precise spatial resolution (than with standard Raman Spectroscopy) and create maps of samples that highlight the specific molecular compounds that they are composed of. In addition to the pin-hole used in confocal microscopy to filter out the out of focus contributions there is also a notch filter along the optical path, as seen in Figure 3.3.4, that is used to filter out the Rayleigh scattered light. There are however several issues that one must be aware of while attempting thin-film characterization with confocal Raman. Primarily the same resolution issues covered in the c-PL section that results from mismatched refraction indices of the perovskite and the medium between the sample and the aperture, which in this case is air.

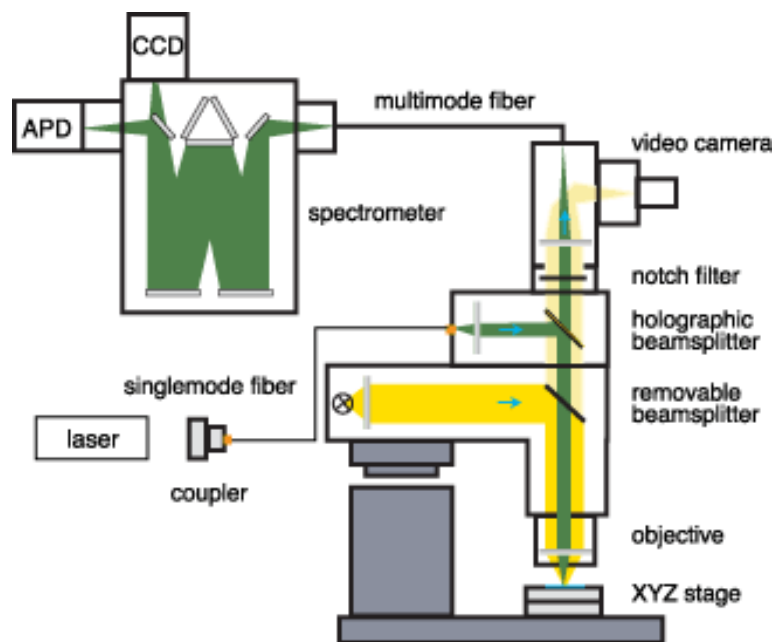


Figure 3.3.4 General beam path of a confocal Raman system.

### Raman Signature of MAPbI<sub>3</sub> and PbI<sub>2</sub>

From the literature we can already see a clear description of the MAPbI<sub>3</sub> and PbI<sub>2</sub> Raman signature and the vibrational modes associated with the recorded peaks. When looking at mixed compounds such as MAPbI<sub>3</sub> the Raman signature can be described as a combination of independent intensities that are functions of wavenumber ( $\omega$ ).<sup>55</sup>

$$I_t(\omega) = I_{bg}(\omega) + \sum_i \alpha_i I_i(\omega)_i \quad (3.3.2)$$

Here we see the total signal,  $I_t(\omega)$ , is equal to the background intensity,  $I_{bg}(\omega)$ , plus the sum of all the independent signals,  $I_i$ , where  $\alpha_i$  is the weight factor for the individual contributions.

Applying this to MAPbI<sub>3</sub> we can then treat the Pb-I cage and the MA cation contributions as quasi-independent allowing us to breakdown the Raman signal into its individual contributions and understand the thin film's decomposition mechanics. The work available on the Raman spectra of thin MAPbI<sub>3</sub> films has identified two complex broad peaks, one at the lower region (50-150 cm<sup>-1</sup>) and another at higher wavenumber regions (175-450 cm<sup>-1</sup>). More specifically two broad bands are observed, one at 110 cm<sup>-1</sup> and another at 250 cm<sup>-1</sup>.<sup>56</sup> The band at the lower region has been identified through theoretical calculations as being the result of vibrational contribution from the Pb-I cage of the MAPbI<sub>3</sub> structure and is located near the modes of PbI<sub>2</sub> (96, 106, and 113cm<sup>-1</sup>).<sup>57</sup>

Additional theoretical work by Quarti *et al.* predicts that the librational modes of the MA cations are found near 138cm<sup>-1</sup> and two torsional modes are found at 250cm<sup>-1</sup> and 390cm<sup>-1</sup>.<sup>58</sup> The lower band has a more narrow FWHM than the band at the higher wavenumbers which is fitting since the Pb-I cage is a highly ordered structure its crystallinity would naturally result in a more narrow peak than the MA cation which has more degrees of torsional and rotational freedom. These additional degrees of freedom contribute to a greater dispersion of the vibrational frequencies and leads to the Raman signature for this component to have a broader FWHM. Figure 3.3.5 shows the Raman spectra of MAPbI<sub>3</sub> and Figure 3.3.6a we can see its spectra broken up into its constituent parts.

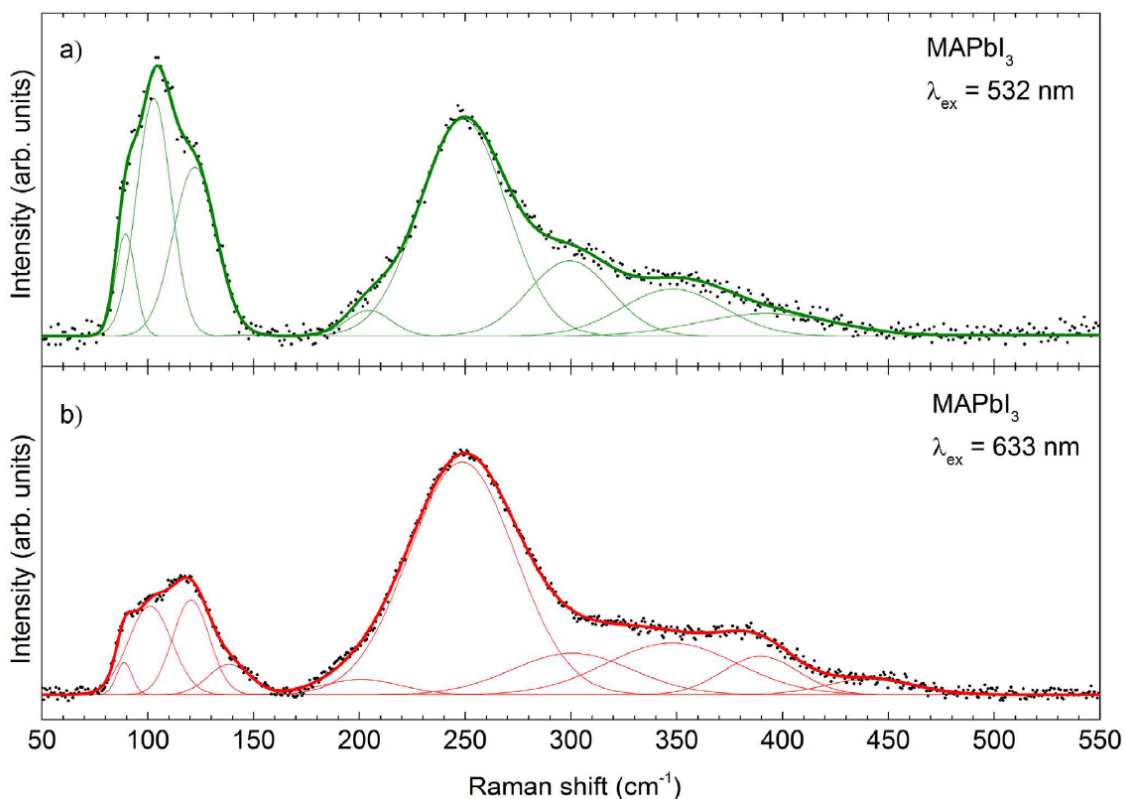
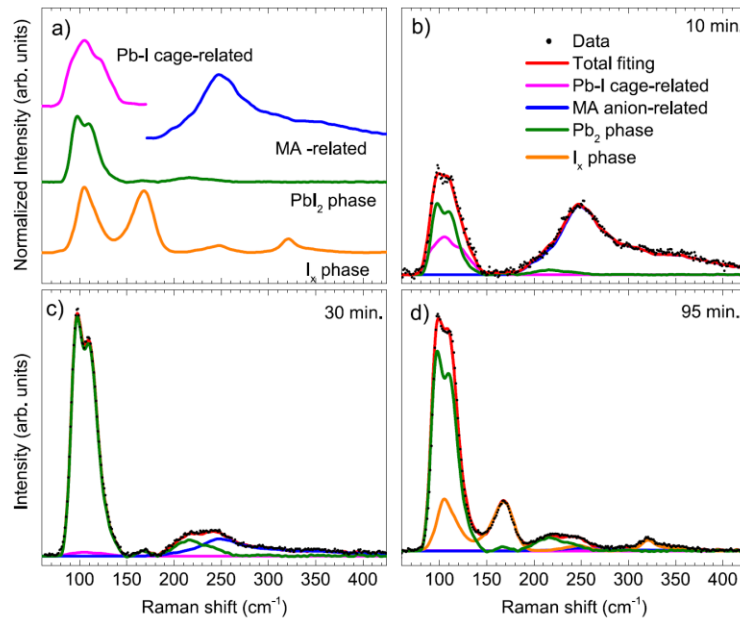


Figure 3.3.5 Raman spectra of MAPbI<sub>3</sub> thin films with (a) 532 nm and (b) 633 nm excitation laser.<sup>44</sup>

### Observed MAPbI<sub>3</sub> degradation

Using an iHR320 Horiba Jovin Yvon and Raman probe and macro-spot optics allowing for a 70 μm spot diameter Pistor *et al.* performed prolonged laser exposure measurements to 1) observe the way in which the Raman signature changes as it degrades and 2) to determine the acceptable laser power density for non-destructive Raman characterization. When the film is exposed to excessive laser power densities it naturally heats up and begins to decompose and different phases begin to co-exist with the MAPbI<sub>3</sub> such as PbI<sub>2</sub> and I<sub>x</sub>. Upon heating the intensity of the higher wavenumber contribution associated with MA torsional modes change with respect to the lower wavenumber

contribution associated mainly with the Pb-I cage and librational modes of the MA cation. In Figure 3.3.6a we see the independent contributions that are identified and taken in to account during the heating and degradation of the MAPbI<sub>3</sub> film. Two of these are the MA cation and the Pb-I cage contributions from MAPbI<sub>3</sub> and the other two coincide with PbI<sub>2</sub> and I<sub>x</sub> which is a third phase that forms during prolonged exposure to excessive laser excitation. As described by equation (3.3.2), Figure 3.3.6b-d shows both the Raman spectrum of MAPbI<sub>3</sub> measured during the degradation and how it can be expressed as a superposition of the different contributions. It was also found that the MAPbI<sub>3</sub> film maintains stability for laser power densities lower than 26W/cm<sup>2</sup>.<sup>44</sup>



**Figure 3.3.6 Breakdown of the MAPbI<sub>3</sub> Raman signature.** Deconstruction of mixed Raman spectra into individual contributions (a) Normalized reference Raman spectra from pure compounds used as individual contributions (b–d) Mixed Raman spectra and their decomposition into individual contributions obtained after different times of excessive laser exposure of a MAPbI<sub>3</sub> thin film.<sup>44</sup>

## Sample creation

There were several samples that I created for various Raman characterization tests. These tests include 1) measurements that recorded single spectra of a sample, 2) timed laser exposure tests, and 3) axial mapping characterization. There were spectra measurements of all the individual materials used, MAPbI<sub>3</sub>, PbI<sub>2</sub>, and SnO<sub>2</sub> which was used as an interfacial barrier layer. The timed exposure measurements were performed on bare MAPbI<sub>3</sub> while determining what system settings could be used for non-destructive characterization. Lastly, axial measurements were taken using samples that consisted of a set of bare MAPbI<sub>3</sub> samples with varying thicknesses and layered samples (MAPbI<sub>3</sub>/SnO<sub>2</sub>/PbI<sub>2</sub>), also with varying thicknesses for the MAPbI<sub>3</sub> layer. Additionally, the MAPbI<sub>3</sub> films for these samples were produced using the “One-Step” deposition method from the Spectral Ellipsometry section instead of the two-step deposition method employed in the c-PL section.

The first, and the most critical, part of this method is the “ink” preparation. This ink is made in three steps, the first two steps involve making a one molar PbI<sub>2</sub>/MAI/DMF solution. Here I would put 461mg of PbI<sub>2</sub> and 1 mL of DMF in a small, clear, glass vial with a magnetic stirring bar and then place it on a hotplate set to 70°C. After about 10 minutes the PbI<sub>2</sub> would completely dissolve. At this point I would then take the vial and insert 159mg of MAI and return the vial to the hotplate for an additional 10 minutes. Even after the MAI is fully dissolved the solution still has a somewhat cloudy appearance. In a second vial I would then place 91mg of MAAC, the purpose of which is to slow the rate of film formation and crystal growth, allowing for larger crystals to form during annealing. The PbI<sub>2</sub>/MAI/DMF solution is placed in a syringe affixed with a 1 μm

particle filter through which it is transferred into the vile containing the MAAC. After ~15 minutes of occasional stirring the MAAC is completely dissolved and the ink is ready for deposition. Next, in the N<sub>2</sub> glovebox, I would deposit 85mL of the ink on 1x1 inch glass substrates coated with a 125nm of ITO. Prior to deposition these substrates were cleaned and prepared in the same manor found in the c-PL and SE sections.

The layered samples consisted of the following 240nm layer of PbI<sub>2</sub> on the ITO substrate, on to which 10nm of SnO<sub>2</sub> was deposited via Atom Layer Deposition (ALD) to act as an interfacial barrier between the PbI<sub>2</sub> and the MAPbI<sub>3</sub> that is deposited as the final top layer. Additionally, I used a witness slide during the ALD deposition of the SnO<sub>2</sub> so that I would have a sample to use for Raman characterization.

The system used for Raman characterization was the Horiba LabRAM HR Evolution. With much trial and error, I was able to determine the proper machine and software setting for achieving non-destructive characterization. These consisted of using a 532nm excitation laser with a power of 8.81mW out of the 100X aperture with the Nutral Density (ND) filter set to 0.01% reducing the intensity to  $8.81 \times 10^{-7} \text{W}$ . The spot size of the laser beam from the 100X aperture was ~5 $\mu\text{m}$  giving us a power density of  $4.49 \text{W}/\text{cm}^2$  which is well within the given threshold for non-destructive characterization power density of  $26 \text{W}/\text{cm}^2$  as found by Pistor *et al.*

The LabSpec6 software that is used for interfacing with the Horiba LabRAM HR Evolution allows the user to choose multiple different scan parameters, data processing and analysis, as well different measurement types. The adjustable scan parameters include: scan acquisition time, number of accumulations (multiple scans averaged together), and scan wavenumber range. Data processing allows for baseline correction,

filtering data spikes, denoising, and data/signal smoothing. The system allows the user to take several different types of measurements, such as a single-point measurement that simply captures the spectra from one point of the film chosen by the user. Additionally, the system is capable of “mapping” measurement. With these the user can collect measurements of the sample that within an x, y, and z range selected by the user to create a 2D or 3D map of the material as well as selecting the time range that you want to collect so that you can see how a material behaves over a specified time frame of laser exposure.

### **Various MAPbI<sub>3</sub> spectra issues**

During equipment familiarization there were occasional signal and instrumentation issues. First, there are Two ways to identify MAPbI<sub>3</sub> during testing 1) Proper Spectra features and, 2) MAPbI<sub>3</sub> induced “Step”. Second there is an issue with Edge Filter transmittance and mismatched spectra stitching when the raised step feature was present. The spectra stitching was more of an issue when using the 1800gr/mm diffraction grating as opposed to the 600gr/mm, however when the MAPbI<sub>3</sub> induced step was present the 1800gr/mm grating was preferable because the 600gr/mm grating would show no discernable signs of the material being present. Unfortunately, I was Unable to determine remedy for MAPbI<sub>3</sub> “Step” and the Horiba representatives were unable to deduce the cause of this feature. In this section I will compare the proper spectra to the step-feature. Next, I will show the difference in the spectra when using the 1800 and 600gr/mm grating when the step is present. Afterwards, I will show the results of degradation on the spectra with the step-feature, as well as the way in which the step-

feature shifts with the change in the starting position of the scan range. Moving on I will show the results of the timed exposure tests with different interfaces. Lastly, I will cover the findings from the axial profiling and characterization tests.

### **Proper MAPbI<sub>3</sub> Spectra**

When the Machine would collect the proper spectra, as seen in Figure 3.3.7, the features would appear the same for both the 600gr/mm and the 1800gr/mm. The excitation laser used was 532nm as opposed to the 633nm laser since it was less effected by the PL response. A neutral density (ND) filter of 0.01% was used to reduce the laser power to non-destructive levels as determined by Pistor *et al.* to be below 26W/cm<sup>2</sup>. With the laser output power of 8.81mW reduced by 0.01% and a spot size of ~5μm the power density was 4.49W/cm<sup>2</sup>, well below the reported threshold.

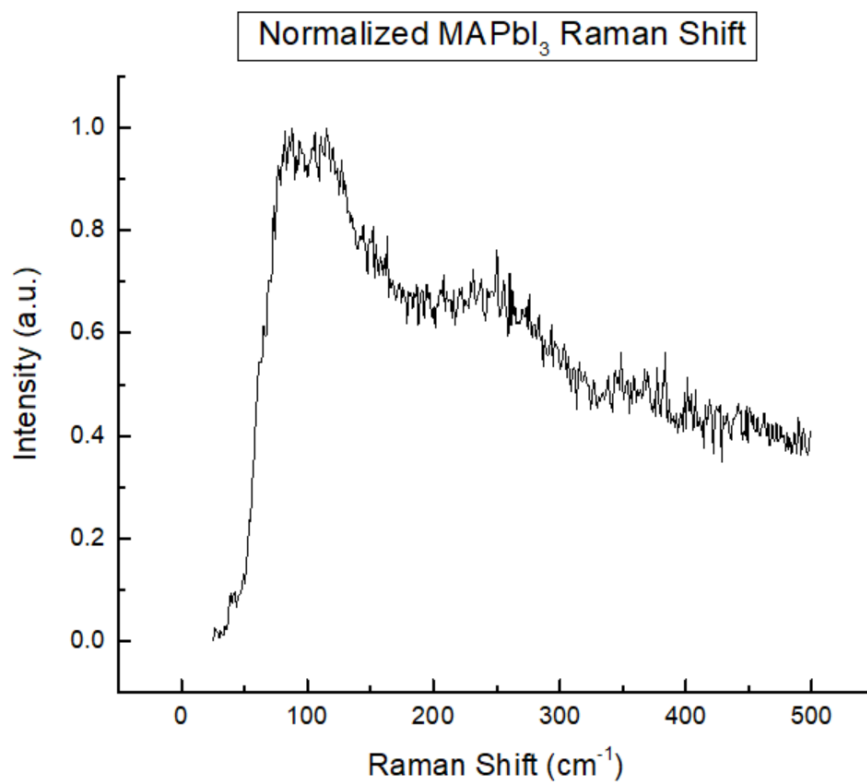


*Figure 3.3.7 Raman spectra of MAPbI<sub>3</sub> prior to baseline corrections.*

Using the LabPro6 software I was able to set the signal baseline similar to the work done by Pistor, as depicted in Figure 3.3.8, resulting in a Raman signature that matches the data that has been reported in the literature. To do this it was necessary to flatten the sharp rise in signal that started  $\sim 50\text{cm}^{-1}$  caused by the edgefilter transmittance and also the parabolic curve of the signal that results from the Rayleigh stray light.

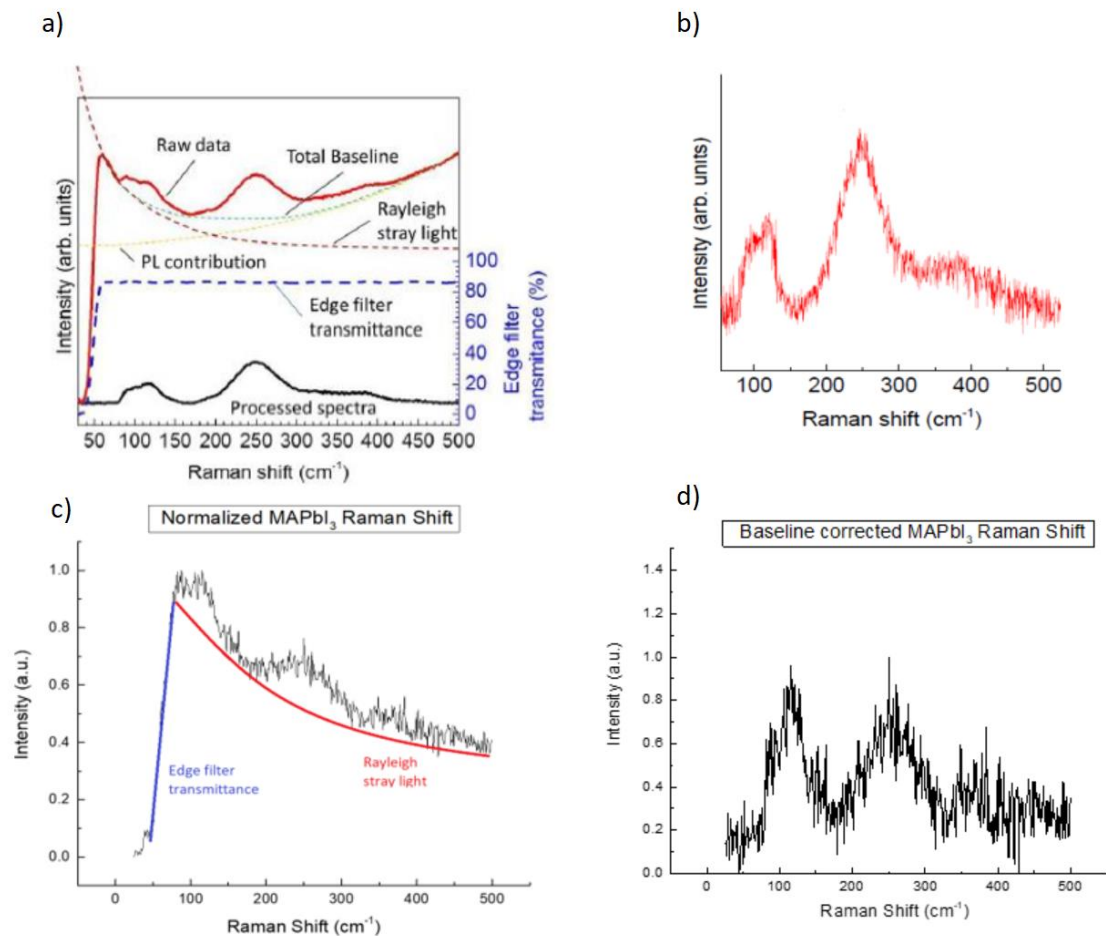


**Figure 3.3.8 Raman spectra and baseline correction.** Here we see data from Pistor et al. compared to my collected and corrected spectra. On top in a) and b) we see the MAPbI<sub>3</sub> spectra from Pistor and in c) and d) we see the spectra collected from the Horiba LabRAM HR Evolution Raman Spectrometer.<sup>44</sup>

### MAPbI<sub>3</sub> Induced Step

While interrogated other samples, both with the same system settings and created in the same manner as the previous samples that resulted in the data depicted in Figure 3.3.7, there was an odd feature that would present itself. This was a dramatic step that would rise sharply starting from  $\sim 175\text{cm}^{-1}$  from the starting range of the scan. This feature, seen in Figure 3.3.9, is only found when using the 1800gr/mm grating.

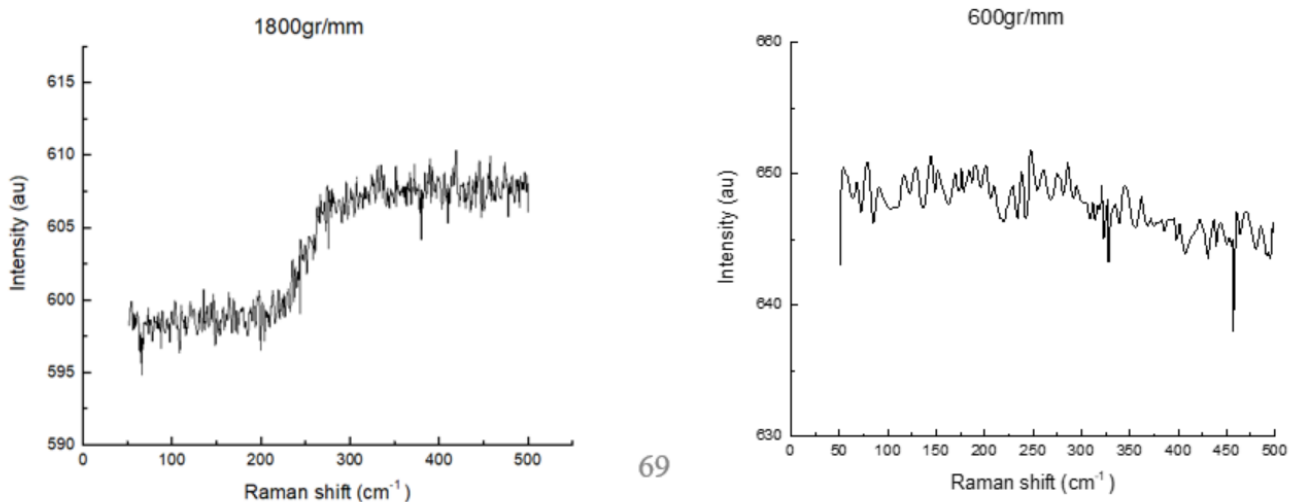


*Figure 3.3.9 Signal change depending on grating used. Here is comparison of signal while using the 1800gr/mm grating to 600gr/mm when step feature is present.*

When the scan range was increased it was found that the step was a repeating feature, presumably due to mismatched stitching of the segments during the scans with extended ranges. This was less of an issue with the 600gr/mm grating where the stitching occurs in  $\sim 1400\text{cm}^{-1}$  segments as opposed to the 1800gr/mm where the mismatched spectra stitching repeats in  $\sim 500\text{cm}^{-1}$  segments (as seen in Figure 3.3.10).

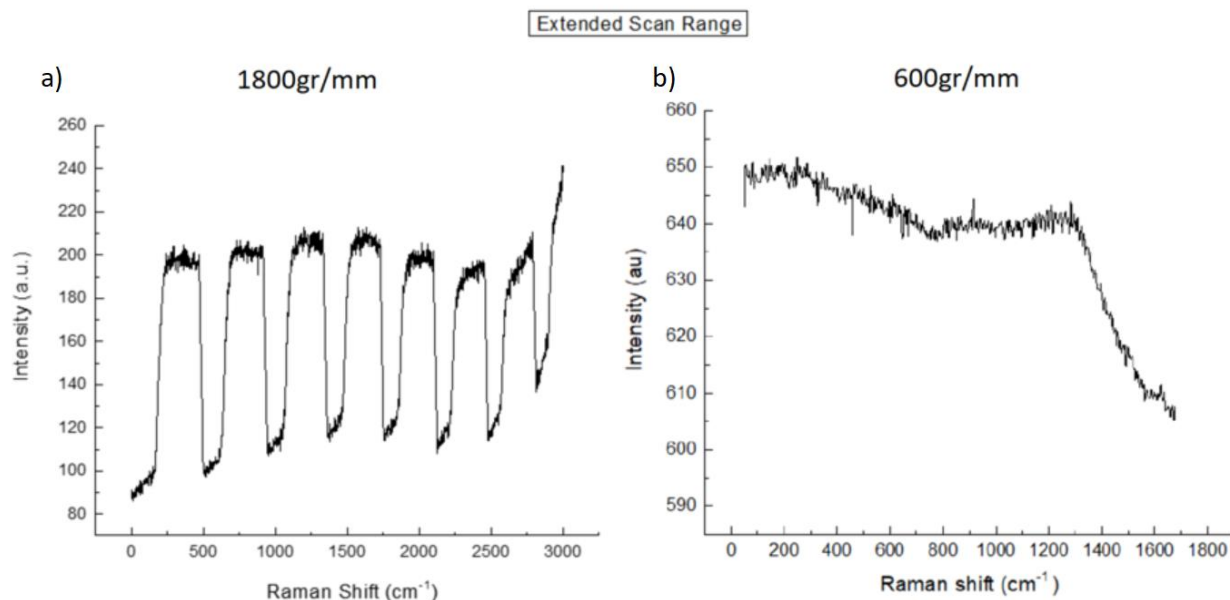


**Figure 3.3.10 Extended wavenumber range.** In a) we see that the step feature drops of sharply  $\sim 500\text{cm}^{-1}$  and then repeats. In b) we see that the 600gr/mm grating experiences a signal drop  $\sim 1300\text{cm}^{-1}$  which is far outside the range of the  $\text{MAPbI}_3$  signature.

Next, I decided to see how these features would change due to thermal degradation. Here I would expose the sample to the laser with the ND filter set to 0.1% for 5 seconds to induce degradation then rescan with the filter set back to 0.01% in effort to maintain consistency with my scan parameters. Looking at the sample through the 600gr/mm grating we see the gradual rise in intensity in the  $95\text{-}115\text{cm}^{-1}$  range corresponding with an increase in  $\text{PbI}_2$  as the  $\text{MAPbI}_3$  decomposes. The rise in the  $\text{PbI}_2$  peaks are also seen in the before and after scans taken with the 1800gr/mm grating. In Figure 3.3.11 we see the scans as taken with both diffraction gratings.

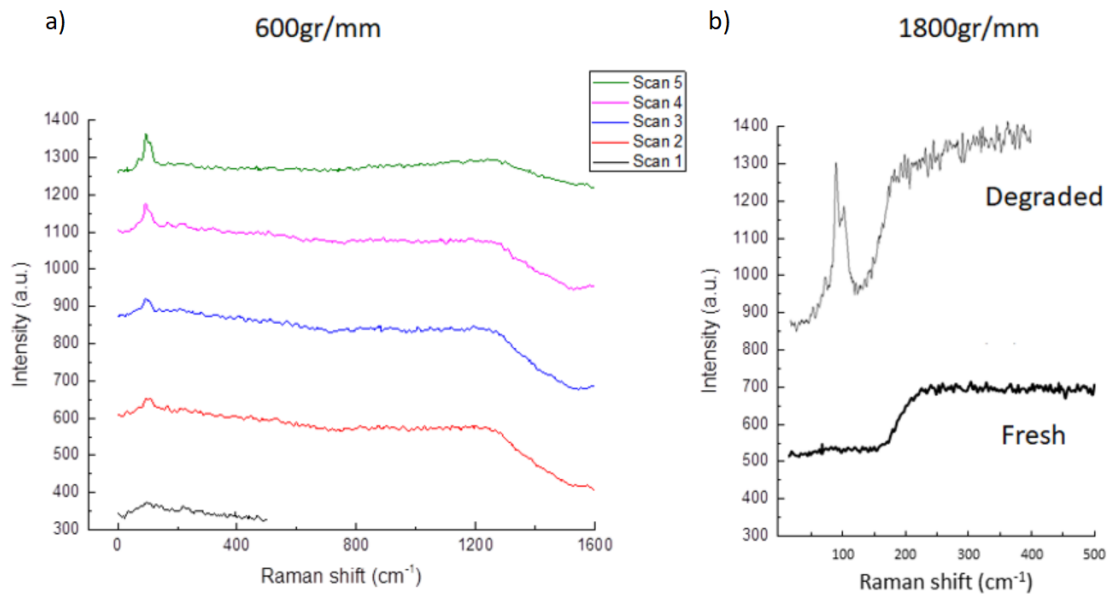


**Figure 3.3.11** Spectra change as MAPbI<sub>3</sub> film degrades. In a) we see the spectra change after each exposure to excess laser power. In b) we see the before and after spectra through the 1800gr/mm diffraction grating.

Furthermore, it was found that not only do the steps repeat, they also shift depending on the starting point of the wavenumber scan range. Looking at Figure 3.3.12 we can see that the step shift is present even in the partially degraded sample where the PbI<sub>2</sub> peaks are raised by the same intensity of the step, yet there is no step present in the scan of blank glass. Although we were unable to determine the exact cause of the step we were at least able to correctly collect the signature for PbI<sub>2</sub>. We then decided to move on and use the step as sign of MAPbI<sub>3</sub> being present.

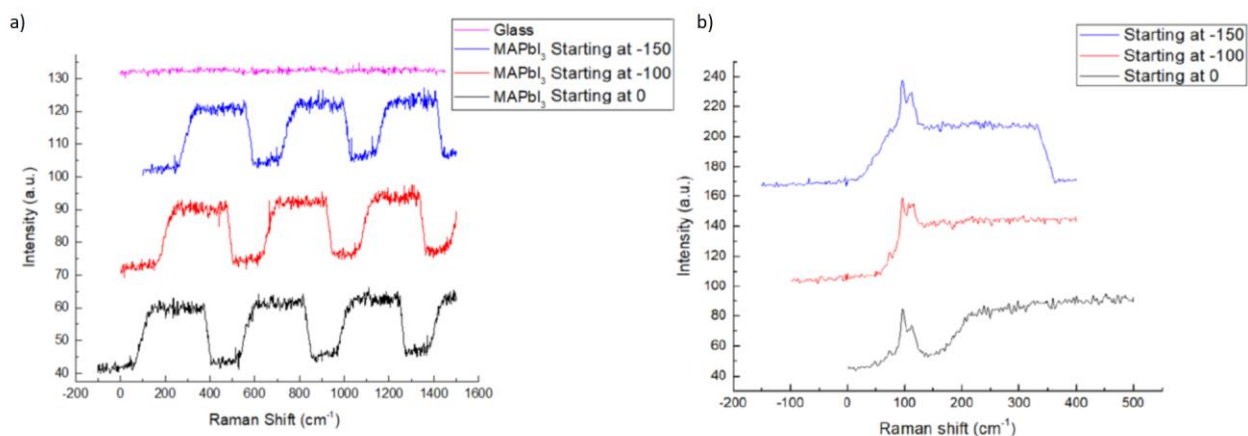


**Figure 3.3.12 Shifting MAPbI<sub>3</sub> induced step.** Here we see that the step shifts in both a) and b) depending on the starting position of the scan.

### Interfacial Thermal Degradation

As discussed earlier, Pistor *et al.* determined that MAPbI<sub>3</sub> is stable with a laser power density under 26W/cm<sup>2</sup> while using a 532nm excitation laser. With the Horiba LabRAM HR Evolution the approximate spot size for the 532nm laser with 100x magnification and 0.01% ND filter is ~5μm, giving an area of 1.962x10<sup>-7</sup>cm<sup>2</sup>. Intensity of 532nm exiting the 100x aperture (with ND filter at 100%) is 8.81mW. Intensity with 0.01% ND filter is 8.81x10<sup>-7</sup> W. This gives us a power density of 4.49W/cm<sup>2</sup> which is well within the given threshold for non-destructive characterization power density of 26W/cm<sup>2</sup>. It was found that the interface between the MAPbI<sub>3</sub> and the substrate has an effect on the sample stability while attempting to characterize a sample on bare glass.

I then performed timed scans on a sample of MAPbI<sub>3</sub> on glass and a sample of MAPbI<sub>3</sub>/ITO/Glass to show how their Raman signatures responded to prolonged laser exposure. In Figure 3.3.13 we see that the MAPbI<sub>3</sub> on ITO maintained its signature indicating the samples stability as opposed to the sample on glass that began to rapidly degrade after ~1 hour of laser exposure.

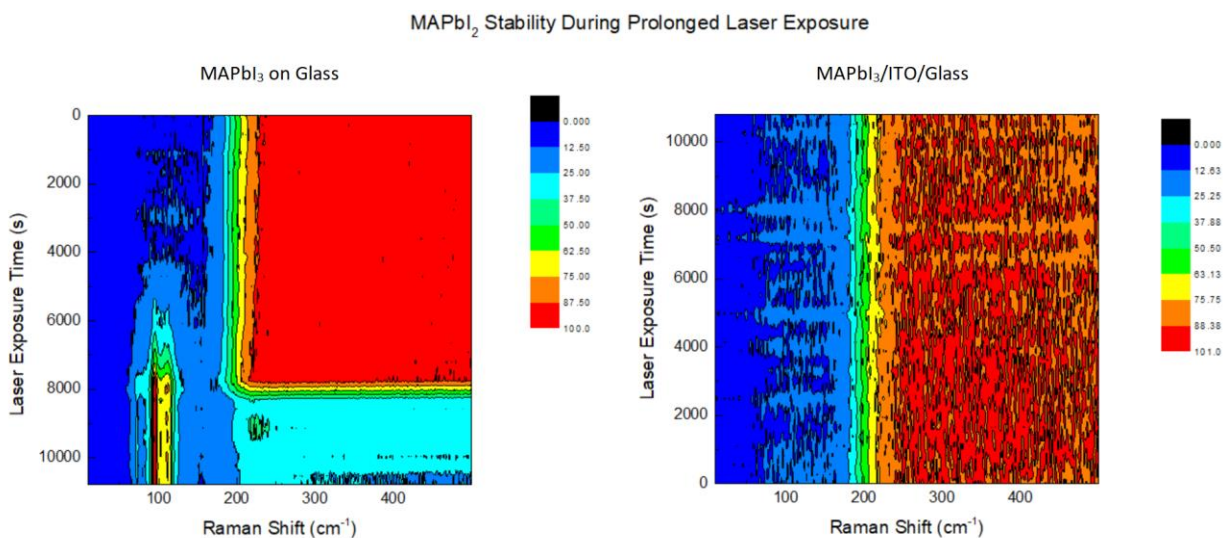


*Figure 3.3.13 The effects of interface on MAPbI<sub>3</sub> stability. To the left we see that the sample on glass degrades as opposed to the MAPbI<sub>3</sub> on ITO which maintains its stability on the right.*

In Figure 3.3.14 the change in average intensity of the 95-115cm<sup>-1</sup> wavenumber range, relating to PbI<sub>2</sub>, and the 250-300cm<sup>-1</sup> wavenumber range, associated with the MAPbI<sub>3</sub> induced step, are graphed with respect to time from the sample on glass that experienced degradation.

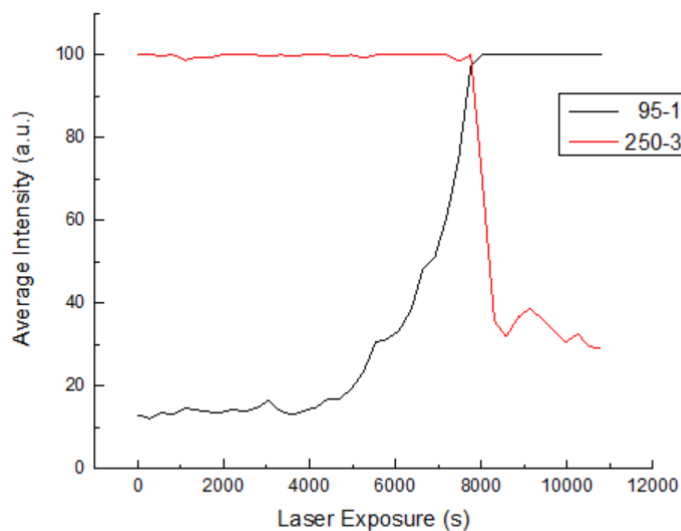


*Figure 3.3.14 Change in average intensity with laser exposure. Here we see the change in average intensity of the  $95\text{-}115\text{cm}^{-1}$  and the  $250\text{-}300\text{cm}^{-1}$  wavenumber range relating to  $\text{PbI}_2$  and the  $\text{MAPbI}_3$  induced step respectively.*

### **Axial Scans**

After having determined the parameters for non-destructive characterization of the  $\text{MAPbI}_3$  film I continued towards the goal of determining if this method can adequately differentiate between  $\text{MAPbI}_3$  and its degradation biproduct  $\text{PbI}_2$ . I performed axial measurements of a  $\text{PbI}_2$  film as well as a sample of  $\text{PbI}_2$  coated with the 10nm layer of  $\text{SnO}_2$ . Next, I performed axial measurements of  $\text{MAPbI}_3$  before finally moving on to the  $\text{MAPbI}_3/\text{SnO}_2/\text{PbI}_2$  layered sample.

In Figure 3.3.15 we see the spectra of the  $\text{PbI}_2$  film compared to that of the degraded  $\text{MAPbI}_3$ . We can see the same sharp peaks at  $94$  and  $115\text{cm}^{-1}$  in both samples however the degraded  $\text{MAPbI}_3$  sample still has a minor remnant of the initial step-feature.

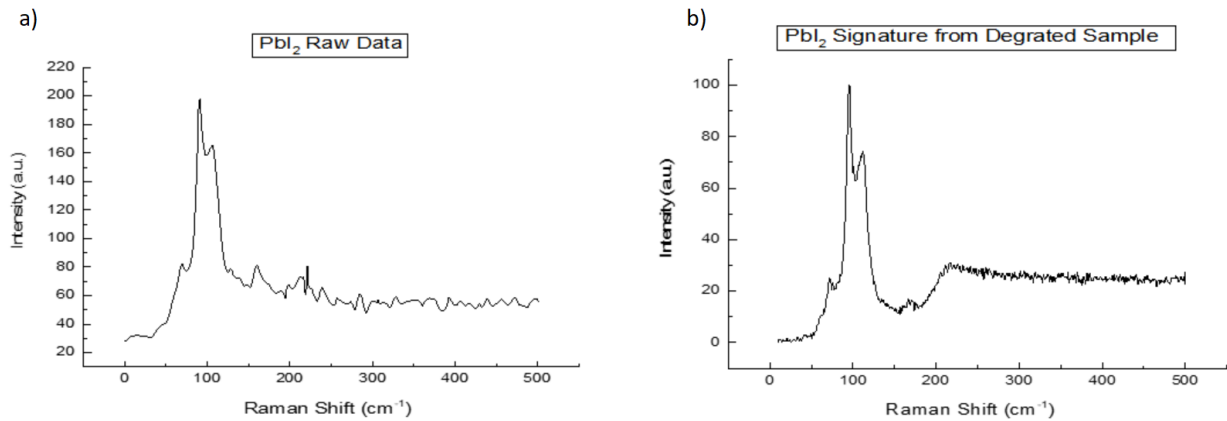


*Figure 3.3.15 comparison of PbI<sub>2</sub> data. Here we see (a) Raw PbI<sub>2</sub> data compared to (b) the PbI<sub>2</sub> spike that appears in the degraded MAPbI<sub>3</sub> film.*

The results of the axial scan are shown in Figure 3.3.16 where we can see the map of the Raman signature through the z-axis in 3.3.16a and the average intensity changing throughout the film in the PbI<sub>2</sub> wavenumber range as well as spectra from above and below the film and in the center. Moving on to Figure 3.3.17 we see a single spectra graph showing both the peaks for PbI<sub>2</sub> and SnO<sub>2</sub>, and the change of intensity as the Raman scans into the depth of the film.

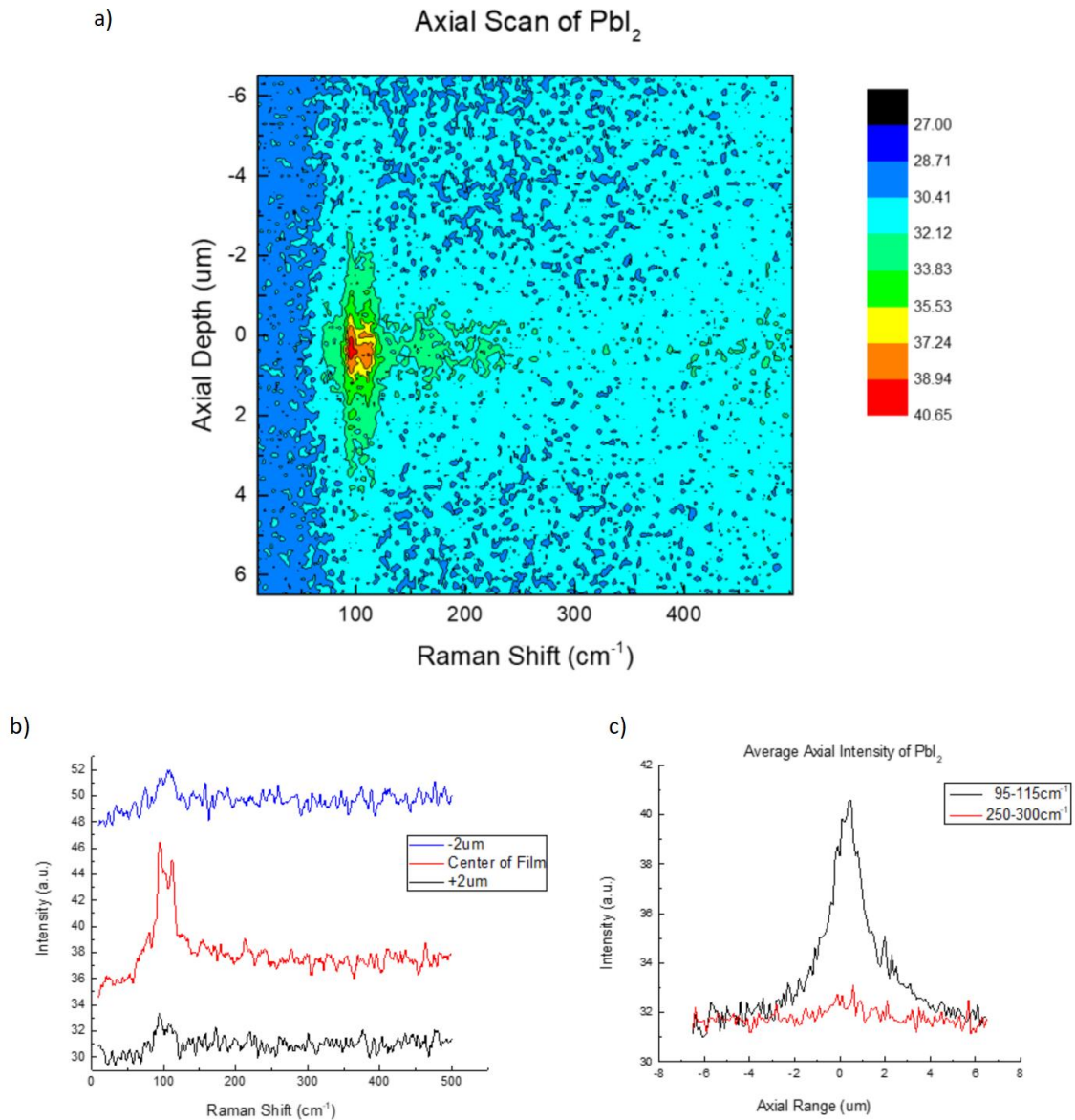


**Figure 3.3.16 Axial (z-axis/depth) scan of  $PbI_2$ .** In a) we see the intensity map as Horiba scans from the air interface to the glass substrate. b) shows the spectra collected in the center of the film as well as areas above and below the film. In c) we see the average intensity of the 95-115  $cm^{-1}$  wavenumber range, associated with  $PbI_2$  and a baseline range of 250-300  $cm^{-1}$ .

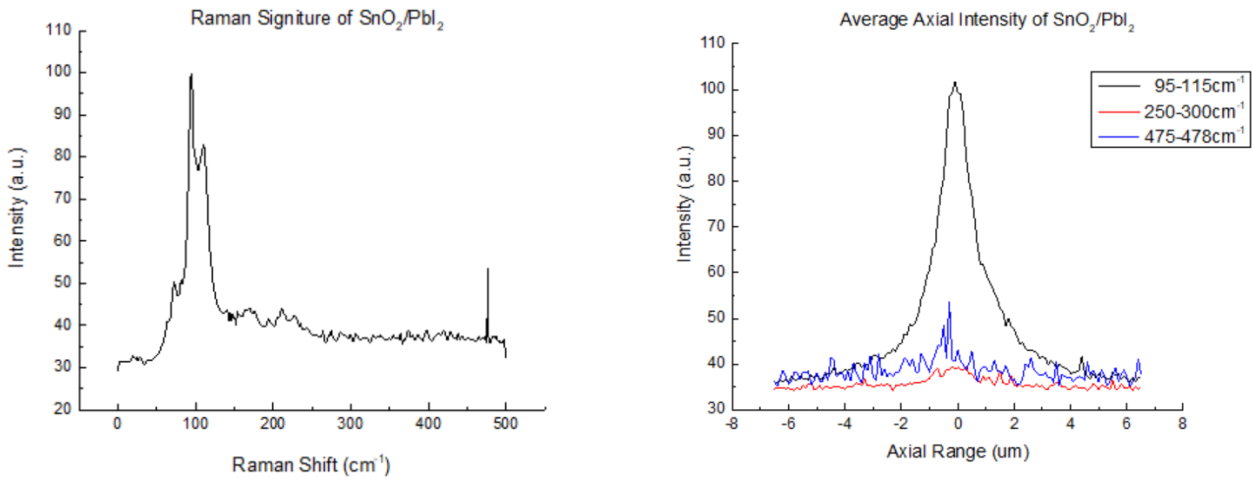


**Figure 3.3.17 Raman Spectra of PbI<sub>2</sub> film covered with 10nm of SnO<sub>2</sub>.** To the left we see both the PbI<sub>2</sub> peaks as 95 and 115cm<sup>-1</sup> and the sharp SnO<sub>2</sub> peak at 477cm<sup>-1</sup>. To the right we see the average intensity of the 95-115cm<sup>-1</sup> and 475-478cm<sup>-1</sup> wavenumber range, associated with PbI<sub>2</sub> and SnO<sub>2</sub> respectively, as well as a baseline range of 250-300cm<sup>-1</sup>.

Next, I proceeded to gather axial measurements of MAPbI<sub>3</sub> film. In Figures 3.3.18 and 3.3.19 we see the intensity map through the film with the former being the mapping results when the step-feature is present and the later showing the proper Raman spectra. Finally, we see in Figure 3.3.20 the axial scan of the MAPbI<sub>3</sub>/SnO<sub>2</sub>/PbI<sub>2</sub> film stack. One quickly notices that it lacks the symmetry found in the previous graphs of the MAPbI<sub>3</sub> only films.

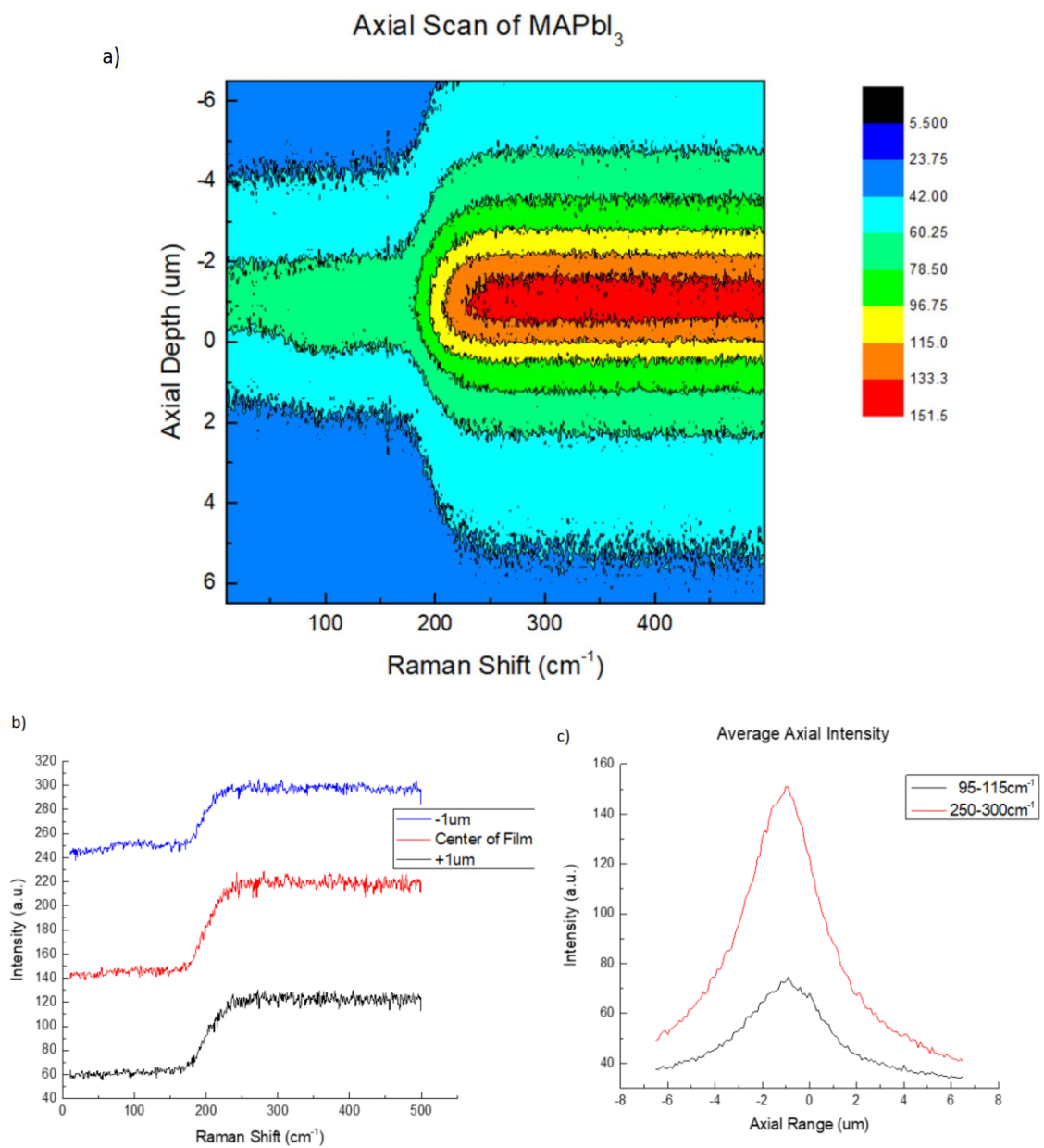


**Figure 3.3.18** Axial (z-axis/depth) scan of MAPbI<sub>3</sub> show the step-feature. In a) we see the intensity map as Horiba scans from the air interface to the glass substrate. b) shows the spectra collected in the center of the film as well as areas above and below the film. In c) we see the average intensity of the 95-115cm<sup>-1</sup> wavenumber range, associated with PbI<sub>2</sub> and the MAPbI<sub>3</sub> induced step range of 250-300cm<sup>-1</sup>.

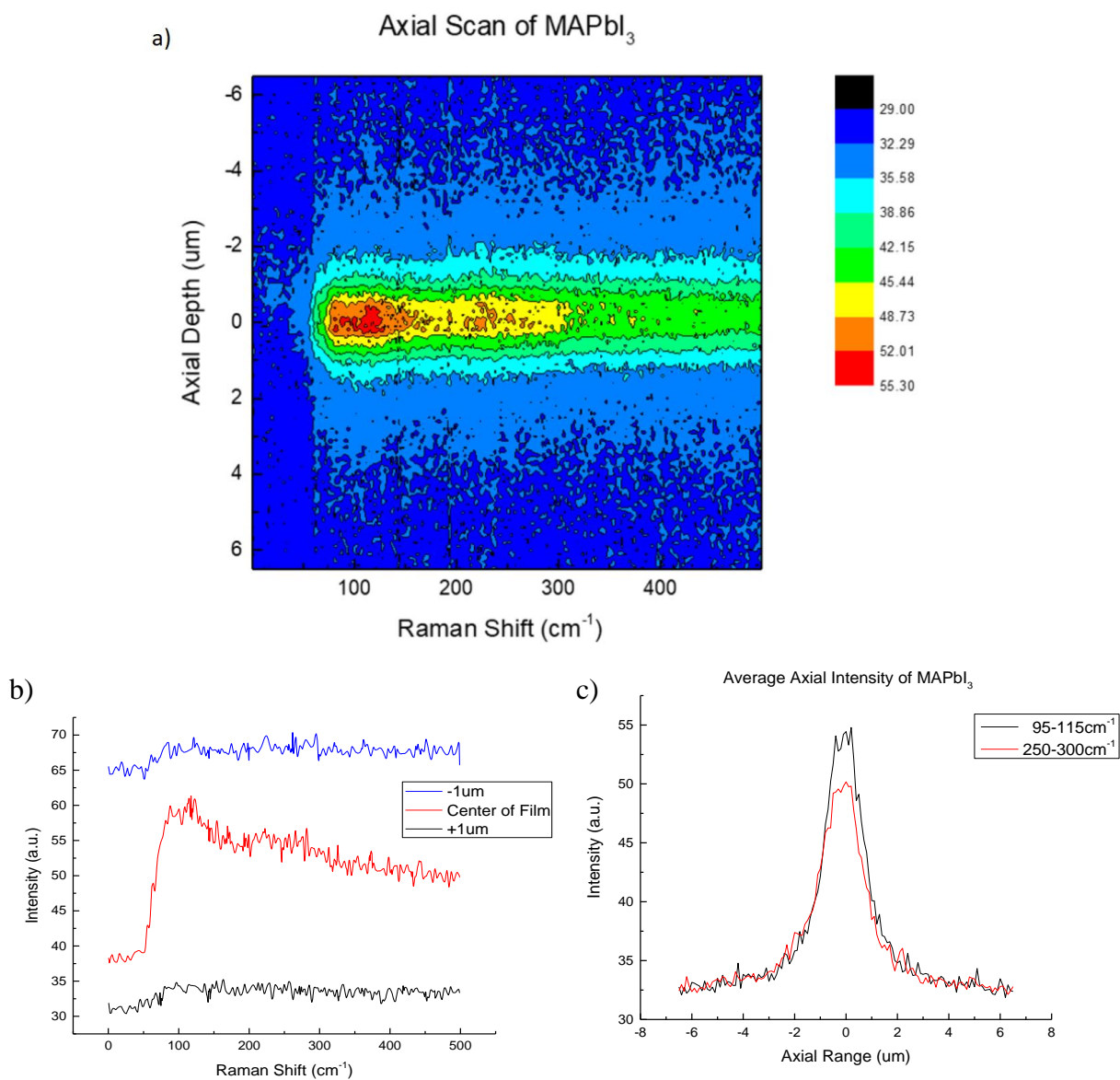


**Figure 3.3.19** Axial (z-axis/depth) scan showing the proper signature for a MAPbI<sub>3</sub> film. In a) we see the intensity map as Horiba scans from the air interface to the glass substrate. b) shows the spectra collected in the center of the film as well as areas above and below the film. In c) we see the average intensity of the 95-115cm<sup>-1</sup> wavenumber range, associated with PbI<sub>2</sub> and the MAPbI<sub>3</sub> induced step range of 250-300cm<sup>-1</sup>.

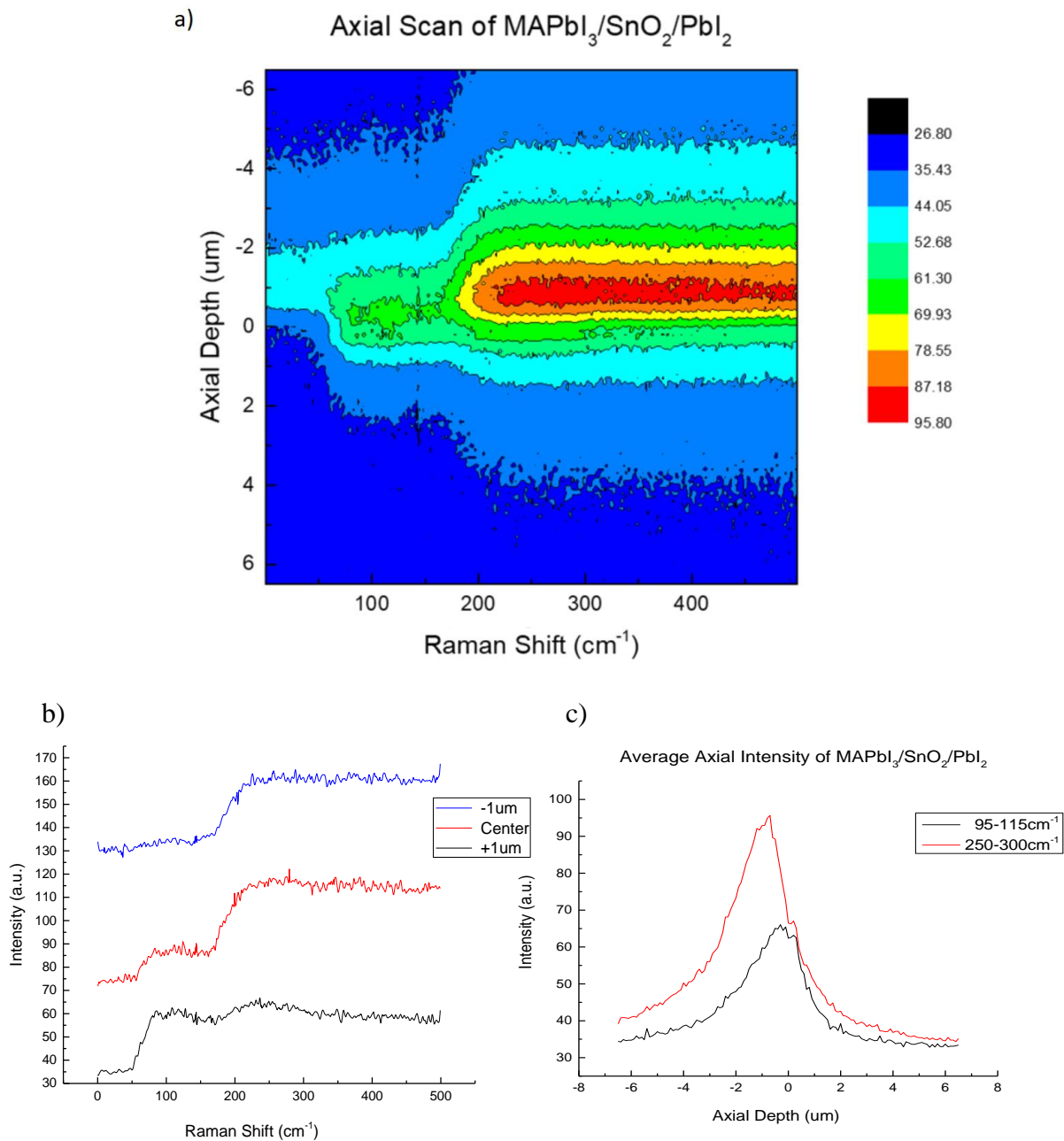


**Figure 3.3.20** Axial (z-axis/depth) scan of MAPbI<sub>3</sub>/SnO<sub>2</sub>/PbI<sub>2</sub>. In a) we see the intensity map as Horiba scans from the air interface to the glass substrate. b) shows the spectra collected in the center of the film as well as areas above and below the film. In c) we see the average intensity of the 95-115cm<sup>-1</sup> wavenumber range, associated with PbI<sub>2</sub> and the MAPbI<sub>3</sub> induced step range of 250-300cm<sup>-1</sup>.

## CONCLUSIONS

All three of the methods have shown potential to be techniques that could be used to investigate samples at various stages of degradation to determine at which interface the decomposition may be originating from despite various issues and limitation that each of the techniques have.

Spectroscopic Ellipsometry (SE) allowed us to develop Tauc-Lorentz physical models for optical (n,k) constants of MAPI perovskite and decomposition product (PbI<sub>2</sub>) in the UV-VIS-NIR (245-1690nm) spectral range. With these models, SE was able to accurately determine the layer thickness of both the MAPbI<sub>3</sub> and PbI<sub>2</sub>. Although it has a limited XY resolution of ~3mm its resolution of <10nm in the Z-axis direction is adequate for the future testing purposes of reviling areas of Z-axial film degradation.

The method of Confocal PL shows promises as a characterization method for determining which interface degradation is occurring, however there are issues with its low axial resolution that seem to prohibit us from determining accurate thicknesses of both the film and the layer of degraded perovskite. Further testing must be made to investigate the methods ability to differentiate between MAPbI<sub>3</sub> and PbI<sub>2</sub> at the substrate interface, as well as varying the film thickness of both the MAPbI<sub>3</sub> and the PbI<sub>2</sub> to determine how accurate of a correlation there is between the spread of axial intensity and film thicknesses.

Confocal Raman, despite the yet to be understood anomaly of the MAPbI<sub>3</sub> induced step feature, and having a <1 μm spatial resolution in the Z-axis (similar to that of confocal PL), proved to be a valuable tool in characterizing and understanding MAPbI<sub>3</sub> and its interfacial mechanics. It, like c-PL, was successful in distinguishing

between layers of  $\text{PbI}_2$  and  $\text{MAPbI}_3$  as well as directly confirming that the decomposition of  $\text{MAPbI}_3$  results in a  $\text{PbI}_2$  biproduct, by revealing its chemical signature. We have developed a protocol that allows us to collect reproducible Raman spectra using Horiba LabRam HR at TXST. However, this method requires high laser excitation, and thus careful parameter tuning is required to get reliable results without inducing thermal decomposition of the film and is highly dependent on the properties of the interfacial layers employed. As I have shown, critical laser power (when decomposition of  $\text{MAPbI}_3$  occurs) depends on the MAPI interface with the substrate, ETL, and HTL. We argue that one of the main factors can be a heat conductivity of the MAPI interface.

## VITA

Joseph Allen Sadler was born August 9, 1983 in Miami, Ok, the son of Rebecca Lyn Buchanan and Chester Sadler. He graduated from Gatesville High School in 2002 after which he enlisted in the U.S. Navy where he served as a SIGINT analyst for the National Security Agency while stationed at Fort Meade, Md. He later became active in the student organization Young American for Liberty as president of the Anne Arundel CC chapter and media coordinator of the Texas State University chapter. While at Texas State University he lead a philosophy dialogue series that aimed to produce thoughtful discourse between panels of speakers with diverse political views. Additionally, he devoted his time to tutoring math and worked as a physics learning assistant while striving to improve his ability to communicate complex topics in an effective manner. In 2015 he received his Bachelor of Science in physics, with a minor in German, from Texas State University. In May of 2018 he received his Master of Science in physics from Texas State University. During his master's program he worked under Dr. Alexander Zakhidov, investigating the photovoltaic properties of perovskite solar cells. He then began working at NXP semiconductors as a Device Engineer.

## REFERENCES

1. Key world energy statistics. (2017).
2. BP. BP Statistical Review of World Energy 2017.
3. Diefenderfer, J., assumptions Vipin Arora, M. & Singer, L. E. International Energy Outlook 2016 Liquid fuels. 202–586 (2040).
4. BP. BP Energy Outlook 2017.
5. Eia. Annual Energy Outlook 2017 with projections to 2050. (2017).
6. Gong, J., Darling Bc, S. B. & You, F. Perovskite photovoltaics: life-cycle assessment of energy and environmental impacts. *Energy Environ. Sci. Energy Environ. Sci* **8**, 1953–1968 (2015).
7. Eia. Levelized Cost and Levelized Avoided Cost of New Generation Resources in the Annual Energy Outlook 2017. (2017).
8. Henry Hazlitt. *Economics in One Lesson*. (1946).
9. von Mises, L. *Human Action: A Treatise on Economics*. *Political Science Quarterly* (1951). doi:10.2307/2145453
10. L Wells, V. H. Uber die Casium-und Kalium-Blei halogenide.
11. Weber, D. CH<sub>3</sub>NH<sub>3</sub>PbX<sub>3</sub>, ein Pb(II)-System mit kubischer Perowskitstruktur  
CH<sub>3</sub>NH<sub>3</sub>PbX<sub>3</sub>, a Pb(II)-System with Cubic Perovskite Structure. **33**, 1443–1445 (1978).
12. Kojima, A. *et al.* Novel Photoelectrochemical Cell with Mesoscopic Electrodes Sensitized by Lead-halide Compounds (5).
13. NREL Eff. Chart rev. 10-30-2017.

14. Fu, R., Feldman, D., Margolis, R., Woodhouse, M. & Ardani, K. U.S. Solar Photovoltaic System Cost Benchmark: Q1 2017. (2009).
15. Kalowekamo, J. & Baker, E. Estimating the manufacturing cost of purely organic solar cells. *Sol. Energy* (2009). doi:10.1016/j.solener.2009.02.003
16. Snaith, H. J. Perovskites: The emergence of a new era for low-cost, high-efficiency solar cells. *Journal of Physical Chemistry Letters* (2013). doi:10.1021/jz4020162
17. Whalley, L. D., Frost, J. M., Jung, Y.-K. & Walsh, A. Perspective: Theory and simulation of hybrid halide perovskites. (2017). doi:10.1063/1.4984964
18. Boix, P. P., Nonomura, K., Mathews, N. & Mhaisalkar, S. G. Current progress and future perspectives for organic/inorganic perovskite solar cells. *Mater. Today* (2014). doi:10.1016/j.mattod.2013.12.002
19. Sum, T. C. & Mathews, N. Advancements in perovskite solar cells: photophysics behind the photovoltaics. *Energy Environ. Sci.* (2014). doi:10.1039/C4EE00673A
20. Zhang, W. *et al.* Highly efficient perovskite solar cells with tunable structural color. *Nano Lett.* (2015). doi:10.1021/nl504349z
21. Zhou, X., Jankowska, J., Dong, H. & Prezhd, O. V. Accepted Manuscript Review Recent theoretical progress in the development of perovskite photovoltaic materials Review Recent theoretical progress in the development of perovskite photovoltaic materials Review Recent theoretical progress in the development of perovskite photovoltaic materials. *J. Energy Chem.* (2017). doi:10.1016/j.jechem.2017.10.010
22. Park, N. G. Perovskite solar cells: An emerging photovoltaic technology. *Materials Today* (2015). doi:10.1016/j.mattod.2014.07.007

23. Wan-Jian Yin, Ji-Hui Yang, Joongoo Kang, Y. Y. and S.-H. W. Halide perovskite materials for solar cells: a theoretical review. *J. Mater. Chem. A* 8926–8942 (2015). doi:10.1039/C4TA05033A
24. Dong, Q. *et al.* Electron-hole diffusion lengths > 175 um in solution-grown CH<sub>3</sub>NH<sub>3</sub>PbI<sub>3</sub> single crystals. *Science* (80-. ). **347**, 967–970 (2015).
25. Wang, Q. *et al.* Qualifying composition dependent p and n self-doping in CH<sub>3</sub>NH<sub>3</sub>PbI<sub>3</sub>. *Appl. Phys. Lett.* (2014). doi:10.1063/1.4899051
26. Park, N.-G., Grätzel, M., Miyasaka, T., Zhu, K. & Emery, K. Towards stable and commercially available perovskite solar cells. *Nat. Energy* (2016). doi:10.1038/nenergy.2016.152
27. Pisoni, A. *et al.* Ultra-low thermal conductivity in organic-inorganic hybrid perovskite CH<sub>3</sub>NH<sub>3</sub>PbI<sub>3</sub>. *J. Phys. Chem. Lett.* (2014). doi:10.1021/jz5012109
28. Conings, B. *et al.* Intrinsic Thermal Instability of Methylammonium Lead Trihalide Perovskite. *Adv. Energy Mater.* (2015). doi:10.1002/aenm.201500477
29. Zhao, X. & Park, N.-G. Stability Issues on Perovskite Solar Cells. *Photonics* (2015). doi:10.3390/photonics2041139
30. Brunetti, B., Cavallo, C., Ciccioli, A., Gigli, G. & Latini, A. On the Thermal and Thermodynamic (In)Stability of Methylammonium Lead Halide Perovskites. *Sci. Rep.* (2016). doi:10.1038/srep31896
31. Fang, H. & Jena, P. Molecular Origin of Properties of Organic-Inorganic Hybrid Perovskites: The Big Picture from Small Clusters. *J. Phys. Chem. Lett.* (2016). doi:10.1021/acs.jpcllett.6b00435

32. Frost, J. M. *et al.* Atomistic origins of high-performance in hybrid halide perovskite solar cells. *Nano Lett.* (2014). doi:10.1021/nl500390f
33. Niu, G., Guo, X. & Wang, L. Review of recent progress in chemical stability of perovskite solar cells. *J. Mater. Chem. A* (2015). doi:10.1039/C4TA04994B
34. Manspecker, C., Venkatesan, S., Zakhidov, A. & Martirosyan, K. S. Role of interface in stability of perovskite solar cells. *Curr. Opin. Chem. Eng.* **15**, 1–7 (2017).
35. Manspecker, C., Scruggs, P., Preiss, J., Lyashenko, D. A. & Zakhidov, A. Reliable Annealing of CH<sub>3</sub>NH<sub>3</sub>PbI<sub>3</sub> Films Deposited on ZnO. (2016). doi:10.1021/acs.jpcc.6b00364
36. Irene, E. A. A Brief History and State of the Art of Ellipsometry. doi:10.1007/978-3-642-33956-1\_1
37. Hinrichs, K., Eichhorn, K. J., Ertl, G., Mills, D. L. & Lüth, H. Ellipsometry of Functional Organic Surfaces and Films. *Springer Ser. Surf. Sci.* (2014). doi:10.1007/978-3-642-40128-2
38. Shirayama, M. *et al.* Optical Transitions in Hybrid Perovskite Solar Cells: Ellipsometry, Density Functional Theory, and Quantum Efficiency Analyses for CH<sub>3</sub>NH<sub>3</sub>PbI<sub>3</sub>. *Phys. Rev. Appl.* (2016). doi:10.1103/PhysRevApplied.5.014012
39. Ahuja, R. *et al.* Electronic and optical properties of lead iodide. doi:10.1063/1.1523145
40. Leguy, A. *et al.* The reversible hydration of CH<sub>3</sub>NH<sub>3</sub>PbI<sub>3</sub> in films, single crystals and solar cells.
41. Heinz, F. D., Gundel, P., Warta, W. & Schubert, M. C. Doping Density in Silicon and Solar Cells Analyzed With Micrometer Resolution. *IEEE J. Photovoltaics* **3**, 1–7 (2012).

42. Swartz, C. H. *et al.* Radiative and interfacial recombination in CdTe heterostructures. *Appl. Phys. Lett.* **105**, 222107 (2014).
43. Sheng, C.-X. *et al.* Laser action and photoexcitations dynamics in PbI<sub>2</sub> films. *Opt. Mater. Express* **5**, 530 (2015).
44. Pistor, P., Ruiz, A., Cabot, A. & Izquierdo-Roca, V. Advanced Raman Spectroscopy of Methylammonium Lead Iodide: Development of a Non-destructive Characterisation Methodology. *Sci. Rep.* **6**, 35973 (2016).
45. Reithmaier, G. *et al.* On-chip time resolved detection of quantum dot emission using integrated superconducting single photon detectors. *Sci. Rep.* (2013).  
doi:10.1038/srep01901
46. Olympus FV1000 User guide Olympus FV1000 MPE Microscope User Guide Olympus FV1000 User guide. (2011).
47. Phillips, L. J. *et al.* Dispersion relation data for methylammonium lead triiodide perovskite deposited on a (100) silicon wafer using a two-step vapour-phase reaction process. *Data Br.* (2015). doi:10.1016/j.dib.2015.10.026
48. Everall, N. J. Confocal Raman microscopy: common errors and artefacts. *Analyst* (2010).  
doi:10.1039/c0an00371a
49. Everall, N. J. Modeling and Measuring the Effect of Refraction on the Depth Resolution of Confocal Raman Microscopy. *Appl. Spectrosc.* **54**, (2000).
50. Sheppard, C. J. R., Connolly, T. J., Lee, J. & Cogswell, C. J. Confocal imaging of a stratified medium.
51. Cox, G. & Sheppard, C. J. R. Measurement of thin coatings in the confocal microscope. *Micron* (2001). doi:10.1016/S0968-4328(01)00017-8

52. Condeles, J. F., Lofrano, R. C. Z., Rosolen, J. M. & Mulato, M. Stoichiometry, surface and structural characterization of lead iodide thin films. *Brazilian J. Phys.* (2006). doi:10.1590/S0103-97332006000300023
53. Oku, T. in *Solar Cells - New Approaches and Reviews* (2015). doi:10.5772/59284
54. Venkatesan, S. *et al.* Tailoring nucleation and grain growth by changing the precursor phase ratio for efficient organic lead halide perovskite optoelectronic devices. *J. Mater. Chem. C* (2017). doi:10.1039/C7TC02928D
55. Pistor, P., Ruiz, A., Cabot, A. & Izquierdo-Roca, V. Advanced Raman Spectroscopy of Methylammonium Lead Iodide: Development of a Non-destructive Characterisation Methodology. *Sci. Rep.* (2016). doi:10.1038/srep35973
56. G. Grancini *et al.* CH<sub>3</sub>NH<sub>3</sub>PbI<sub>3</sub> perovskite single crystals: surface photophysics and their interaction with the environment. *Chem. Sci.* **6**, 7305–7310 (2015).
57. Sears, W. M., Klein, M. L. & Morrison, J. A. Polytypism and the vibrational properties of PbI<sub>2</sub>. *Phys. Rev. B* (1979). doi:10.1103/PhysRevB.19.2305
58. Quarti, C. *et al.* The raman spectrum of the CH<sub>3</sub>NH<sub>3</sub>PbI<sub>3</sub> hybrid perovskite: Interplay of theory and experiment. *J. Phys. Chem. Lett.* (2014). doi:10.1021/jz402589q